Computationally-effective Modeling of Far-field Underwater Explosion for Early-stage Surface Ship Design

Zhaokuan Lu

Dissertation submitted to the faculty of the Virginia Polytechnic Institute and State University in partial fulfillment of the requirements for the degree of

Doctor of Philosophy
in
Aerospace Engineering

Alan J. Brown, Chair
Robert A. Canfield
Christine M. Gilbert
Kevin G. Wang

February 25th, 2020
Blacksburg, Virginia

Keywords: Underwater explosion, Fluid-structure interaction, Shock wave, Cavitation, Spectral Element Method, Mesh generation, Statistical analysis

Computationally-effective Modeling of Far-field Underwater Explosion for Early-stage Surface Ship Design

Zhaokuan Lu

Abstract

The vulnerability of a ship to the impact of underwater explosions (UNDEX) and how to incorporate this factor into early-stage ship design is an important aspect in the ship survivability study. In this dissertation, attention is focused on the cost-efficient simulation of the ship response to a far-field UNDEX which involves fluid shock waves, cavitation, and fluid-structural interaction. Traditional fluid numerical simulation approaches using the Finite Element Method to track wave propagation and cavitation requires a high-level of mesh refinement to prevent numerical dispersion from discontinuities. Computation also becomes quite expensive for full ship-related problems due to the large fluid domain necessary to envelop the ship. The burden is aggravated by the need to generate a fluid mesh around the irregular ship hull geometry, which typically requires significant manual intervention. To accelerate the design process and enable the consideration of far-field UNDEX vulnerability, several contributions are made in this dissertation to make the simulation more efficient. First, a Cavitating Acoustic Spectral Element approach which has shown computational advantages in UNDEX problems, but not systematically assessed in total ship application, is used to model the fluid. The use of spectral elements shows greater structural response accuracy and lower computational cost than the traditional FEM. Second, a novel fully automatic all-hexahedral mesh generation scheme is applied to generate the fluid mesh. Along with the spectral element, the all-hex mesh shows greater accuracy than the all-tetrahedral finite element mesh which is typically used. This new meshing approach significantly saves time for mesh generation and allows the spectral element, which is confined to the hexahedral element, to be applied in practical ship problems. A further contribution of this dissertation is the development of a surrogate non-numerical approach to predict structural peak responses based on the shock factor concept. The regression analysis reveals a reasonably strong linear relationship between the structural peak response and the shock factor. The shock factor can be conveniently employed in the design aspects where the peak response is sufficient, using much less computational resources than numerical solvers.

Computationally-effective Modeling of Far-field Underwater Explosion for Early-stage Surface Ship Design

Zhaokuan Lu

General Audience Abstract

The vulnerability of a ship to the impact of underwater explosions (UNDEX) and how to incorporate this factor into early-stage ship design is an important aspect in the ship survivability study. In this dissertation, attention is focused on the cost-efficient simulation of the ship response to a far-field UNDEX which involves fluid shock waves, cavitation, and fluid-structural interaction. Traditional fluid numerical simulation approaches using the Finite Element Method to track wave propagation and cavitation requires a highly refined mesh to deal with large numerical errors. Computation also becomes quite expensive for full ship-related problems due to the large fluid domain necessary to envelop the ship. The burden is aggravated by the need to generate a fluid mesh around the irregular ship hull geometry, which typically requires significant manual intervention. To accelerate the design process and enable the consideration of far-field UNDEX vulnerability, several contributions are made in this dissertation to make the simulation more efficient. First, a Cavitating Acoustic Spectral Element approach, which has shown computational advantages in UNDEX problems but not systematically assessed in total ship application, is used to model the fluid. The use of spectral elements shows greater structural response accuracy and lower computational cost than the traditional FEM. Second, a novel fully automatic all-hexahedral mesh generation scheme is applied to generate the fluid mesh. Along with the spectral element, the all-hex mesh shows greater accuracy than the all-tetrahedral finite element mesh which is typically used. A further contribution of this dissertation is the development of a non-numerical approach which can approximate peak structural responses comparable to the numerical solution with far less computational effort.

Acknowledgments

I would like to express my deepest gratitude to my Ph.D. advisor Dr. Alan Brown for his constant guidance, great patience and delightful sense of humor. I want to thank my dissertation committee members, Dr. Robert Canfield, Dr. Christine Gilbert, and Dr. Kevin Wang, for sharing their knowledge with me unreservedly. I'm grateful for my fellow colleagues in Randolph 319, who bring me so much joy and unforgettable memories. I'm also very thankful to AOE department staff Steve Edwards, Jonathan Spencer, Kelsey Wall, and Racheal Hall for their administrative and IT supports. Last but not least, I want to thank my wonderful wife Yuting Feng for her unfailing love and caring, and my parents Juan Zhao and Yongkui Lu for their unconditional support.

Table of Contents

Chapter 1 Introduction

This dissertation is organized in a manuscript format which is comprised of a general introduction (Chapter 1), three stand-alone but coherent papers either published or prepared for publication (Chapter 2~4) and a final conclusion (Chapter 5).

1.1 Statement of the problem to be investigated and its significance

One of the most critical aspects of naval ship survivability is the vulnerability of a ship to an underwater explosion (UNDEX). UNDEX events can be categorized as near-field and far-field. In near-field explosions, the explosive is sufficiently close to the ship's hull and sufficiently large that its effects result in large plastic deformation [1]. Since most of the energy is absorbed in the ship's hull by this deformation, the destructive effect is typically severe, but local. In a far-field explosion, the charge may be less strong and/or located far enough from the ship that the primary impact of the explosion comes from the shock wave, and the ship's structural response is limited to elastic deformation. However, a significant amount of energy is still passed into the ship causing sudden motion of structural foundations and potentially significant equipment damage or personnel injury [2]. In the far-field regime, the shock wave released by the explosive decays to a nearly-linear acoustic wave with a discontinuous pressure profile as it reaches the ship. Other important phenomena of far-field UNDEX are the cavitation caused by inward panel motion (local cavitation) and cavitation caused by shock wave reflection from the free surface (bulk cavitation). Because the near-field and far-field phenomena are so different, far-field UNDEX is usually analyzed separately from near-field UNDEX, and because of its total-ship impact, the focus of this dissertation is on far-field UNDEX and shock. Shock trials are typically performed long after critical and irreversible ship design decisions are made, rarely before a naval ship is put into service. The shock trial process is long, extremely expensive, and environmentally unfriendly. In the past, early design assessment may be performed with computer prediction, but this is usually late in the design process when a greater level of detail is available, too late for avoiding costly design changes.

This dissertation addresses the problem of considering far-field UNDEX vulnerability in early-stage surface ship design. The first objective of this dissertation is to develop a computationally efficient numerical model to simulate the fluid, structure and fluid-structure interaction that is also sufficient for application in early-stage ship concept design. The structural response time-history results from the simulation can be employed to evaluate ship vulnerability to far-field explosions. Although made more efficient, numerical simulation is still unaffordable in concept exploration process (first step in early-stage design) where thousands of designs typically need to be evaluated. Meanwhile, peak structural responses alone may provide sufficient information to assess the severity of shock impact and guide decision-making such as equipment arrangement in the concept exploration. Therefore, the second objective of this dissertation is to identify and demonstrate efficient non-numerical approaches such as statistical and analytical schemes to be used as surrogates for and in conjunction with numerical models to predict peak structural responses for concept exploration and design.

1.2 Review of the previous work in the area

One of the frequently used simulation approaches in far-field UNDEX problems is the boundary element method (BEM). The advantage of the BEM is that little or no actual fluid modeling is required, thus allowing faster computation. One of the most used BEM methods is the doubly asymptotic approximation (DAA) by Geers [3] which applies partial differential equations to relate the pressure and displacement of a structural wet surface to the fluid boundary using the acoustic fluid assumption. However, if the cavitation effect cannot be neglected as in the surface ship problem, the fluid domain has to be explicitly discretized and coupled with the structural solver. Since the shock wave decays to a constitutively linear acoustic wave in the far-field UNDEX case, FEM-based approaches are typically favored due to their advantages in solving acoustic wave propagation. Felippa and Deruntz [4] proposed the cavitating acoustic finite element (CAFE) method which simulates the acoustic wave propagation using FEM and cavitation by a cut-off condition. Despite the benefits of using the FEM-based fluid models (e.g., CAFE), the dispersive nature of the FEM elements [5] makes them computationally expensive since high-level mesh refinement is needed to achieve a satisfactory solution. To resolve the dispersive nature of traditional FEM, the spectral element method (SEM) was introduced in the UNDEX problem by Sprague and Geers [6] in place of linear FEM. Incorporating the framework proposed by Felippa and Deruntz [4], their new solver was called cavitating acoustic spectral element (CASE) method. Introduced by Patera [7], SEM reduces the dispersion of the traditional FEM by using high-order basis functions. Although the high-order SEM suffers from increased spurious oscillation for the discontinuous shock wave (Gibbs phenomenon), the CASE approach exhibited superiority to the CAFE approach in 1D mass-spring [6] and 3D submerged spherical shell problem [8]. Klenow [9] associated the higher accuracy of the CASE with the better acoustic wave propagation and cavitation region modeling. However, the CASE solution has yet to be compared to CAFE in the far-field surface ship UNDEX problem which features complex structure, hull shape, and both local and bulk cavitation regions.

The task of applying CAFE/CASE to simulate the surface ship far-field UNDEX is complicated by the need to generate the fluid mesh around the irregular ship hull geometry. Ship design application requires fast simulation with minimal or no manual intervention in the mesh generation. It is desirable to make the mesh generation fully automatic. In prior research dealing with surface ships, hexahedral-dominant [10] and all-tetrahedral meshes [11] are most commonly used. The creation of hex-dominant meshes usually involves a degree of manual intervention to make the domain meshable. Although an automatic generation algorithm for hex-dominant meshes is introduced by Baudouin [12], the hex-mesh percentage is not guaranteed, and non-conformal faces exist. Automatic schemes to generate a tetrahedral mesh are quite mature (ex: Advancing front, Delaunay refinement). However, the tetrahedron is generally considered inferior to the hexahedron in terms of accuracy and computational efficiency since more elements must be used for the same DOF. As a result, an automatically generated all-hexahedral mesh with a satisfactory quality might be a better solution for this type of problem. Another benefit of using an all-hexahedral mesh is the potential to harness the benefit of the Spectral Element Method (SEM) which is confined to the hexahedral element.

Since the FSI boundary geometry is complicated, the fluid and structure interface meshes usually are non-matching. Thus, the displacement and nodal force need to be interpolated before it can be used by the partner solver. The CASE has previously been coupled to the structure by an average mapping technique which maps the average pressure and displacement fields in [8].

Although this method features straightforward implementation, high-pressure gradients induced by the oblique shock wave are smoothed. Thus, the accuracy of the peak velocity prediction may suffer. It has not been demonstrated whether CASE would preserve superior behavior if a more rigorous information mapping scheme (e.g., consistent mapping scheme [13]) is used.

To find effective surrogate non-numerical approaches, we traced back the literature to the era before the dominance of numerical simulation. In 1961, Keil [2] proposed a conceptual shock factor based on the shock wave energy density which can linearly scale the structural velocity response according to his account. This shock factor is later applied to a submarine-like structure by O'Hara [14]. Zhang [15] proposed a modified shock factor for small cylindrical objects to account for the shock wave scattering effect. The modified shock factor linearly scales the peak acceleration of the structure response successfully. Guo [16] adopted the Keil shock factor for a SWATH catamaran with some adjustments to consider the shock wave shadowed by the double-hull structure. A similar structural response is found under an equal shock factor condition. Although the shock factor is frequently used to quantify the shock severity imposed on surface ships (e.g., [17]), a generalized shock factor for the surface ship that can be used to predict the peak structural response under different far-field UNDEX events and at different locations in the ship has never been fully explored.

1.3 The proposed approach for investigating the problem

We first employ the basic ideas of Cavitating Acoustic Finite (CAFE) and Spectral Element (CASE) for modeling the fluid and couple them to an Abaqus explicit structural solver. As a preliminary step to applying our approach to a full surface ship problem, we use a floating shock platform (FSP) problem to show the potential relative computational advantage in far-field surface ship UNDEX problems. A general-purpose searching and projection algorithm is devised to facilitate the fluid-structure interaction. In addition, consistent, average, and energy-conservative mapping schemes are explored and compared to determine which is the most cost-effective approach. The implementation details can be found in Chapter 2.

In Chapter 3, the attention is focused on simulating the actual surface ship structure. We assess a mesh-first, automatic, all-hexahedral mesh generation scheme called Sculpt algorithm (Owen, Staten, and Sorensen 2011) that provides excellent early-time UNDEX simulation results with only minimal compromise in the boundary geometry accuracy. The resulting fluid mesh is used with linear and high-order SEM elements and results are compared to an all-tetrahedral mesh generated by an automatic Delaunay refinement algorithm with linear FEM elements. The comparison is performed for both Total Field and Scattered Field Finite and Spectral Element Cavitating Acoustic fluid models.

For the non-numerical approaches intended for concept exploration presented in Chapter 4, the shock factor developed by Keil [2] is first refined to be used for ships and extended to predict peak acceleration. To confirm the linear relationship, regression analysis is performed between the shock factor and the peak structural response predicted by the CASE-Abaqus coupled numerical solver. To further accelerate the regression data collection, an analytical fluid model proposed by G.I. Taylor [18] is assessed, with the hope to substitute or work in conjunction with the numerical fluid solver. By assuming the fluid is perfectly acoustic, the Taylor model is able to describe the fluid effect on the fluid-structure interface. The model gradually fails as the cavitation starts to generate, violating the acoustic assumption. However, the first few milliseconds the Taylor model can correctly simulate may be sufficient to capture the structural peak response. In early-stage ship design, a combination of the high-fidelity CASE

model and the low-fidelity Taylor model may greatly improve the concept exploration process, following a variable fidelity approach as described in [19].

1.4 Contribution to co-authored papers

The contributions of the papers (Chapter 2~Chapter 4) by the author of this dissertation are listed below:

Chapter 2:

- Developed the solver for simulation.
- Performed the numerical simulation.
- Wrote the major part of the paper.

Chapter 3:

- Developed the solver for simulation.
- Performed the numerical simulation.
- Wrote the major part of the paper.

Chapter 4:

- Developed the major part of the theory.
- Performed the statistical analysis.
- Wrote the major part of the paper.

Reference

[1] W. D. Reid, *The Response of Surface Ships to Underwater Explosions*. Melbourne, Vic. : DSTO Aeronautical and Maritime Research Laboratory, 1996.

[2] A. H. Keil, "The Response of Ships To Underwater Explosions," in *Transactions of Society of Naval Architects and Marine Engineers*, 1961.

[3] T. L. Geers, "Residual Potential and Approximate Methods for Three-Dimensional Fluid-Structure interaction problems," *J. Acoust. Soc. Am.*, vol. 49, no. 5, pp. 1505–1510, 1970.

[4] C. A. Felippa and J. A. DeRuntz, "Finite Element Analysis of Shock-induced Hull Cavitation," *Comput. Methods Appl. Mech. Eng.*, vol. 44, no. 3, pp. 297–337, 1984.

[5] J. D. De Basabe and M. K. Sen, "Grid Dispersion and Stability Criteria of Some Common Finite-Element Methods for Acoustic and Elastic Wave Equations," *Geophysics*, vol. 72, no. 6, pp. T81–T95, 2007.

[6] M. A. Sprague and T. L. Geers, "Spectral Elements and Field Separation for an Acoustic Fluid Subject to Cavitation," *J. Comput. Phys.*, vol. 184, no. 1, pp. 149–162, 2003.

[7] A. T. Patera, "A Spectral Element Method for Fluid Dynamics: Laminar Flow in a Channel Expansion," *J. Comput. Phys.*, vol. 54, no. 3, pp. 468–488, 1984.

[8] M. A. Sprague and T. L. Geers, "A Spectral-Element Method for Modelling Cavitation in Transient Fluid-Structure Interaction," *Int. J. Numer. Methods Eng.*, vol. 60, no. 15, pp. 2467–2499, 2004.

[9] B. Klenow, "Finite and Spectral Element Methods for Modeling Far-Field Underwater Explosion Effects on Ships," Virginia Tech, 2009.

[10] Z. Zong, Y. Zhao, and H. Li, "A Numerical Study of Whole Ship Structural Damage Resulting from Close-In Underwater Explosion Shock," *Mar. Struct.*, vol. 31, pp. 24–43, 2013.

[11] H. Wang, X. Zhu, Y. S. Cheng, and J. Liu, "Experimental and numerical investigation of

ship structure subjected to close-in underwater shock wave and following gas bubble pulse," *Mar. Struct.*, vol. 39, pp. 90–117, 2014.
[12] T. C. Baudouin, J. F. Remacle, E. Marchandise, F. Henrotte, and C. Geuzaine, "A frontal approach to hex-dominant mesh generation," *Adv. Model. Simul. Eng. Sci.*, vol. 1, no. 1, pp. 1–30, 2014.
[13] C. Farhat, M. Lesoinne, and P. Le Tallec, "Load and Motion Transfer Algorithms for Fluid/structure Interaction Problems with Non-matching Discrete Interfaces: Momentum and Energy Conservation, Optimal Discretization and Application to Aeroelasticity," *Comput. Methods Appl. Mech. Eng.*, vol. 157, no. 1–2, pp. 95–114, 1998.
[14] G. J. O'Hara and P. F. Cunniff, "Scaling for Shock Response of Equipment in Different Submarines," *Shock Vib.*, vol. 1, no. 2, pp. 161–170, 1993.
[15] W. Zhang and W. Jiang, "An Improved Shock Factor to Evaluate the Shock Environment of Small-Sized Structures Subjected to Underwater Explosion," *Shock Vib.*, vol. 2015, pp. 1–11, 2015.
[16] J. Guo, X. bin Ji, Y. yan Wen, and X. wei Cui, "A new shock factor of SWATH catamaran subjected to underwater explosion," *Ocean Eng.*, vol. 130, no. December 2016, pp. 620–628, 2017.
[17] C.-C. Liang and Y.-S. Tai, "Shock responses of a surface ship subjected to noncontact underwater explosions," *Ocean Eng.*, vol. 33, no. 5–6, pp. 748–772, 2006.
[18] G. I. Taylor, "The Pressure and Impulse of Submarine Explosion Waves on Plates," *Sci. Pap. Sir Geoffrey Ingram Taylor*, pp. 287–303, 1941.
[19] A. Brown, S. Brizzolara, and S. Choi, "Set-Based Design Framework for Naval Ship Concept Exploration with Tight Integration of High-Fidelity Physics-Based Simulations," in *ASNE SetBased Design Symposia*, 2017.

Chapter 2 Application of the Spectral Element Method in a Surface Ship Far-field UNDEX Problem

(Published in Shock and Vibration)

Zhaokuan Lu, Alan Brown
Department of Aerospace and Ocean Engineering, Virginia Tech, Blacksburg, VA, 24061, USA

Abstract

The prediction of surface ship response to a far-field underwater explosion (UNDEX) requires the simulation of shock wave propagation in the fluid, cavitation, fluid-structure interaction and structural response. Effective approaches to model the fluid include Cavitating Acoustic Finite Element (CAFE) and Cavitating Acoustic Spectral Element (CASE) methods. Although the Spectral Element method offers the potential for greater accuracy at lower computational cost, it also generates more spurious oscillations around discontinuities which are difficult to avoid in shock related problems. Thus, the advantage of CASE remains unproven. In this paper, we present a 3D partitioned FSI framework and investigate the application of CAFE and CASE to a surface ship early-time far-field UNDEX problem to determine which method has the best computational efficiency for this problem. We also associate the accuracy of the structural response with the modeling of cavitation distribution. A further contribution of this work is the examination of different non-matching mesh information exchange schemes to demonstrate how they affect the structural response and improve the CAFE/CASE methodologies.

Keywords: Underwater explosion, Spectral Element Method, Shock wave, Cavitation

2.1 Introduction

2.1.1 Background

One of the most studied aspects of naval ship survivability is the vulnerability of a ship to an underwater explosion. Shock trials are rarely performed before a naval ship is put into service when valuable information on the ship and onboard equipment response to underwater shock could be obtained. The process is long, extremely expensive and environmentally unfriendly. Thus, early assessment has been mostly performed with computational prediction.

UNDEX events can be categorized as near-field, and far-field. In near-field explosions, the explosive is sufficiently close to the ship's hull and sufficiently large that its effects result in large plastic deformation [1], [2]. Since the energy is mostly absorbed in the ship's hull by the deformation, the destructive effect is typically local, but severe. In this work, we focus on the early-time far-field UNDEX where the explosive is small or relatively far from the ship's hull, and the shock wave released by the explosive has decayed to a linear acoustic wave with a discontinuous pressure profile as it reaches the ship [2]. The structural deformation is mostly or entirely elastic. The high-frequency and low-inertia response of the hull plate panels is excited due to the propagation of the energy into the structure. Onboard equipment and people can be exposed to dangerous accelerations. At the point where the hull panels move inward faster than the surrounding water, the water is subject to tension. A cavitation region called local cavitation is developed near the panel due to the inability of water to sustain tension. Eventually, the local cavitation begins to shrink and collapses as the pressure near the panel is restored and the panel

rebounds. The collapse creates an impact pressure pulse and panel reloading [3]. At about the same time, the incident shock wave reaches the free surface and the reflection of the shock wave generates a tensile wave. Due to the large impedance difference between water and air, the reflected wave pressure is almost the negative of the incident shock wave, which significantly reduces the total pressure. A large cavitation region is formed when the total pressure drops below vapor pressure and remains cavitated until the pressure is restored. This cavitation region is called bulk cavitation. The closure of bulk cavitation also emits a shock wave, the timing and impact of which depends on the ship's proximity to the closure point [2]. The combination of incident shock wave loading and subsequent response to cavitation constitutes the early-time response of a surface ship to the far-field UNDEX.

2.1.2 Modeling techniques for the fluid domain in UNDEX

The fluid-structure interaction of UNDEX problem was first addressed by Taylor [4] who proposed the Taylor Plate Theory to calculate structural motion under shock impact. The fluid-structure interaction between an exponentially decaying plane shock wave and an infinite air-backed rigid plate was analyzed. The relationship between the wetted surface pressure and plate motion is obtained using Newton's second law and a linear acoustic assumption. Taylor Plate Theory provides a quick and simple way of estimating peak kick-off velocity (the highest upward velocity induced by shock) where hull structural panels are generalized as rigid plates [5]. However, no interaction between cavitated fluid and structure is captured since the fluid domain is not modeled.

The Boundary Element Method (BEM) has also been used in far-field UNDEX problems. The advantage of the BEM is that little or no actual fluid modeling is required, thus allowing faster computation. One of the most used BEM methods is the Doubly Asymptotic Approximation (DAA) by Geers [6]–[8] which applies partial differential equations to relate the pressure and displacement of a structural wet surface to the fluid boundary using the acoustic fluid assumption. The formulation of the first order DAA includes an early-time approximation (ETA) and late-time approximation (LTA). The name doubly asymptotic suggests that the approximation approaches the exact solution at both early-time/high-frequency and late-time/low-frequency limits. DAA is used in the Underwater Shock Analysis program (USA) [9] which simulates with the UNDEX problems without cavitation. The motion of a submerged cylindrical shell exposed to a far-field underwater explosion, where the high ambient pressure prevents cavitation, was solved using the USA code in [10] and results compare well with experimental data. However, if the cavitation effect cannot be neglected as in the surface ship problem, the fluid domain or a portion of it needs to be explicitly modeled. The response of a floating barge exposed to an UNDEX simulated by the USA code with and without cavitation shows a significant difference in structural response [11]. To improve the pure BEM based on DAA when cavitation presents, several wet-surface approximation (WSA) models have been introduced (e.g., [12]). The investigation of WSA coupled with elastic mass-spring system conducted in [13] revealed the degraded accuracy due to the inability of capturing the fluid accretion (uncavitated fluid between the cavitation upper boundary and the structure).

A more rigorous way of simulating the events involving fluid cavitation is to explicitly discretize the fluid domain and couple it with the structural solver. Since the shock wave decays to a constitutively linear acoustic wave in the far-field UNDEX case, finite element-based approaches are typically favored due to their advantages in solving acoustic wave propagation. The foundation of the FEM-type treatment was proposed by Newton [14] who used a scalar

displacement potential-based formulation to model the acoustic fluid and a bilinear equation of state for cavitation. Newton also observed the effect of frothing (spurious cavitation region) caused by the discontinuity near the cavitation-fluid boundary [14]. Newton's model was later used in [15] to study seismic waves and cavitation effects on a dam. Felippa and DeRuntz [16] proposed the Cavitating Acoustic Finite Element Method (CAFE) based on the work of Newton and implemented it in their Cavitating Fluid Analysis (CFA) code. A damping factor was introduced to reduce the frothing. The CAFE approach was later used with the commercial FEM code LS-DYNA and applied in several far-field UNDEX problems (e.g., [17], [18]). The Abaqus explicit acoustic solver has also been used by many researchers [19]–[23]. Abaqus takes a similar approach to CAFE using the linear acoustic element (AC3D8R), but with a pressure-based formulation [24]. Despite the benefits of using the FEM-based fluid models (e.g., CAFE), the dispersive nature of the FEM elements [25] makes them computationally expensive since high-level mesh refinement is needed to achieve a satisfactory solution.

To resolve the dispersive nature of traditional FEM, the Spectral Element Method (SEM) was introduced in the UNDEX problem by Sprague and Geers [26]–[29] in place of linear FEM. Incorporating the framework proposed by Felippa and DeRuntz [16], their new solver was called Cavitating Acoustic Spectral Element Method (CASE). Introduced by Patera [30], SEM is a combination of the Spectral Method and traditional FEM. High-order basis functions with interpolation nodes at the root of orthogonal polynomials are used to reduce the interpolation error which makes SEM less dispersive than linear FEM. Although the high-order SEM suffers from increased spurious oscillation for the discontinuous shock wave (Gibbs phenomenon), the CASE approach exhibited the same accuracy with less computational resources compared to CAFE in a 1D mass-spring plane shock wave problem [26] and a 3D submerged spherical shell problem [27]. It has also been shown that CASE is manageable for a modern PC for the surface ship far-field UNDEX problem [28]. Klenow [31] assessed the superior behavior of CASE in 1D and associated the higher accuracy of the CASE with the better cavitation region modeling. The same submerged spherical shell in [27] with cavitation effect neglected was investigated in [32] using SEM. The results again showed the higher accuracy of the CASE compared to CAFE with the same degrees of freedom. However, the CASE solution has yet to be compared to CAFE in the far-field surface ship UNDEX problem which features complex structure, hull shape and both local and bulk cavitation regions.

Due to the different phenomenon and geometric simplicity of the submerged spherical shell (deep-water UNDEX) compared to the surface ship, the advantage of CASE found in the Sprague & Geers study [26] does not necessarily exist in a complex surface ship application. Thus, it remains to be determined whether high-order SEM possesses a computational advantage over other types of FEM for the surface ship UNDEX problem.

2.1.3 Information exchange schemes at the fluid-structure interface

In early CAFE applications, node-to-node matching of the linear FEM-based fluid and the structural mesh was used. Since the fluid element is usually smaller, the structural element size needs to be decreased to meet the requirement on the boundary, which lowers the stable time increment and increases the computational cost. The one-to-one matching scheme also makes it difficult to connect the fluid mesh to a complex structural mesh [33]. This approach is even less applicable to a high-order SEM based fluid solver coupled to structural linear FEM solver since the nodes are arranged differently in the spectral element. Therefore, pressure and displacement

usually have to be interpolated between the non-matching meshes using various data exchange schemes.

The desirable features of effective data exchange schemes are global load (force) conservation, energy conservation, and mapping consistency. Load conservation means the total fluid nodal force does not change after it is received on the structural side. By the same principle, energy conservation requires the balance of total work input/received by the fluid and received/input by the structure. Mapping consistency guarantees the constant pressure (Interface Force Patch test) and a linearly varying displacement field (Interface rigid-motion path test) to be exactly mapped [34]. Following the nomenclature and classification of [34], interface treatments can be categorized as Prime dual, Dual and Direct Force-Motion Transfer methods (DFMT). Prime dual (also called the Mortar method [35]) and dual approaches employ global and localized Lagrange multipliers to enforce the consistency of displacement or pressure during the fluid and structure interaction. The mapping error is minimized by solving a weighted residual-based equation system. The aforementioned features can all be satisfied (e.g., [36]). However, the prime dual and dual methods involve a large amount of computation since all the DOFs on the boundary are coupled and the equation system needs to be solved.

In our research, we focus on Direct Force-motion Transfer methods (DFMT) which are local in nature (involving only neighboring nodes for interpolation), thus less computational effort. The implementation of DFMT is also greatly simpler than the prime dual and dual methods. Among the different Direct Force-motion Transfer (DFMT) schemes for non-matching meshes, the Consistent Interpolation approach [37]–[39] and Energy Conservative mapping approach [38] are often used. The consistent approach guarantees the mapping consistency of the pressure and the displacement fields. Although the consistent algorithm does not enforce force and energy conservation, it does not necessarily give an unacceptable result as demonstrated in [38]. The conservative approach enforces conservation of energy but loses consistency when the structural mesh is finer than the fluid mesh [40]. It generally guarantees consistency when the fluid mesh is finer than the structural mesh which is the case for UNDEX where the cavitation effect needs to be captured. It has been suggested that the energy conservation is of little importance for a short-duration shock wave transient simulation [34], [41]. However, no quantification of this is found in the literature.

The CASE has previously been coupled to the structure by an average mapping technique which maps the average pressure and displacement fields in [27]. Although this method features straightforward implementation, high-pressure gradients induced by the oblique shock wave are smoothed. Thus, the accuracy of the peak velocity prediction may suffer. It has not been demonstrated whether CASE would preserve superior behavior if a more rigorous information mapping scheme (e.g., consistent scheme) is used.

In the research described in this paper, we employ the basic ideas of CAFE and CASE for the fluid modeling and couple them to an Abaqus explicit structural solver. As a preliminary step to applying our approach to a full surface ship problem, we use a Floating Shock Platform (FSP) problem to show the potential relative computational advantage in far-field surface ship UNDEX problems. In addition, consistent, average and energy-conservative mapping schemes are explored and compared to determine which is the most cost-effective approach.

2.2 Description of the FSI framework, structure and fluid model

2.2.1 Coupled FSI framework through MpCCI

In this section, we present a partitioned FSI framework for the far-field UNDEX problem. On the structural side, we use the Abaqus Explicit solver which features explicit-time integration. For the fluid solver, the CAFE and CASE methodologies are implemented in our own fluid solver in C++. For the coupling between fluid and structural solvers, MpCCI [42], a multi-physics coupling software is utilized. MpCCI supports most state-of-the-art commercial solvers and our in-house code. Abaqus is coupled through its Co-simulation Engine, and the in-house code is coupled through MpCCI API functions. The details regarding the resolution of non-matching meshes and time-step size are introduced later in this section. The skeleton of the coupled framework is shown in Figure 2.1.

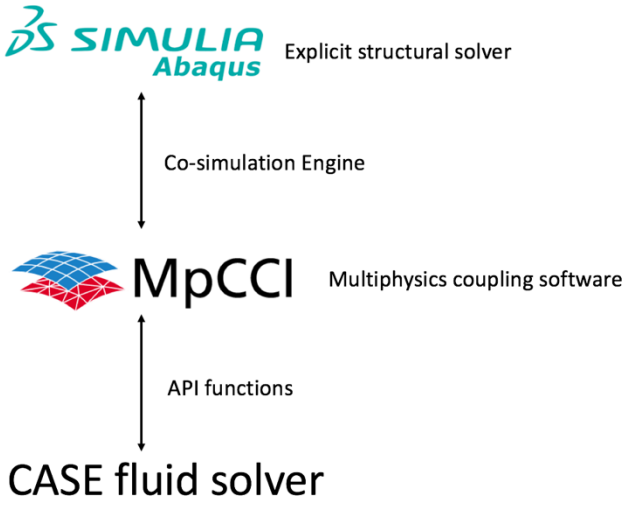

Figure 2.1 Partitioned FSI framework

2.2.2 Abaqus (Explicit) Structural solver

Since an important effect of the far-field UNDEX problem is the structural oscillation caused by the stress wave propagation after the shock impact, Abaqus Explicit is chosen due to its advantage in solving problems with transient high-speed events. In comparison, the implicit solver (Abaqus Standard) is more suitable for the low-speed phenomenon like structure dynamic motion after the shock wave effect is gone. The semi-discretized structural motion is expressed in Eq. 2.1.

$$M\ddot{x} + Kx = f \tag{2.1}$$

The mass matrix is lumped to save memory and facilitate an explicit central difference Newmark scheme detailed in [24].

2.2.3 Cavitating Acoustic Spectral/Finite Element Method (CASE/CAFE)

In this section, we describe the governing equations and spatial discretization of the CASE/CAFE framework which are adapted from [16], [27], [31].

The far-field assumption allows the acoustic treatment of the shock wave propagation. Although the acoustic fluid is compressible, we assume the fluctuations between the density ρ and reference density ρ_0 are small, thus allowing the continuity equation based on dynamic displacement $\vec{x}$:

$$\frac{\partial \rho}{\partial t} + \nabla \cdot \left(\rho \frac{\partial \vec{x}}{\partial t} \right) = 0 \tag{2.2}$$

to be linearized using total condensation $S = \frac{\rho}{\rho_0} - 1$ for $|S| \ll 1$

$$\frac{\partial S}{\partial t} + \nabla \cdot \left(\frac{\partial \vec{x}}{\partial t} \right) = 0 \tag{2.3}$$

Neglecting the viscosity and convection term, the Euler momentum equation for the acoustic fluid is written as:

$$\rho_0 \frac{\partial^2 \vec{x}}{\partial t^2} = \rho_0 \vec{f} - \nabla p^t \tag{2.4}$$

where p^t is the total fluid pressure, and $f(\vec{X})$ is the body force field.

In this work, we apply the Total Field Formulation (TFM) which comprises the incident, scattered and static field following the approach from [16]. The incoming shock wave causes the incident field, and its reflection from the boundaries (i.e., structure and free surface) generates the scattered field. The static field is the hydrostatic field of the fluid. The primary variables of TFM only contain the incident and the scattered field, which in combination is called the dynamic field. The static field is not modeled since it is known for all time.

Using the relationship $-\nabla \psi = \rho_0 \vec{x}$ based on irrotational fluid assumption, the governing equations, Eq. 2.3 and Eq. 2.4, are converted to the form in Eq. 2.5 and Eq. 2.6:

$$s = \nabla^2 \psi \tag{2.5}$$

$$\frac{\partial^2 \psi}{\partial t^2} = \begin{cases} c^2 s, & s > \dfrac{(p^{cav} - p_{eq})}{c^2} \\ p^{cav} - p_{eq}, & Otherwise \end{cases} \tag{2.6}$$

where s is the dynamic condensation and ψ is the dynamic displacement potential related to the dynamic pressure by $p = \ddot{\psi}$. Eq. 2.6b enforces a cut-off cavitation condition which stops the total pressure going below vapor pressure p_{cav} once cavitation begins. The vapor pressure is small enough to be negligible. p_{eq} is the static field pressure.

Following the standard Galerkin approach, we multiply the Eq. 2.5 by test function ϕ and integrate it over the fluid domain Ω_f:

$$\int_{\Omega_f} [s\phi - \nabla^2 \psi \phi] d\Omega = 0 \tag{2.7}$$

Applying the Green's first identity to Eq. 2.7 yields the weak form:

$$\int_{\Omega_f} s\phi d\Omega + \int_{\Omega_f} \nabla \psi \cdot \nabla \phi d\Omega = \int_{\Gamma_f} \phi \nabla \psi \cdot \vec{n} d\Gamma \tag{2.8}$$

where Γ_f denotes the fluid boundary and $\vec{n}$ is the outward pointing normal vector on the boundary.

Due to the fact that the fluid mesh is comprised of all hexahedral elements, the densified condensation and displacement potential can be written over an element as

$$s(\xi,\eta,\zeta,t) = \phi^T s(t) = \sum_{i,j,k=1}^{N+1} \phi_i(\xi)\phi_j(\eta)\phi_k(\zeta)s_{ijk}(t) \tag{2.9}$$

$$\psi(\xi,\eta,\zeta,t) = \phi^T \psi(t) = \sum_{i,j,k=1}^{N+1} \phi_i(\xi)\phi_j(\eta)\phi_k(\zeta)\psi_{ijk}(t) \tag{2.10}$$

where ϕ is the column vector of the 1D spectral basis function $\phi_i(\xi), \phi_j(\eta), \phi_k(\zeta)$. For the CASE elements, the interpolation point and quadrature point are both chosen as Gauss-Lobatto-Legendre (GLL), thus allowing the mass matrix to be fully diagonal. This is the essential difference between the CASE and CAFE elements which use equally spaced interpolation point and Gauss-Legendre quadrature nodes. As a result, the mass matrix is not diagonal. For the sake of fast computation in the CAFE explicit temporal integration, the mass matrix is diagonalized by row-sum technique.

Substituting Eq. 2.9 and Eq. 2.10 into the weak form (Eq. 2.8) gives:

$$Qs + H\psi = b \tag{2.11}$$

where $Q = \int_{\Omega_f} \phi\phi^T d\Omega$, $H = \int_{\Omega_f} \nabla\phi \cdot \nabla\phi^T d\Omega$, $b = \int_{\Gamma_f} \phi\nabla\psi \cdot \vec{n} d\Gamma$. Following the nomenclature in [16], we name Q the global capacitance matrix, H the global reactance matrix and b the global fluid force vector. The governing equation (Eq. 2.6) is evaluated in a node-by-node fashion:

$$\ddot{\psi} = \begin{cases} c^2 s|i, & s|i > -p_{eq}|i/c^2 \\ p^{cav} - p_{eq}, & otherwise \end{cases} \quad i = 1,2,\dots n_{node} \tag{2.12}$$

The boundary conditions to be prescribed are at the free surface, fluid-structure interface and non-reflecting boundary (NRB). At the free surface, the essential boundary condition is imposed as:

$$p = 0 \tag{2.13}$$

The fluid-structure interaction and NRB terms are natural boundary conditions governed by the fluid force vector b which can be expressed as:

$$b = b^s + b^{nrb} \tag{2.14}$$

where:

$$b^s = \int_{\Gamma_{fs}} \phi\nabla\psi \cdot \vec{n} d\Gamma_{fs} = \int_{\Gamma_{fs}} \phi \frac{\partial\psi}{\partial n} d\Gamma_{fs} = -\rho_0 \int_{\Gamma_{fs}} \phi\phi^T x^s d\Gamma_{fs} \tag{2.15}$$

where x^s is the displacement vector of the structure along the normal direction of fluid-structure interface taken as positive into the fluid. By the same principle,

$$b^{nrb} = -\rho_0 \int_{\Gamma_{nrb}} \phi\phi^T x^{nrb} d\Gamma_{nrb} \tag{2.16}$$

where x^{nrb} is the displacement of NRB approximated by Curved Wave Approximation [29]:

$$x^{nrb} - x^{eq} = \left(\frac{1}{\rho_0 c}\Theta p^*_{inc} + \frac{1}{\rho_0}\Theta R^{-1} p^{**}_{inc}\right) + \frac{1}{\rho_0 c}\left(p^* - p^*_{eq} - p^*_{inc}\right) + \frac{\kappa}{\rho_0}(p^{**} - p^{**}_{eq} - p^{**}_{inc}) \tag{2.17}$$

where $p = p_{inc} + p_{sc}$, x_{eq} is the displacement at equilibrium, Θ is the cos value of the angle between the incident shock direction and the outward norm $\vec{n}$. κ represents the mean curvature of the NRB. The terms in the first bracket represents the displacement caused by the incident wave and the terms in the second bracket is the approximation of the displacement caused by the

scattered wave. Since the NRB used in later investigation is planar ($\kappa = 0$), the last term is dropped.

2.2.4 Non-conformal fluid-structure mesh coupling

Due to the discontinuity of the shock wave and nonlinear cavitation effect, the fluid mesh must typically be finer than the structural mesh. To facilitate the mapping between non-matching meshes by the methods introduced in this chapter, a general purpose searching and projection algorithm is implemented. The node of interest from the fluid (structure) surface mesh is first paired with the nearest element on the structure (fluid) surface mesh. Then, the node is orthogonally projected onto the paired element. The local coordinate of the projected node is determined to facilitate the later interpolation. If the projection fails, the value of the closest node on the target mesh is directly used. To handle the interpolation of pressure and displacement field, three aforementioned different DFMT mapping algorithms are introduced below.

2.2.4.1 Consistent and average mapping algorithm

The consistent mapping scheme follows a straightforward implementation by projecting the target nodes to the source mesh and then interpolating the desired properties using the local shape function. Specifically, the structural quadrature nodes χ_i (i.e., Gauss-Legendre) are mapped to the fluid mesh to obtain the interpolated pressure (Eq. 2.18) and the displacement is obtained by projecting the fluid nodes on the structure mesh and interpolating using the local structural shape function (Eq. 2.19).

$$p_{\chi_i} = \sum_{j=1}^{j=n_f} N_j(\chi_i) p_j \tag{2.18}$$

$$u_j = \sum_{i=1}^{i=n_s} N_i(\chi_j) u_i \tag{2.19}$$

where i denotes the nodes on structure element and j on fluid element, p is the pressure and u is the nodal displacement, n_s and n_f are the node number on structure and fluid element and N is the shape function. In Figure 2.2, we use a 3rd order CASE element coupled to linear structural element as an illustration of this method.

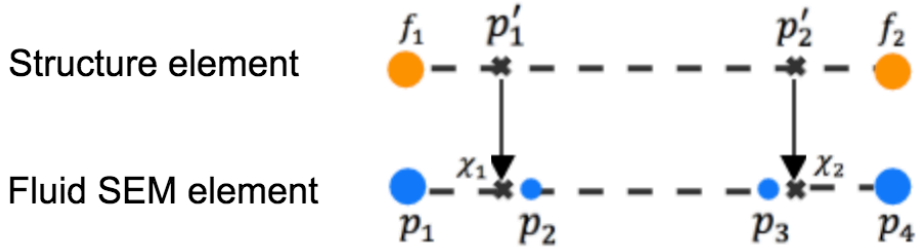

Figure 2.2 Consistent mapping algorithm

For the average mapping algorithm in [27], the pressure and displacement interpolations are further loosened by taking their averaged values (Eq. 2.20) (Eq. 2.21). Thus, the searching and projection routine is simplified since the local coordinate of the projected node is no longer required. Only the pairing relationship between the node and target element is needed.

$$p_{\chi_i} = \overline{p}_j \tag{2.20}$$

$$u_j = \overline{u}_i \tag{2.21}$$

The consistent and average mapping approaches do not attempt to guarantee the force and further energy conservation. The level of conservation depends on the number of Gauss points used.

2.2.4.2 Energy conservative mapping algorithm

From the virtual work balance derivation in [38], the nodal force (i.e., pressure flux) mapping matrix must be transposed to the displacement mapping matrix in order to guarantee energy conservation. For instance, if we use the consistent mapping for displacement, then we have to use the same shape function (i.e., the shape function of the structural element) to interpolate the nodal force. Thus, for the fully consistent mapping approach in Section 2.2.4.1, energy conservation is not guaranteed since the mapping matrices are not related.

In the later context, we interpolate the displacement using the consistent approach (Eq. 2.22):

$$u_j = \sum_{i=1}^{i=n_s} N_i(\chi_j) u_i \tag{2.22}$$

Then, the received nodal force f_i on the structure element becomes:

$$f_i = \sum_{j=1}^{j=n_f} \phi_j N_i(\chi_j) \tag{2.23}$$

in which χ_j is the local coordinate of the mapped n_f fluid nodes on the structure element and ϕ_j is the nodal force on the fluid element which can be represented as:

$$\phi_j = \int_{\Gamma_f^e} N_j p \vec{n} ds, \qquad j \in \Gamma_f^e \tag{2.24}$$

where Γ_f^e is the fluid surface.

Based on the unit summation property of the shape function (i.e.,$\sum_{i=1}^{i=i_e} N_i(\chi_j) = 1$), the total received force f_t^s by structure element becomes:

$$f_t^s = \sum_{i=1}^{i=n_s} f_i = \sum_{i=1}^{i=n_s} \sum_{j=1}^{j=n_f} \phi_j N_i(\chi_j) = \sum_{j=1}^{j=n_f} \phi_j \tag{2.25}$$

Thus, the total force is conservative as well. In Figure 2.3, we use a 3rd order CASE element coupled to linear structural element as an example for the energy conservative mapping algorithm derivation.

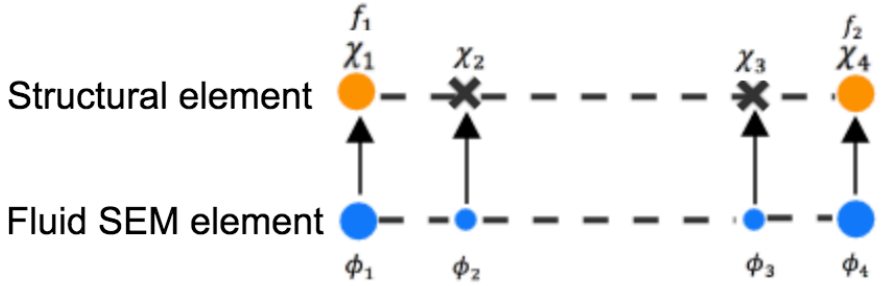

Figure 2.3 Energy conservative mapping algorithm

2.2.5 Temporal discretization

The governing equations of the CAFE/CASE framework are integrated in time by a staggered second-order explicit central difference scheme (a.k.a. Leapfrog scheme) introduced by Felippa and DeRuntz [16]. The approximation of critical time increment is given as:

$$\Delta t_{crt} = \frac{2}{c\sqrt{\lambda_{max}(1+2\beta)}} \tag{2.26}$$

where λ_{max} is the maximum fluid mesh eigenvalue estimated by Gershgorin's theorem [29] for CAFE/CASE elements and β is the artificial damping factor used to mitigate the spurious oscillation. Half of the critical time increment ($CFL = 0.5$) is used in the cases hereafter.

The non-matching time step interpolation is performed by a monotone cubic Hermite spline implemented in MpCCI to achieve a 3rd order interpolation accuracy [42]. Different from the sub-cycling approach, the current approach does not require either solver to cut the time increment to make the ratio integer, thus allowing them to advance at their own optimal step size. Also, this would make the later comparison of CASE and CAFE elements more consistent by keeping the CFL number constant. This idea is illustrated in Figure 2.4.

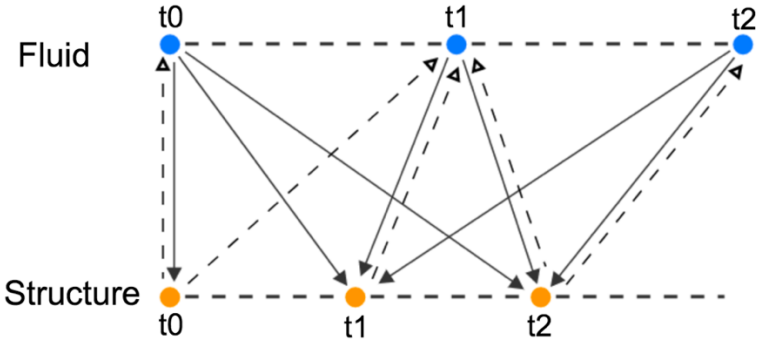

Figure 2.4 time step interpolation

2.3 Numerical results and assessment

In this section, we first present a preliminary model assessment and then demonstrate which type of fluid element has the highest computational efficiency for the Floating Shock Platform UNDEX problem.

2.3.1 Model assessment

In this section, the model and FSI framework introduced in Section 2.2 is assessed using two benchmark problems. The linear CASE element is used in the in-house fluid solver and the consistent mapping algorithm is adopted for the non-matching mesh interpolation. Excellent agreement with the baseline results provides more confidence in the model setup employed for the numerical experiment described in later sections.

2.3.1.1 Bleich-Sandler Problem

The Bleich-Sandler plate [43] is a classic UNDEX benchmark problem with cavitation. The problem includes a rigid plate sitting on the free surface of an infinitely deep fluid column (Figure 2.5). The plate is subject to the load from a step exponential plane shock wave in Eq.

2.27 where P_{peak} is the peak pressure on the shock front, c is the speed of sound, τ is the decay constant and x_{so} is the initial location of the shock front at $t = 0$. The plate is kicked off by the incident shock wave, which then causes the cavitation. The plate gravity and the atmospheric pressure acting on top of the plate causes the velocity to decrease to the extent that the motion is reversed. The cavitation eventually closes as the pressure is restored and the plate rebounds. The cavitation collapse emits a pressure impulse which leads to a reloading of the plate. The solution by the method of characteristics is given in [43] and chosen as the benchmark.

$$p_{inc}(x,t) = P_{peak} \exp\left[-\frac{t + \frac{x - x_{so}}{c}}{\tau}\right] H\left(t + \frac{x - x_{so}}{c}\right) \tag{2.27}$$

Although the problem was originally in 1D, we use a 3D configuration to validate our in-house framework (Figure 2.5). The plate is modeled in Abaqus by a rigid element and coupled with the fluid solver using MpCCI. To limit the size of the fluid domain, the plane non-reflective boundary is prescribed at the bottom of the fluid column. No boundary condition is defined on the sides since they are symmetry boundaries. The detailed parameters are presented in Table 2.1. We compare our numerical result with the benchmark solution in Figure 2.6. The result shows excellent agreement between the in-house solver and benchmark solution with an L2 error norm of 0.0322. The L2 error norm used in this case is defined as:

$$L_2 = \frac{\sqrt{\int_0^{t_{term}} \left[V_{benchmark}(t) - V_{computed}(t)\right]^2 dt}}{\sqrt{\int_0^{t_{term}} [V_{benchmark}(t)]^2 dt}} \tag{2.28}$$

where $V_{benchmark}(t)$ is the benchmark solution time history, $V_{computed}(t)$ is the computed solution time history and t_{term} is the total simulation time.

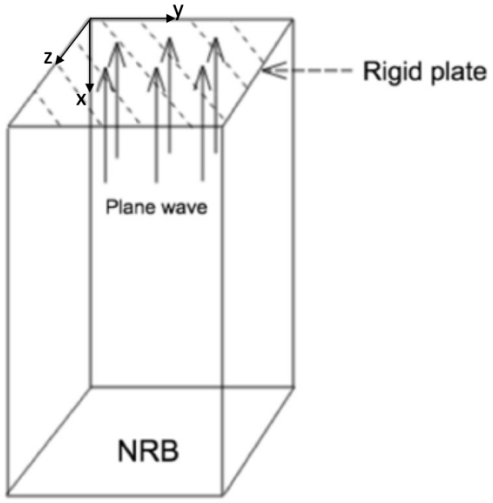

Figure 2.5 Bleich-Sandler configuration

Table 2.1 Bleich-Sandler parameter configuration

Parameters	Value
Plate weight	144 kg
Fluid domain size	0.1 m*3.8 m*0.1 m
Fluid mesh size	0.025 m in y&z 0.0175 m in x
Shock wave peak pressure (P_{peak})	0.712 Mpa
Shock wave decay rate (τ)	0.999 ms
Initial location of the shock front (x_{so})	0 m

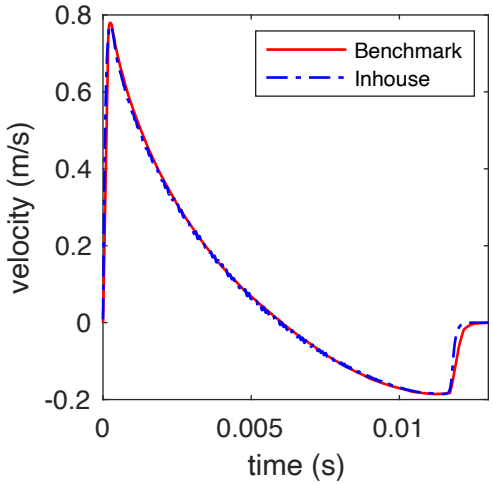

Figure 2.6 Comparison of structural response of the in-house solver and benchmark solution (13ms)

2.3.1.2 Floating Shock Platform

In this section, we further assess model and FSI framework in a MILS-901D standard Floating Shock Platform (FSP) [44] application with an incident spherical step exponential shock wave (Eq. 2.29) initiated when the shock wave would contact the nearest structure point to the explosive. The incident shock wave pressure is specified as:

$$p_{inc}(\boldsymbol{X},t) = P_{peak}\exp\left[-\frac{t-\frac{R-R_0}{c}}{\tau}\right]H\left[t-\frac{R-R_0}{c}\right] \tag{2.29}$$

where R is the distance from the charge center to the point $\boldsymbol{X}$ and R_0 denotes the initial wave radius at the nearest structure point. The peak pressure P_{peak} and decay rate τ are calculated from the similitude equation from [45], [46].

Since precise experimental data are not available, we assess our results by comparison to a numerical solution calculated by the Abaqus structural-acoustic solver which couples a FEM based acoustic fluid solver with the Abaqus structural solver. In Abaqus, we employ a CAFE-like approach using the same cut-off cavitation condition and non-reflective boundary condition as used in our fluid solver. The major difference from the CAFE approach is that the linear acoustic fluid element in Abaqus is pressure-based instead of using displacement potential. The non-matching mesh interpolation is performed by the node-to-surface constraint function in Abaqus

which uses the same principle with energy conservative mapping algorithm as described in Section 2.2.4.2. The size of the fluid domain is set so that the bulk cavitation caused by the free surface is captured as shown in the Figure 2.7. The lower bulk cavitation boundary indicated by the red curve is calculated by the algorithm described in [11] assuming the structure is not present. Since the explosive is located directly below the longitudinal center of the FSP, only half of the fluid and structure domain is modeled. A simulation screenshot is shown in Figure 2.8. The detailed parameters are listed in Table 2.2.

The same FSP structure is modeled in our framework and coupled to fluid solver using MpCCI. The same base fluid mesh is used as in Abaqus, but with linear CASE elements. The results are compared at two points. The first point 1646 (-1.8288m, 0m, -0.3048m) is at the top of an athwartship girder and the second point 2320 (-0.3048m, 0m, 0.3048m) is at the center of a stiffened plate. The simulation result of the in-house CASE solver agrees well with the Abaqus acoustic-structure solver solution as shown in Figure 2.9. In order to quantify this comparison, an error norm is used. The error norm is calculated using the approach introduced by Russel [47] which is frequently used for structural vibration problems. The comprehensive error factor ϵ_c is obtained by combining the magnitude error factor ϵ_m and phase error factor ϵ_p together:

$$\epsilon_c = \sqrt{\frac{\pi}{4}\left(\epsilon_m^2 + \epsilon_p^2\right)} \tag{2.30}$$

The expression for ϵ_m and ϵ_p can be found in [47]. Using the Abaqus results as the baseline, the Russel error norm of the in-house solution is 0.0985 at point 1646 and 0.0982 at point 2330, which is satisfactory. The trend at point 1646 is similar to the Bleich-Sandler result which is identified by an initial kick-off caused by the incident wave, panel rebound and the reloading from cavitation collapse. The velocity response at point 2320 in both models shows a relatively low-frequency large-amplitude oscillation because the plate is unsupported at that location.

Table 2.2 Abaqus parameter configuration

Parameters	Value
FSP structure size (half)	4.2672m (14ft)*1.2192m (4ft)*4.8768m (16ft)
Fluid domain size	5.7912m (19ft)*3.6576 (12ft)*10.9728m (36ft)
Structural element type	4-node shell element (S4R)
Structural element size	0.3048m (1ft)
Fluid element type	8-node acoustic brick element (AC3D8R)
Fluid element mesh size	0.0762m (0.25ft)
Charge Stand-off distance	9.144m (30ft)
Charge depth	3.048m (10ft)
Shock wave peak pressure	16.22 Mpa
Shock wave decay rate	0.3208ms

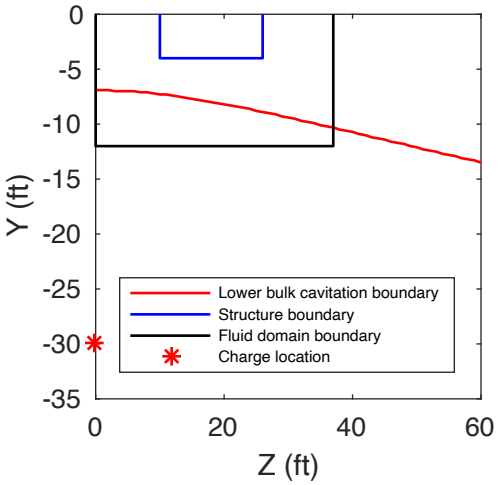

Figure 2.7 Problem configuration

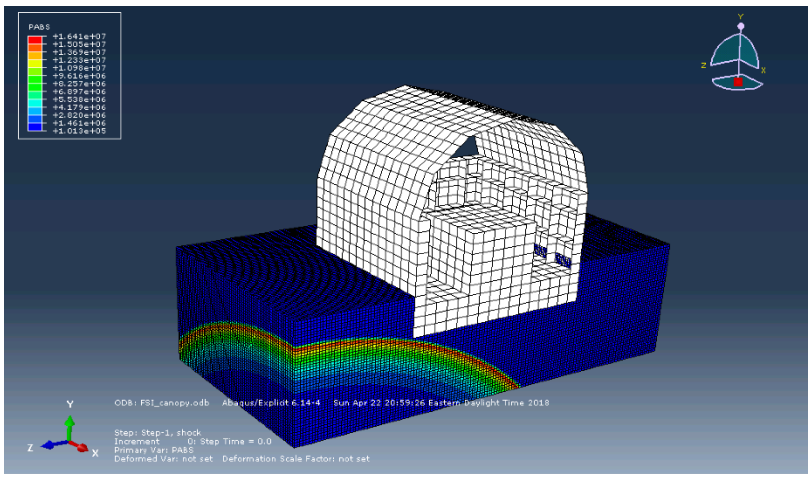

Figure 2.8 FSP Abaqus configuration

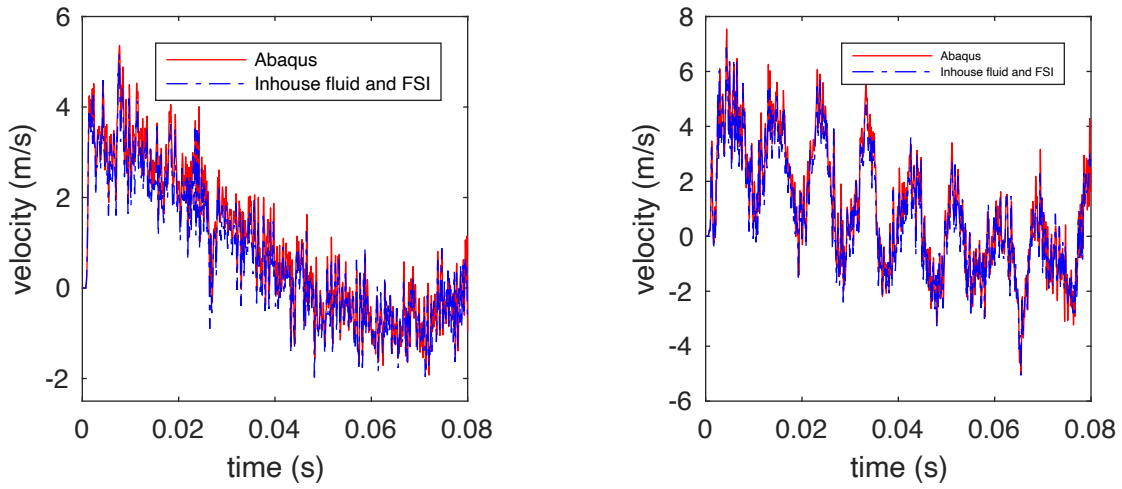

(a) Point 1646 (b) Point 2320

Figure 2.9 Comparison of structural response of in-house FSI framework and Abaqus/Explicit

2.3.2 Comparison of CAFE and CASE elements

This section compares the behavior of linear finite elements (linear CAFE), linear spectral elements (linear CASE) and high-order spectral elements (high-order CASE) using our in-house solver in the same FSP case configuration used in Section 2.3.1.2. The result at point 1646 is used for plotting and analysis. We add a damping factor $\beta = 0.25$ to mitigate the spurious oscillation caused by the cavitation. For all methods, we use a base fluid mesh of 7312 0.3048m (1ft) cubic hexahedral elements. H refinement (linear CAFE and linear CASE) and p refinement (high-order CASE) are performed on the base fluid mesh. The DOF and time increment are shown in the Table 2.3. Based on our previous convergence study, an $N = 8$ CASE solution is used as the numerical benchmark to quantify the accuracy of the structural response. We first compare the accuracy of structural response to the benchmark using different types of fluid elements and then assess the behavior by plotting the cavitation distribution. The consistent mapping approach described in Section 2.2.4.1 is used for the cases throughout this section.

2.3.2.1 Operation count calculation

An operation count is used to quantify computational cost. Due to the large memory usage of storing the global reactance matrix H, the matrix-vector product $(H\psi)$ is typically conducted on the element level $(H^e\psi^e)$ and then assembled. The operation count involved in directly multiplying matrix H^e and vector ψ^e (direct-matrix product) is:

$$2(N+1)^6 - (N+1)^3 \tag{2.31}$$

where N is the CASE element order. Only the floating point operations (FLOP) are counted since the assignment operation, and logical operation is subjective based on different implementations.

However, for the high-order CASE element, the $O(N^6)$ operation is very inefficient. Following the algorithm detailed in [29], we employ tensor-product factorization (T.F.) for the matrix-vector multiplication $(H^e\psi^e)$ which features $O(N^4)$ operation (FLOP shown in Eq. 2.32).

$$12(N+1)^4 + 15(N+1)^3 \tag{2.32}$$

We plot the FLOP of an element with CASE p refinement and CAFE/CASE h refinement in Figure 2.10 using the direct-matrix product and tensor-product factorization. As shown in Figure 2.10, using tensor-product factorization significantly lowers the FLOP of high-order CASE but does not help with linear CAFE/CASE. Thus, we decide to use direct-matrix product for linear CAFE/CASE and tensor-product factorization for high-order CASE elements.

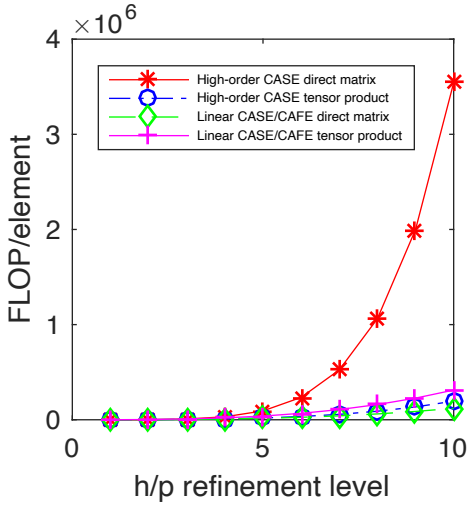

Figure 2.10 FLOP comparison

The FLOP in Eq. 2.31 and Eq. 2.32 are used to represent the total operation count of one element in a single time step since the other operations (e.g., boundary term calculation) are marginal in comparison. As a result, the total FLOP for the fluid solver can be represented by:

$$ndt * NEL * (2(N + 1)^6 - (N + 1)^3) \tag{2.33}$$

for linear CAFE/CASE and

$$ndt * NEL * (12(N + 1)^4 + 15(N + 1)^3) \tag{2.34}$$

for high-order CASE where NEL denotes total element number and ndt the total number of time steps.

2.3.2.2 Comparison of structural response accuracy

In this section, we compare the accuracy with the different types of elements to the benchmark using the structural velocity response. The Russel error norm (Eq. 2.30) of the structural response is compared to the degree of freedom (Figure 2.11). This comparison indicates that the error norm for high-order CASE is smaller than the linear CASE which is smaller than linear CAFE with the same DOF. Furthermore, the error decreases faster with DOF in the high-order CASE case. Since the time increment of high-order CASE is significantly smaller than the other element types (Table 2.3), it is necessary to plot the total FLOP against error norm to quantify their relative computational efficiency.

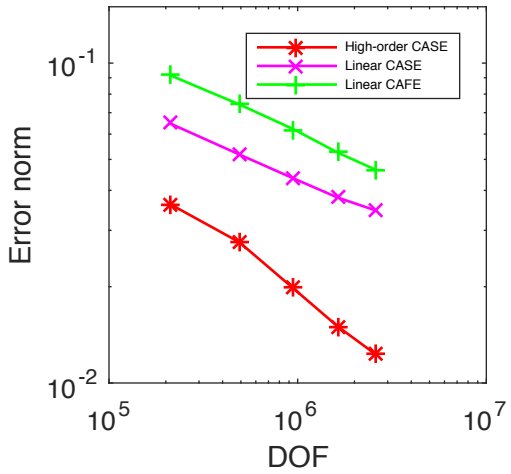

Figure 2.11 Error norm comparison for different element types with respect to DOF

Table 2.3 DOF and time increment (s) of different refinement levels

Refinement level	DOF	CAFE [s]	linear CASE [s]	CASE [s]
3	210226	2.39473e-05	1.59649e-05	8.70518e-06
4	490637	1.79605e-05	1.19737e-05	5.29987e-06
5	949336	1.43684e-05	9.57894e-06	3.56347e-06
6	1630195	1.19737e-05	7.98245e-06	2.55908e-06
7	2577086	1.02631e-05	6.8421e-06	1.92626e-06

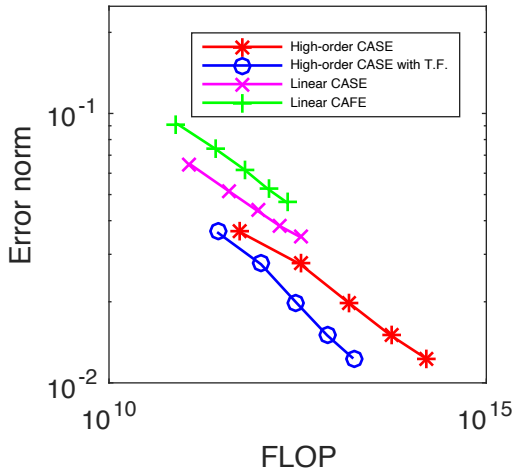

Figure 2.12 Operation count comparison for different element types with respect to FLOP

As shown in Figure 2.12, the high-order CASE with tensor-product factorization achieves the highest accuracy compared to the benchmark with the same number of FLOP. The computational efficiency of high-order CASE is superior even without tensor-product factorization (direct-matrix product). Thus, the high-order CASE may still be advantageous if an unstructured tetrahedral mesh without tensor product factorization is used. Linear CASE outperforms linear CAFE although inferior to the high-order CASE.

Next the behavior of high-order CASE elements of different order is investigated. *H* refinement for CASE elements with different order is used for this assessment. The base element size is increased to 0.6096m (2ft). A case with 8th order CASE-type *p* refinement and 2nd order *h* refinement is employed for the benchmark. Russell error factor is employed as in the previous cases. The case configuration and the corresponding DOF are listed in Table 2.4. The time increments for each case are presented in Table 2.5. The trend in Figure 2.13 shows the lower computational cost to achieve the same level of accuracy when the element order is higher.

Table 2.4 DOF of different refinement levels of CASE element

	p=2	p=3	p=4
h=1	-	29497	67881
h=2	64231	210226	490637
h=3	222325	735310	1725241
h=4	490637	1630195	3833881
h=5	1004541	3348961	-
h=6	1630195	-	-

Table 2.5 Time increment (s) of different refinement levels of CASE element

	p=2	p=3	p=4
h=1	-	1.74104e-05	1.05997e-05
h=2	1.69333e-05	8.70518e-06	5.29987e-06
h=3	1.12889e-05	5.80345e-06	3.53325e-06
h=4	8.46667e-06	4.35259e-06	2.64993e-06
h=5	6.77333e-06	3.48207e-06	-
h=6	5.64444e-06	-	-

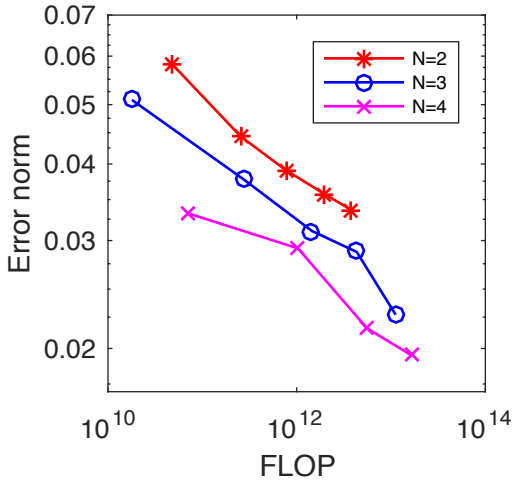

Figure 2.13 Operation count comparison for different high-order SEMs

2.3.2.3 Comparison of dynamic condensation distribution and cavitation region

In this section, the influence of cavitation region modeling on the accuracy of predicting structural response in the FSP problem is assessed. Our hypothesis is that the interaction between cavitation and structure plays an important role. We compare the dynamic condensation distribution in the depth direction under the center of the FSP bottom at various times (10ms, 20ms and 30ms) following the approach in [31]. A negative dynamic condensation indicates the extent of cavitation based on Eq. 2.12. Instead of the Russel error norm definition which is used for quantifying the norm of the oscillatory response history, we use the L2 error norm definition defined in Eq. 2.35.

$$L_2 = \frac{\sqrt{\int_0^d \left[s_{benchmark}(x,t) - s_{computed}(x,t)\right]^2 dx}}{\sqrt{\int_0^d [s_{benchmark}(x,t)]^2 dx}} \tag{2.35}$$

where d is the depth and x is the coordinate in depth direction. Again, the result of the $N = 8$ CASE solution is used as a benchmark.

The L2 norm for the h and p refinement levels from 4 to 6 are tabulated (Table 2.6 to Table 2.8), but only the 4th level h/p refined linear CASE, linear CAFE and high-order CASE of the same DOF are plotted for clarity (Figure 2.14) showing negative dynamic condensation and hence cavitation as a function of depth. The cavitation region initiates and grows as the FSP panel is displaced inward by the initial shock impact, leaving one cavitated region attached to the

structure and the other isolated in the fluid. The two cavitation regions keep growing and eventually merge at 30ms as the panel is still moving inward.

The error norm results show that high-order CASE gives a more accurate cavitation distribution than linear CASE which is better than linear CAFE, all compared to the benchmark. This reflects the strong association between the accuracy of cavitation modeling and structural response. However, much of the error in the dynamic condensation distribution is not observed in the velocity response of the structure. This is an indication that the disturbance below the first cavitation region may not affect the structure as much as the structural response is driven by the fluid directly attached to it. We may conclude that there is a need to accurately capture the shape and magnitude of cavitation regions in the fluid especially when directly in contact with the structure. Thus, high-order spectral elements may be advantageous in modeling the cavitated surface-ship problem due to their superior performance in modeling cavitation.

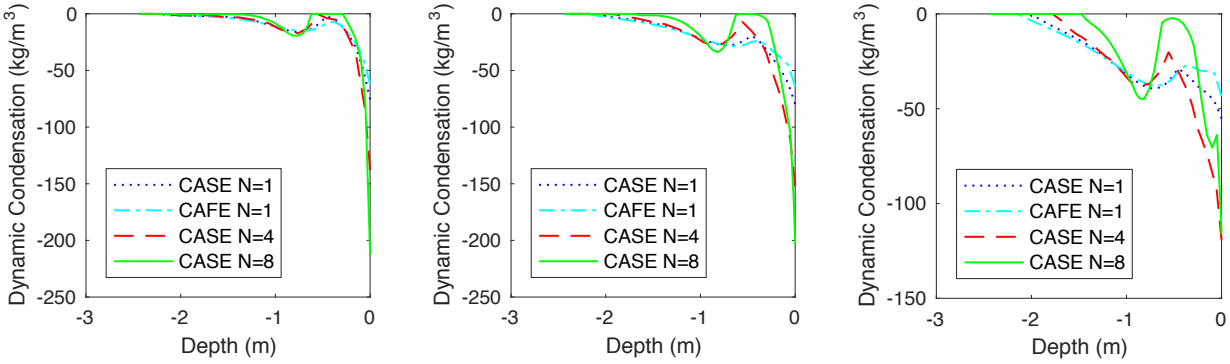

Figure 2.14 Dynamic condensation distribution at 10ms, 20ms and 30ms

Table 2.6 L2 norm of the dynamic condensation distribution at 10ms

Refinement level	Linear FEM	Linear SEM	High-order SEM
4	0.7840	0.7048	0.3517
5	0.6725	0.5645	0.2369
6	0.5947	0.4634	0.2759

Table 2.7 L2 norm of the dynamic condensation distribution at 20ms

Refinement level	Linear FEM	Linear SEM	High-order SEM
4	0.7301	0.6352	0.3775
5	0.6391	0.5227	0.2406
6	0.5757	0.4446	0.2015

Table 2.8 L2 norm of the dynamic condensation distribution at 30ms

Refinement level	Linear FEM	Linear SEM	High-order SEM
4	0.6757	0.5948	0.5240
5	0.6108	0.5222	0.2900
6	0.5759	0.4981	0.2085

2.3.3 Comparison of different mapping algorithms for CASE

In the previous section, it is shown that the computational advantage of high-order CASE is preserved with the consistent mapping algorithm. In this section, three different non-matching mesh mapping approaches (consistent, average and energy conservation) are compared to determine which one is the most efficient. The position of the sampling point (pt. 5084) is identical to the point 1646 in the previous section which is on the athwartship stringer in the FSP.

2.3.3.1 The comparison between the consistent mapping and average mapping schemes

In this section, a comparison between the consistent and the average mapping algorithms is made. In order to assess the difference, four fluid mesh configurations using CASE elements of various order are used, as shown in Figure 2.15. The base structural mesh stays the same at 0.1524m (0.5ft) for all the cases. In the first case, fluid mesh uses a 0.1524m (0.5ft) base element with 2nd order h refinement; the second case uses a 0.3048m (1ft) base element with 2nd order h refinement (matching fluid and structure mesh); the third case uses a 0.1524m (0.5ft) base element with 2nd order p refinement; the fourth case uses a 0.3048m (1ft) base element with 2nd order p refinement. Cases 1 and 3, and cases 2 and 4 have the same degree of freedom.

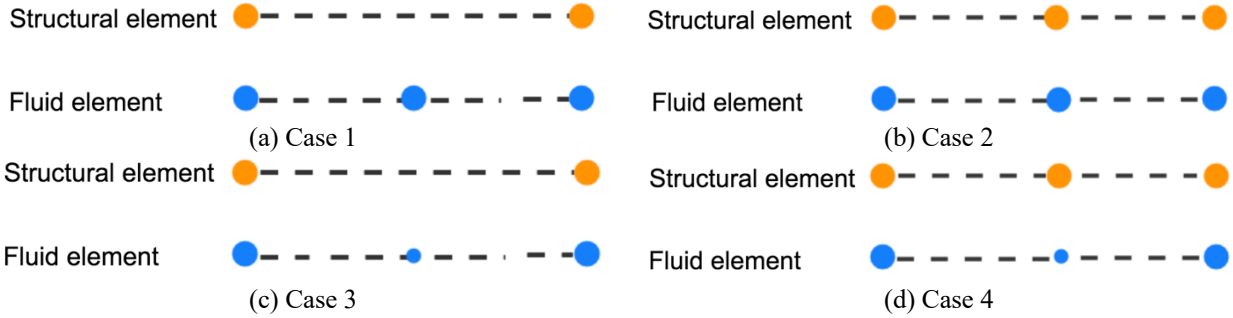

Figure 2.15 Mesh configuration for case 1 to 4

Instead of directly comparing the response history, we compare the shock response spectrum (SRS) calculated from the acceleration time history. The SRS is important in describing ship shock response especially in terms of ship equipment design. Using different mapping schemes on the fluid-structure wetted surface may alter the oscillation pattern which may then cause large differences in the SRS. The SRS plots in this section are generated by a MATLAB code created by Irvine [48] using the Smallwood algorithm. An amplification factor $Q = 10$ and the 1Hz sampling rate are applied. The Case 3 with consistent mapping result is used as benchmark since we have already shown that higher order elements with higher DOF have better accuracy. The SRS for Cases 1 to 4 are plotted in Figure 2.16 from 0.1 to 300 Hz which is a typical upper limit for shipboard shock analysis [49]. The L2 error norm of the four cases is presented in Table 2.9. The SRS result L2 norm difference between consistent and average mapping for each case is presented in the Table 2.10.

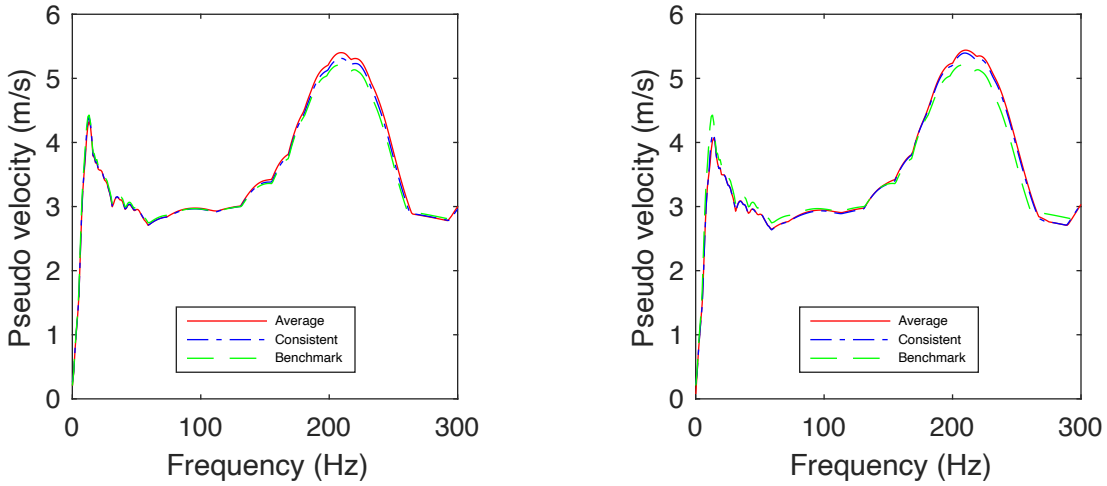

(a) Case 1 (b) Case 2

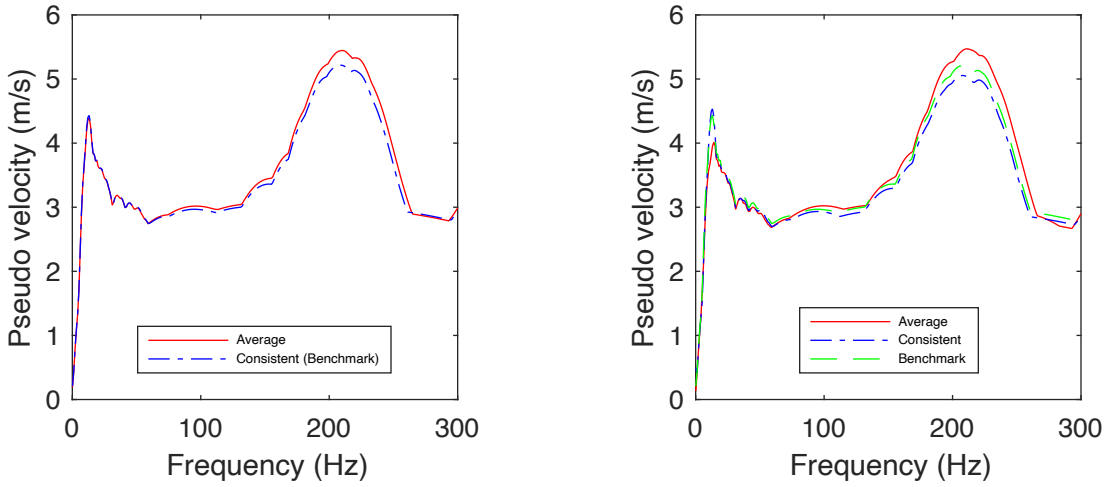

(c) Case 3 (d) Case 4

Figure 2.16 Shock response spectrum of case 1 to 4

Table 2.9 L2 error norm for case 1 to 4

	Average mapping	Consistent mapping
Case 1	0.02830	0.01567
Case 2	0.04442	0.03863
Case 3	0.03245	Benchmark
Case 4	0.04577	0.02618

Table 2.10 Difference between consistent and average mapping (L2 norm)

	0.1524m (0.5ft)	0.3048m (1ft)
h=2	0.01319 (Case1)	0.008317 (Case 2)
p=2	0.03245 (Case3)	0.06684 (Case4)

The L2 error norm in Table 2.9 indicates that the consistent mapping algorithm gives a better (lower error norm) result than average mapping in the cases tested. This result makes sense

because the displacement/pressure value on quadrature points is more accurate in the consistent mapping case. Average mapping generally overpredicts the peak velocity in the shock response spectrum as shown in Figure 2.16.

If we proceed with the conclusion that consistent mapping gives better results in all the cases, we can treat the L2 norm in Table 2.10 as the extra mapping error introduced by the average mapping since it is essentially a simplification of the consistent mapping. For the matching mesh configuration (Case 2), the difference between consistent and average mapping is the smallest. The difference becomes larger as the fluid element size is increased (Case3 vs Case4). The high-order CASE element shows a larger difference than the linear element with the same DOF (Case1 vs Case3). Overall, the performance of average mapping becomes poorer for fluid elements with larger size and higher order, which is the case for high-order CASE elements.

2.3.3.2 The comparison between conservative and consistent schemes

In this section, the behavior of the consistent mapping scheme is compared to the energy conservative scheme to examine the importance of energy conservation. The difference between the two algorithms is that energy conservation is not guaranteed by the consistent approach as demonstrated in Section 2.2.4. However, energy conservation may not be important for a short-duration problem such as in far-field UNDEX which usually lasts less than 100ms. To demonstrate the problem, a 3rd order CASE fluid mesh coupled with the linear structural mesh of the same element size 0.1524m (0.5ft) as presented in Figure 2.3 is used. For the consistent mapping, we use linear Gauss-Legendre quadrature on the structural element which guarantees total force conservation but is theoretically unable to achieve energy conservation theoretically. Although consistency is normally violated for the conservative scheme [50], the nested fluid mesh configuration used in this case guarantees consistency by passing the aforementioned patch test as described in Section 2.1.3.

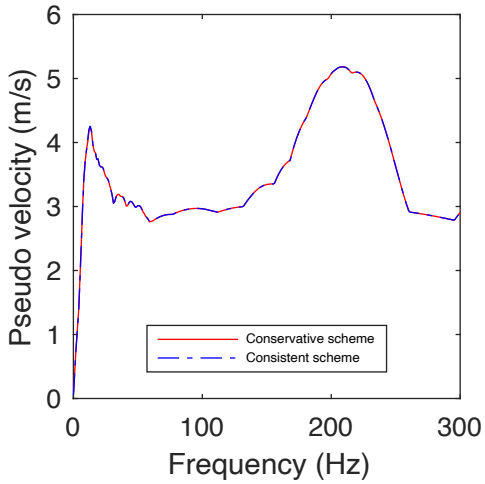

Figure 2.17 Comparison between consistent and energy conservative approach in SRS

The SRS comparison in Figure 2.17 shows that there is almost no difference in structural response between the consistent and conservative method. We track the total energy input (positive) / received (negative) by fluid and received/input by the structure in the consistent method. The energy history in Figure 2.18 indicates that the consistent mapping approach essentially conserves the total energy in this application. This supports the assertion made in [41] that an energy conservation scheme might be of little significance in short-duration problems

involving shock. Also, given the knowledge that an energy conservative method can violate consistency if the fluid elements are fully mismatched (not nested), the consistent mapping approach is sufficient and possibly superior for the far-field UNDEX application.

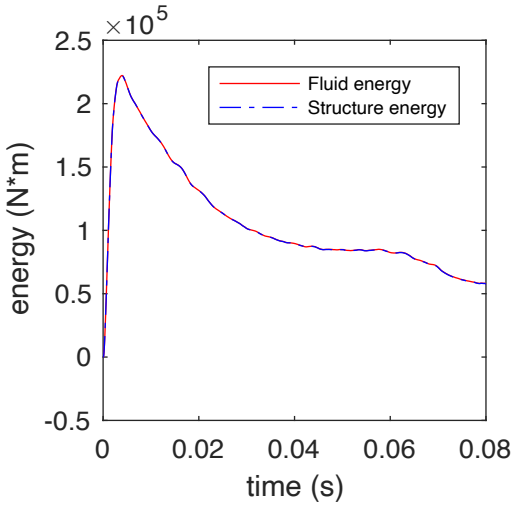

Figure 2.18 Energy history on fluid and structure interface

2.4 Conclusions

In this paper, research to apply, assess and improve the CASE algorithm in an early-time far-field UNDEX problem for application to surface ship problems is described. A partitioned fluid-structure interaction framework is assembled and assessed in two benchmark cases. Results are very good. The computational efficiency of linear finite element (linear CAFE), linear spectral element (linear CASE) and high-order spectral element methods (high-order CASE) using a floating shock platform case are compared. Three information exchange schemes (average, consistent and energy conservative) for the non-matching meshes are also compared.

The results show that superior computational efficiency is achieved with high-order spectral elements in the surface ship FSP far-field UNDEX problem with the consistent mapping approach even though a large cavitation region exists. The high-order CASE possesses the highest computational efficiency even without the use of tensor-product factorization. As the element order increases, the advantage of high-order CASE becomes larger. Although not as effective as high-order CASE, linear CASE still outperforms the fundamental linear CAFE. This result is due to the more accurate modeling of the cavitation region which significantly affects the accuracy of the structural response.

The numerical tests of the mapping schemes reveal structural response overestimation by the average approach where the error becomes larger as the coupled mesh non-matching increases, especially when the fluid element is larger than the structural element. This indicates that the average mapping approach is not suitable for high-order CASE elements which often have larger element size than the structural elements.

We also found that the energy conservative method is not necessary for this type of problem because the consistent approach can sufficiently ensure energy conservation and generate almost the same result with easier implementation and less computational effort.

Because the floating shock platform problem may not represent the full properties of a full ship our future research and next paper will apply this method to a medium surface combatant ship.

Reference

[1] A. H. Keil, "The Response of Ships To Underwater Explosions," in *Transactions of Society of Naval Architects and Marine Engineers*, 1961.

[2] W. D. Reid, *The Response of Surface Ships to Underwater Explosions*. Melbourne, Vic. : DSTO Aeronautical and Maritime Research Laboratory, 1996.

[3] K. Makinen, "Cavitation Models for Structures Excited By a Plane Shock Wave," *J. Fluids Struct.*, vol. 12, pp. 85–101, 1998.

[4] G. I. Taylor, "The Pressure and Impulse of Submarine Explosion Waves on Plates," *Sci. Pap. Sir Geoffrey Ingram Taylor*, pp. 287–303, 1941.

[5] A. K. Mathew, "Modeling Underwater Explosion (UNDEX) Shock Effects for Vulnerability Assessment in Early Stage Ship Design," Virginia Tech, 2018.

[6] T. L. Geers, "Doubly asymptotic approximations for vibration analysis of submerged structures," *J. Acoust. Soc. Am.*, vol. 73, no. 4, p. 1152, 1978.

[7] T. L. Geers, "Residual Potential and Approximate Methods for Three-Dimensional Fluid-Structure interaction problems," *J. Acoust. Soc. Am.*, vol. 49, no. 5, pp. 1505–1510, 1970.

[8] T. L. Geers and B. J. Toothaker, "Third-order Doubly Asymptotic Approximations for Computational Acoustics," *J. Comput. Acoust.*, vol. 08, no. 01, pp. 101–120, 2000.

[9] J. A. DeRuntz, T. L. Geers, and C. A. Felippa, "The Underwater Shock Analysis (USA) Code, a Reference Manual," 1978.

[10] P. K. Fox, "Nonlinear Response of Cylindrical Shells to Underwater Explosion: Testings and Numerical Prediction Using USA/DYNA3D," 1992.

[11] S. L. Wood and Y. S. Shin, "Cavitation Effects on a Ship-Like Box Structure Subjected to an Underwater Explosion," Naval Postgraduate School, 1998.

[12] F. L. DiMaggio, I. S. Sandler, and D. Rubin, "Uncoupling Approximations in Fluid-Structure Interaction Problems With Cavitation," *J. Appl. Mech.*, vol. 48, no. December 1981, pp. 753–756, 1981.

[13] M. A. Sprague and T. L. Geers, "Computational Treatments of Cavitation Effects in Near-Free-Surface Underwater Shock Analysis," *Shock Vib.*, vol. 7, pp. 105–122, 2001.

[14] R. Newton, "Effects of Cavitation on Underwater Shock Loading-Plane Problem Part 1," 1979.

[15] O. C. Zienkiewicz, D. K. Paul, and E. Hinton, "Cavitation in Fluid-Structure Response (With Particular Reference to Dams Under Earthquake Loading)," *Earthq. Eng. Struct. Dyn.*, vol. 11, no. April 1982, pp. 463–481, 1983.

[16] C. A. Felippa and J. A. DeRuntz, "Finite Element Analysis of Shock-induced Hull Cavitation," *Comput. Methods Appl. Mech. Eng.*, vol. 44, no. 3, pp. 297–337, 1984.

[17] Y. S. Shin, "Ship Shock Modeling and Simulation for Far-Field Underwater Explosion," *Comput. Struct.*, vol. 82, no. 23–26, pp. 2211–2219, 2004.

[18] S. W. Gong and K. Y. Lam, "On Attenuation of Floating Structure Response to Underwater Shock," *Int. J. Impact Eng.*, vol. 32, no. 3, 2006.

[19] D. B. Woyak, "Modeling Submerged Structures Loaded by Underwater Explosions with ABAQUS / Explicit," *ABAQUS Users' Conf.*, pp. 1–15, 2002.

[20] X. Li, X. Wei, P. Zheng, and W. Wu, "The Response of a Floating Structure Due to Underwater Explosion with Cavitation Effect," in *International Society of Offshore and Polar Engineers*, 2010, vol. 7, pp. 633–638.

[21] A. Zhang, W. Zhou, S. Wang, and L. Feng, "Dynamic Response of the Non-Contact

Underwater Explosions on Naval Equipment," *Mar. Struct.*, vol. 24, no. 4, pp. 396–411, 2011.
[22] Z. Zong, Y. Zhao, and H. Li, "A Numerical Study of Whole Ship Structural Damage Resulting from Close-In Underwater Explosion Shock," *Mar. Struct.*, vol. 31, pp. 24–43, 2013.
[23] G. Wang, S. Zhang, M. Yu, H. Li, and Y. Kong, "Investigation of the Shock Wave Propagation Characteristics and Cavitation Effects of Underwater Explosion near Boundaries," *Appl. Ocean Res.*, vol. 46, pp. 40–53, 2014.
[24] Dassault Systèmes Simulia, "Abaqus 6.14 Theory Guide," 2014.
[25] J. D. De Basabe and M. K. Sen, "Grid Dispersion and Stability Criteria of Some Common Finite-Element Methods for Acoustic and Elastic Wave Equations," *Geophysics*, vol. 72, no. 6, pp. T81–T95, 2007.
[26] M. A. Sprague and T. L. Geers, "Spectral Elements and Field Separation for an Acoustic Fluid Subject to Cavitation," *J. Comput. Phys.*, vol. 184, no. 1, pp. 149–162, 2003.
[27] M. A. Sprague and T. L. Geers, "A Spectral-Element Method for Modelling Cavitation in Transient Fluid-Structure Interaction," *Int. J. Numer. Methods Eng.*, vol. 60, no. 15, pp. 2467–2499, 2004.
[28] M. A. Sprague and T. L. Geers, "A Spectral-Element/Finite-Element Analysis of a Ship-Like Structure Subjected to an Underwater Explosion," *Comput. Methods Appl. Mech. Eng.*, vol. 195, no. 17–18, pp. 2149–2167, 2006.
[29] M. A. Sprague, "Advanced Computational Techniques for the Analysis of 3-D Fluid-Structure Interaction with Cavitation," University of Colorado at Boulder, 2002.
[30] A. T. Patera, "A Spectral Element Method for Fluid Dynamics: Laminar Flow in a Channel Expansion," *J. Comput. Phys.*, vol. 54, no. 3, pp. 468–488, 1984.
[31] B. Klenow, "Finite and Spectral Element Methods for Modeling Far-Field Underwater Explosion Effects on Ships," Virginia Tech, 2009.
[32] A. Zhang, S. Ren, Q. Li, and J. Li, "3D Numerical Simulation on Fluid-Structure Interaction of Structure Subjected to Underwater Explosion with Cavitation," *Appl. Math. Mech. (English Ed.*, vol. 33, no. 9, pp. 1191–1206, 2012.
[33] Y. S. Shin and N. A. Schneider, "Ship Shock Trial Simulation of USS Winston S. Churchill (DDG 81): Modeling and Simulation Strategy and Surrounding Fluid Volume Effects," in *74 th Shock and Vibration Symposium*, 2003.
[34] C. A. Felippa, K. C. Park, and M. R. Ross, "A Classification of Interface Treatments for FSI," in *Fluid Structure Interaction II: Modelling, Simulation, Optimization*, H.-J. Bungartz, M. Mehl, and M. Schäfer, Eds. Berlin, Heidelberg: Springer Berlin Heidelberg, 2010, pp. 27–51.
[35] C. Bernardi, Y. Maday, and A. T. Patera, "Domain Decomposition by the Mortar Element Method," in *Asymptotic and Numerical Methods for Partial Differential Equations with Critical Parameters*, H. G. Kaper, M. Garbey, and G. W. Pieper, Eds. Dordrecht: Springer Netherlands, 1993, pp. 269–286.
[36] M. R. Ross, C. A. Felippa, K. C. Park, and M. A. Sprague, "Treatment of Acoustic Fluid-Structure Interaction by Localized Lagrange Multipliers: Formulation," *Comput. Methods Appl. Mech. Eng.*, vol. 197, no. 33–40, pp. 3057–3079, 2008.
[37] C. Farhat, M. Lesoinne, and N. Maman, "Mixed Explicit/Implicit Time Integration of Coupled Aeroelastic Problems: Three-Field Formulation, Geometric Conservation and Distributed Solution," *Int. J. Numer. Methods Fluids*, vol. 21, no. 10, pp. 807–835, 1995.

[38] C. Farhat, M. Lesoinne, and P. Le Tallec, “Load and Motion Transfer Algorithms for Fluid/structure Interaction Problems with Non-matching Discrete Interfaces: Momentum and Energy Conservation, Optimal Discretization and Application to Aeroelasticity,” *Comput. Methods Appl. Mech. Eng.*, vol. 157, no. 1–2, pp. 95–114, 1998.
[39] R. Lohner *et al.*, “Fluid-structure-thermal Interaction Using a Loose Coupling Algorithm and Adaptive Unstructured Grids,” *Am. Inst. Aeronaut. Astronaut.*, 1998.
[40] R. K. Jaiman, X. Jiao, P. H. Geubelle, and E. Loth, “Assessment of Conservative Load Transfer for Fluid–Solid Interface with Non-Matching Meshes,” *Int. J. Numer. Methods Eng.*, vol. 218, no. 1, pp. 372–397, 2005.
[41] M. R. Ross, M. A. Sprague, C. A. Felippa, and K. C. Park, “Treatment of Acoustic Fluid-Structure Interaction by Localized Lagrange Multipliers and Comparison to Alternative Interface-Coupling Methods,” *Comput. Methods Appl. Mech. Eng.*, vol. 198, no. 9–12, pp. 986–1005, 2009.
[42] Computing Fraunhofer Institute for Algorithms and Scientific, *MpCCI 4.5 user manual*. Sankt Augustin, Germany, 2017.
[43] H. Bleich and I. Sandler, “Interaction Between Structures and Bilinear Fluids,” *Int. J. Solids Struct.*, vol. 6, no. 5, pp. 617–639, 1970.
[44] “MIL-S-901D Military Specification,” 1989.
[45] R. H. Cole, *Underwater Explosions*. Princeton University Press, 1948.
[46] M. Swisdak, “Explosion Effects and Properties: Part II – Explosion Effects in Water,” Washington, DC, 1978.
[47] D. M. Russell, “Error Measures for Comparing Transient Data: Part I: Development of a Comprehensive Error Measure Part II: Error Measures Case Study,” in *The Proceedings of the 68th Shock and Vibration Symposium*, 1997, pp. 3–6.
[48] T. Irvine, “An Introduction to the Shock Response Spectrum,” Vibrationdata, 2012.
[49] E. W. Clements, “Shipboard Shock and Navy Devices for Its Simulation,” Washington, DC, 1972.
[50] A. De Boer, A. H. van Zuijlen, and H. Bijl, “Comparison of Conservative and Consistent Approaches for the Coupling of Non-Matching Meshes,” *Comput. Methods Appl. Mech. Eng.*, vol. 197, no. 49–50, pp. 4284–4297, 2008.

Chapter 3 Assessment of a New Mesh Generation and Modeling Approach for the Surface Ship Far-field Underwater Explosion Problem

(Presented at SNAME Maritime Convention 2019 and submitted to SNAME annual transaction)

Zhaokuan Lu, Alan Brown
Department of Aerospace and Ocean Engineering, Virginia Tech, Blacksburg, VA, 24061, USA

Abstract

Critical components in the study and improvement of ship survivability include the vulnerability of a ship to the impact of an underwater explosion (UNDEX) and how to incorporate this factor into early-stage ship design. When simulating surface ship early-time far-field UNDEX, the Finite Element Method (FEM) may be used to model shock wave propagation and cavitation in the fluid. This is a computationally intensive task, however, due to the large size of the fluid domain which typically requires several million degrees of freedom (DOF) in the mesh. The task is further complicated by the need to generate the fluid mesh around the irregular ship hull geometry. Ship design concept exploration requires fast simulation with minimal or no manual intervention in the mesh generation. The high-order Spectral Element Method (SEM) has proven to be a more accurate replacement for linear FEM in UNDEX modeling but is restricted to using hexahedral elements in 3D. Therefore, the fast, automated application of the SEM in the surface ship UNDEX problem is hindered by the need to generate an effective and efficient unstructured hexahedral mesh. The research described in this paper assesses a mesh-first, automatic, all-hexahedral mesh generation scheme that provides excellent early-time UNDEX simulation results with only minimal compromise in the boundary geometry accuracy. The resulting fluid mesh is used with linear and high-order SEM elements and results are compared to an all-tetrahedral mesh generated by an automatic Delaunay refinement algorithm with linear FEM elements. The comparison is performed for both Total Field and Scattered Field Finite and Spectral Element Cavitating Acoustic fluid models. The goal of this study is to provide a method of modeling the fluid domain in early-time far-field UNDEX with sufficient efficiency and minimal mesh generation effort.

Keywords: Mesh generation, Underwater explosion, Spectral Element Method, Shock wave

3.1 Introduction

Underwater explosions (UNDEX) have long been a major threat to surface ships, but shock trials are rarely performed before a ship is put into service, long after important decisions affecting the ship and onboard equipment response to underwater shock are made. The shock trial process is long, expensive and environmentally unfriendly. Thus, early assessment has been mostly dedicated to computational prediction. UNDEX events can be categorized as near-field, and far-field. In near-field explosions, the explosive is sufficiently close to the ship's hull and sufficiently large that its effects result in large plastic deformation [1], [2]. Since the energy is mostly absorbed in the ship's hull by the deformation, the destructive effect is typically local and severe. In this work, we focus on the early-time far-field UNDEX where the explosive is relatively small and far from the ship's hull, and the shock wave released by the explosive has

decayed to a linear acoustic wave with a discontinuous pressure profile as it reaches the ship [2]. The structural deformation is mostly or entirely elastic and the high-frequency and low-inertia response of the hull panel is excited with the propagation of the stress wave into the structure. At the point where the hull panels move inward faster than the surrounding water, the water is subject to tension. A cavitation region called local cavitation is developed near the panel due to the inability of water to sustain tension. Quickly, the local cavitation begins to shrink and eventually collapses as the pressure near the panel is restored and the panel rebounds. The collapse creates an impact pressure pulse and panel reloading [3]. At about the same time, the incident shock wave reaches the free surface and the reflection of the shock wave generates a tensile wave. Due to the large impedance difference between water and air, the reflected wave pressure is almost the negative of the incident shock wave. A large cavitation region is formed when the total fluid pressure drops below vapor pressure and remains cavitated until the pressure is restored. This cavitation region is called bulk cavitation. The closure of bulk cavitation also emits a shock wave, the timing, and impact of which depends on the ship's proximity to the closure point [2]. The combination of incident shock wave loading and subsequent response to cavitation constitutes the early-time response of a surface ship to the far-field UNDEX.

As demonstrated by several researchers (e.g., [4]), explicitly modeling the fluid domain around the ship to capture the shock wave propagation and cavitation is essential to solving far-field UNDEX problems. However, the fluid mesh generation takes a significant amount of effort due to the complicated geometry of the hull surface. The USA code [5] methodology is a widely-used approach in simulating the far-field UNDEX problem. The USA framework assumes a matching fluid and structural mesh on the coupling surface where the fluid mesh is extruded from the structural wetted surface mesh [6]. Several layers of mesh are built to extend the fluid mesh to the boundaries, which takes significant manual effort. This is unacceptable in the concept exploration design stage where many different hullform variants need to be considered with their associated meshes. It is desirable to make mesh generation fully automatic. The node-to-node coupling requirement may later be relieved by various non-matching mapping approaches so that the fluid and structural mesh can be generated separately. In prior research dealing with surface ships, hexahedral-dominant [7] and all-tetrahedral meshes [8] are most commonly used. The creation of hex-dominant meshes usually involves a degree of manual intervention to make the domain meshable. Although an automatic generation algorithm for hex-dominant meshes is introduced by Baudouin [9], the hex-mesh percentage is not guaranteed and non-conformal faces exist. Automatic schemes to generate a tetrahedral mesh are quite mature (ex: Advancing front, Delaunay refinement), however, the tetrahedron is generally considered inferior to the hexahedron in terms of accuracy and computational efficiency since more elements must be used for the same DOF. Furthermore, the elements around sharp edges tend to have poor element quality (large skewness) and very small size, which limits the numerical time step size if an explicit solver is used. The small time step size significantly increases the computational time for the surface ship UNDEX problem since the DOFs are large in the large fluid domain. As a result, an automatically generated all-hexahedral mesh with satisfactory quality is a better solution for this type of problem. Another benefit of using an all-hexahedral mesh is the potential to harness the benefit of the Spectral Element Method (SEM). Introduced by Patera [10], SEM is a combination of the Spectral Method and traditional FEM. High-order basis functions with interpolation nodes at the root of orthogonal polynomials are used to reduce the interpolation error which makes SEM less dispersive than linear FEM element. The superior behavior of high-order Spectral Element Method (SEM) over traditional FEM in UNDEX

problems has been demonstrated in several studies [11]–[13]. However, extension to the surface ship problem has been limited by the restriction of SEM to using hexahedral elements and the lack of efficient all-hexahedral mesh generators. Although the nodal SEM has been extended to the triangular element with higher numerical cost (e.g., [14]), extension to tetrahedral elements is still ongoing research.

Most hexahedral mesh generation methods can be categorized as either geometry-first or mesh-first schemes. The geometry-first approach captures the geometry boundary in CAD form by carefully arranging the elements around it. This usually involves algorithms such as mapping and sweeping. The geometry-first approach can usually generate a high-quality mesh around the geometry boundary, however, the process has yet to be automated for a general geometry since the domain has to first be partitioned into mappable or sweepable parts. Instead of attempting to reconstruct the geometry as fine as possible, the mesh-first algorithm meshes the domain as if there is no boundary and then deforms the nodes near the boundary to capture the geometry. This allows fast and automatic all-hex meshing but with the sacrifice of boundary geometry accuracy.

In this work, we employ the Sculpt algorithm introduced by Owen [15] which is implemented in the software BOLT [16]. The Sculpt scheme starts with a box bounding the geometry to be meshed. Then, a uniformly-sized Cartesian grid comprised of hexahedrons is built. Next, the nodes are projected on to the geometry boundary. A pillow layer comprised of hex elements is then inserted at the boundary to locally refine the mesh. Smoothing techniques are employed to improve the mesh quality in the last step. The advantage of the Sculpt mesh generation scheme is that little manual intervention is required and the interior mesh quality is high due to the base Cartesian mesh throughout the domain. Another benefit of the Sculpt algorithm and most mesh-first methods is that they are less geometry-sensitive since the boundary is not explicitly fitted as in the geometry-first approaches. During the model preparation stage, unseen gaps and misalignments in the model may be induced. Tackling these geometric imperfections usually takes a large amount of time before the meshing process can start. Furthermore, the nature of the method allows the parallel execution of the meshing [17]. A drawback of this meshing approach is that the quality of the boundary mesh depends on the resolution of the base mesh and edges are rounded if the base mesh is not fine enough. As the mesh is refined, the sharpness is gradually retrieved. For ship hull geometry, sharp geometry changes usually present near bow and stern which are not as critical for the UNDEX problem. The mesh generated by Sculpt was validated against a more sophisticated mesh by the manual pave-and-sweep technique in [18]. The result showed an equivalently accurate result for the Sculpt-generated mesh.

In summary, there are several benefits of applying the Sculpt all-hexahedral meshing algorithm to the UNDEX problem. The first is significant time savings in the design process since little manual intervention is required for model preparation and mesh generation. Secondly, the problem of poor element quality (e.g., highly distorted and small element) around sharp boundaries can be avoided with a little sacrifice of geometry representation accuracy. Thus, a relatively large time step size can be used and the simulation may be more stable due to high element quality. Finally, the all-hexahedral mesh enables the application of the Spectral Element Method. All of these benefits improve efficiency which is imperative in the early ship design process where thousands of designs may need to be considered.

For the remainder of this work, we will assess the unstructured all-hexahedral mesh generated by the Sculpt algorithm for application to the far-field UNDEX problem. The mesh is

used to discretize the fluid domain for an in-house Cavitating Acoustic Finite/Spectral Element (CAFE/CASE) fluid code developed based on the methodology proposed by Sprague [19]. At this point, the Sculpt algorithm is not able to generate a curvilinear high-order hexahedral element. The high-order SEM element is thus generated by inserting internal nodes in the linear element. Therefore, the base element size of high-order SEM mesh is larger than the linear SEM mesh with comparable DOF, making the boundary geometry less accurate. This could potentially compromise the computational advantage of the high-order SEM mesh. Although the tetrahedral element is typically considered inferior to the hexahedral element, its automatic mesh generation property is highly desirable. We will compare the computational efficiency of an all-hexahedral mesh generated by the Sculpt algorithm using linear and high-order SEM elements to the all-tetrahedral mesh generated by the Delaunay refinement algorithm using linear FEM elements.

In the following sections, we first present the fluid-structure interaction framework coupling our in-house fluid solver with the Abaqus structural solver for the numerical simulation. Then, the model and the FSI framework are assessed using two benchmark problems. Next, the tetrahedral linear FEM element, hexahedral linear element and high-order SEM element are compared in an acoustic wave propagation case. Finally, the computational efficiency of the three fluid mesh types is assessed in a surface ship UNDEX problem.

3.2 Numerical Model

In this section, we briefly present the fluid and structural model and the FSI framework used for later assessment.

3.2.1 Abaqus (Explicit) Structural Solver

Since an important effect of the far-field UNDEX problem is the structural oscillation caused by the stress wave propagation after the shock impact, Abaqus Explicit is chosen to model the structure due to its advantage in solving problems with transient high-speed events. In comparison, the implicit solver (Abaqus Standard) is more suitable for the low-speed phenomenon like structure dynamic motion after the shock wave effect is gone. The semi-discretized structural motion is expressed in Eq. 3.1.

$$M\ddot{x} + Kx = f \tag{3.1}$$

The mass matrix is lumped to save memory and facilitate the explicit central difference Newmark scheme [20].

3.2.2 Cavitating Acoustic Finite/Spectral Element Method (CAFE/CASE)

In this section, the governing equations and spatial discretization of the CAFE/CASE model, adapted from [12], [19], [21] are described.

3.2.2.1 Governing equations

The far-field assumption allows the acoustic treatment of the shock wave propagation. Although the acoustic fluid is compressible, we assume the fluctuations of density are small, thus allowing the continuity equation based on dynamic displacement $\vec{x}$:

$$\frac{\partial \rho}{\partial t} + \nabla \cdot \left(\rho \frac{\partial \vec{x}}{\partial t} \right) = 0 \tag{3.2}$$

to be linearized using total condensation $S = \frac{\rho}{\rho_0} - 1$ for $|S| \ll 1$:

$$\frac{\partial S}{\partial t} + \nabla \cdot \left(\frac{\partial \vec{x}}{\partial t}\right) = 0 \tag{3.3}$$

Neglecting the viscosity and convection term, the Euler momentum equation for the acoustic fluid is written as:

$$\rho_0 \frac{\partial^2 \vec{x}}{\partial t^2} = \rho_0 \vec{f} - \nabla p^t \tag{3.4}$$

where p^t is the total fluid pressure, and $f(\vec{X})$ is the body force field.

Depending on how the governing equations are implemented in the fluid field, the model can be categorized as a Total Field Model or a Scattered Field Model as described in the following sections.

3.2.2.2 Total Field Model

The Total Field Model (TFM) includes the incident shock wave, scattered and static fluid fields as proposed by [21]. The incident shock wave and its reflection from the boundaries (i.e., structure and free surface) generate the scattered field. The static field is the hydrostatic field of the fluid. Figure 3.1 illustrates a surface ship exposed to an underwater explosion. The incident wave in the ship problem is a spherical shock wave as specified in Eq. 3.7. To minimize computational time and numerical losses, the incident wave is modeled at t=0 as just having reached its first boundary, hull or free surface, although it actually originates at the charge center. The peak pressure P_{peak} and decay rate τ of the incident wave at this time are calculated using the similitude equation from [22] and [23]. The incident wave is tracked in the fluid model from this point on. As the incident wave contacts the free surface or ship's hull, it is reflected (scattered) and absorbed. The TFM tracks the incident wave and calculates it's scattering explicitly in the fluid model with boundary conditions whereas the SFM assumes that the incident wave is known for all time throughout the fluid domain (as though the ship were not there) using the same similitude equation, and only solves for the scattered wave field excited by the interaction between the known incident wave and the domain boundaries.

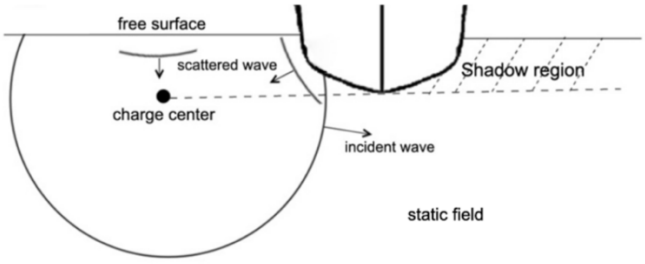

Figure 3.1 Far-field UNDEX wave field demonstration

Using the irrotational fluid assumption $-\nabla\Psi = \vec{x}$, the governing equations, Eq. 3.3 and Eq. 3.4, are converted to the form in Eq. 3.5 and Eq. 3.6. The primary variables only contain the incident and the scattered field, which in combination is called the dynamic field. The detailed derivation is found in [12].

$$s = \nabla^2 \psi \tag{3.5}$$

$$\frac{\partial^2 \psi}{\partial t^2} = \begin{cases} c^2 s, & s > \dfrac{(p^{cav} - p_{eq})}{c^2} \\ p^{cav} - p_{eq}, & Otherwise \end{cases} \tag{3.6}$$

where s is the densified dynamic condensation defined as $s = \rho_0 S$ and ψ is the densified dynamic displacement potential expressed as $\psi = \rho_0 \Psi$. p_{cav} is the vapor pressure of the fluid which is small enough to be negligible. p_{eq} is the static field pressure. The spherical incident pressure p_{inc}, Eq. 3.7, is used to prescribe the initial condition of ψ using the relationship $\psi_0 = \iint p_{inc} dt$. The incident wave at $t = 0$ is prescribed at the point where the wave first touches the fluid boundary (structure or free surface).

$$p_{inc}(\boldsymbol{X}, t) = \frac{R(\boldsymbol{X})}{R_0} P_{peak}\, exp\left[-\frac{t - \frac{R(\boldsymbol{X}) - R_0}{c}}{\tau}\right] H\left[t - \frac{R(\boldsymbol{X}) - R_0}{c}\right] \tag{3.7}$$

where $R(\boldsymbol{X})$ is the distance from the charge center to the fluid node at coordinate $\boldsymbol{X}$. R_0 denotes the initial wave radius at the nearest structure or free surface point.

Following the standard Galerkin approach, Eq. 3.5 is multiplied by the test function ϕ and integrated over the fluid domain Ω_f:

$$\int_{\Omega_f} [s\phi - \nabla^2 \psi \phi] d\Omega = 0 \tag{3.8}$$

Applying the Green's first identity to Eq. 3.8 yields the weak form:

$$\int_{\Omega_f} s\phi d\Omega + \int_{\Omega_f} \nabla\psi \cdot \nabla\phi d\Omega = \int_{\Gamma_f} \phi \nabla\psi \cdot \vec{n} d\Gamma \tag{3.9}$$

where Γ_f denotes the fluid boundary and $\vec{n}$ is the outward pointing normal vector on the boundary.

For the linear and high-order hexahedral spectral elements, the densified condensation and displacement potential are written as:

$$s(\xi, \eta, \zeta, t) = \phi^T s(t) = \sum_{i,j,k=1}^{N+1} \phi_i(\xi)\phi_j(\eta)\phi_k(\zeta) s_{ijk}(t) \tag{3.10}$$

$$\psi(\xi, \eta, \zeta, t) = \phi^T \psi(t) = \sum_{i,j,k=1}^{N+1} \phi_i(\xi)\phi_j(\eta)\phi_k(\zeta) \psi_{ijk}(t) \tag{3.11}$$

where ϕ is the column vector of the 1D spectral basis function $\phi_i(\xi), \phi_j(\eta), \phi_k(\zeta)$. The interpolation point and quadrature point are both chosen as Gauss-Lobatto-Legendre (GLL), thus allowing the mass matrix to be fully diagonal.

For the linear tetrahedral finite element, the corresponding variables are expressed as:

$$s(\xi, \eta, \zeta, t) = \phi^T s(t) = \sum_{i=1}^{4} \phi_i(\xi, \eta, \zeta) s_i(t) \tag{3.12}$$

$$\psi(\xi, \eta, \zeta, t) = \phi^T \psi(t) = \sum_{i=1}^{4} \phi_i(\xi, \eta, \zeta)\, \psi_i(t) \tag{3.13}$$

where ϕ_i is the basis function defined on interpolation nodes as:

$$\phi_1(\xi, \eta, \zeta) = \omega, \phi_2(\xi, \eta, \zeta) = \xi, \phi_3(\xi, \eta, \zeta) = \eta, \phi_4(\xi, \eta, \zeta) = 1 - \omega - \xi - \eta \tag{3.14}$$

Unlike the spectral element, the finite element does not guarantee the mass matrix to be diagonal. Thus, the mass matrix is lumped by the row-sum technique.

Substituting Eq. 3.10 and Eq. 3.11 into the weak form (Eq. 3.9) gives:

$$Qs + H\psi = b \tag{3.15}$$

where $Q = \int_{\Omega_f} \phi\phi^T d\Omega$, $H = \int_{\Omega_f} \nabla\phi \cdot \nabla\phi^T d\Omega$, $b = \int_{\Gamma_f} \phi\nabla\psi \cdot \vec{n} d\Gamma$. Following the nomenclature in [21], we name Q the global capacitance matrix, H the global reactance matrix and b the global fluid force vector. The governing equation (Eq. 3.6) is then evaluated in a node-by-node fashion:

$$\ddot{\psi}_i = \begin{cases} c^2 s_i, & s_i > -p_{eq_i}/c^2 \\ p^{cav} - p_{eq}, & otherwise \end{cases} \quad i = 1,2,\dots n_{node} \tag{3.16}$$

3.2.2.3 Scattered Field Model

The Scattered Field Model (SFM) described in this section was proposed by Sprague and Geers [19] to improve the Total Field Model (TFM). Since the incident field is essentially a shock wave with an exponential decay profile and with a peak pressure P_{peak} and decay rate τ that can be calculated as in Eq. 3.7, it is assumed to be known for all time throughout the fluid domain as though the ship were not there. The SFM only solves for the scattered wave field excited by the interaction between the known incident wave and the domain boundaries. The benefit of the Scattered Field Model (SFM) is that the incident wave can be propagated efficiently without numerical error, unlike in the TFM. Following the same derivation for TFM, the governing equation is reorganized as:

$$s_{sc} = \nabla^2 \psi_{sc} \tag{3.17}$$

$$\frac{\partial^2 \psi_{sc}}{\partial t^2} = \begin{cases} c^2 s_{sc}, & s_{sc} > \dfrac{[p^{cav} - (p_{eq} + p_{inc})]}{c^2} \\ p^{cav} - (p_{eq} + p_{inc}), & Otherwise \end{cases} \tag{3.18}$$

where s_{sc} and ψ_{sc} represent the scattered densified dynamic condensation and densified scattered dynamic displacement potential. p_{inc} is the incident pressure profile introduced in Eq. 3.7.

As in the TFM, the continuity equation is discretized as:

$$Qs_{sc} + H\psi_{sc} = b \tag{3.19}$$

where $Q = \int_{\Omega_f} \phi\phi^T d\Omega$, $H = \int_{\Omega_f} \nabla\phi \cdot \nabla\phi^T d\Omega$, $b = \int_{\Gamma_f} \phi\nabla\psi_{sc} \cdot \vec{n} d\Gamma$.

The governing equation (Eq. 3.18) is evaluated in a node-by-node fashion:

$$\ddot{\psi}_{sc_i} = \begin{cases} c^2 s_{sc_i}, & s_{sc_i} > \dfrac{[p^{cav} - (p_{eq_i} + p_{inc_i})]}{c^2} \\ p^{cav} - (p_{eq_i} + p_{inc_i}), & otherwise \end{cases} \quad i = 1,2,\dots n_{node} \tag{3.20}$$

where p_{inc_i} is the known incident pressure at node i.

Although the advantage of SFM was demonstrated by Sprague and Geers [19] in an underwater spherical shell case, it may not be sufficient for the surface ship problem. Since the incident wave is prescribed using (Eq. 3.7) in the SFM, the structure is treated as though it is not present. Therefore, the fluid domain region potentially affected by the hull (see the shadow region in Figure 3.1) is not considered by the SFM. As a result, the structural response on the shadow side may be over-predicted using SFM. In Section 3.3.4 this problem is evaluated and a refined SFM model is proposed. The underwater spherical shell modeled in [19] does not suffer significantly from this problem because the structure is small enough and shaped to allow the wave to diffract to its shadow side.

3.2.2.4 Temporal discretization

The governing equations of the CAFE/CASE model are integrated in time using a staggered second-order explicit central difference scheme (a.k.a. Leapfrog scheme) introduced in [21].

3.2.3 Non-matching Fluid and Structural Mesh Coupling

In this section, we introduce the fluid-structure mesh coupling approach. Since the FSI boundary geometry is complicated, the fluid and structure interface meshes usually are non-matching. Thus, the displacement and nodal force needs to be interpolated before it can be used by the partner solver. A consistent interpolation approach proposed by Farhat [24] which guarantees the mapping consistency of the pressure and the displacement fields is applied.

The consistent mapping scheme follows a straightforward implementation by projecting the target nodes to the source mesh and then interpolating the desired properties using the local shape function. Specifically, the structural quadrature nodes χ_i (i.e., Gauss-Legendre) are orthogonally projected to the closest fluid mesh to obtain the interpolated pressure (Eq. 3.21) and the displacement is obtained by projecting the fluid nodes on the structure mesh and interpolating using the local structural shape function (Eq. 3.22).

$$p_{\chi_i} = \sum_{j=1}^{j=n_f} N_j(\chi_i) p_j \tag{3.21}$$

$$u_j = \sum_{i=1}^{i=n_s} N_i(\chi_j) u_i \tag{3.22}$$

where i denotes the nodes on structure element and j on fluid element, p is the pressure and u is the nodal displacement, n_s and n_f are the node number on the structure and fluid element and N is the shape function. In Figure 3.2, we use a 3rd order CASE element coupled to the linear structural element as an illustration of this method.

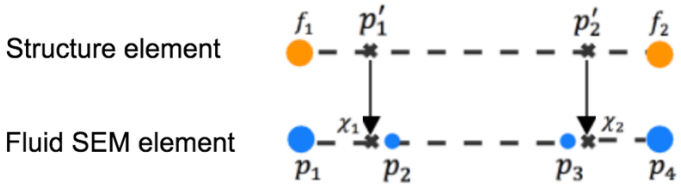

Figure 3.2 Consistent mapping algorithm

3.3 Numerical Results and Model Assessment

In this section, results from the FSI framework and models described in Section 3.2 are presented and compared to analytical results from simple baseline problems and to each other. In Section 3.3.1, a benchmark underwater spherical shell UNDEX problem that has been solved analytically, and a basic surface ship UNDEX problem that was solved numerically using the Abaqus structural-acoustic solver are used to demonstrate and assess our FSI framework and models. In Section 3.3.2, an acoustic wave pressure propagation problem is presented and results using linear and high-order SEM elements are compared to results using linear tetrahedral FEM elements. The purpose of this comparison is to describe the behavior of the fluid meshes using those element types and make an initial comparison of their results. In Section 3.3.3, structural

velocity response results using an all-hexahedral (hex) fluid mesh generated by the Sculpt algorithm with linear and high-order SEM elements are compared to results using an all-tetrahedral (tet) mesh generated by the Delaunay algorithm with FEM elements. These meshing schemes are both fully automatic, thus candidates for a design application. This comparison is performed using both TFM and SFM. The goal of this comparison is to assess the most efficient design-feasible fluid meshing scheme for the far-field UNDEX problem. Section 3.3.4 extends this study by further investigating differences between the Total Field Model and Scattered Field Model.

3.3.1 Model Assessment

The model and FSI framework introduced in Section 3.2 are assessed using an underwater shell benchmark problem without cavitation and by comparison to Abaqus numerical results in a basic surface ship UNDEX problem. Excellent agreement with the benchmark and baseline results provides more confidence in the model setup employed for the numerical experiment described in later sections.

3.3.1.1 Underwater spherical shell

An empty underwater spherical shell subject to a plane step wave is modeled as in Figure 3.3. This problem was first solved analytically by Zhang and Geers [25] using a modified Cesaro summation method. The shell is considered to be elastic and isotropic. The material density is ρ_0 and the plate velocity is $c_0 = \sqrt{E/\rho_0(1-\nu^2)}$, where E is Young's modulus and ν is the Poisson's ratio. The shell thickness-to-radius ratio is defined as $h/a = 0.01$ where h is the shell thickness and a is the sphere radius, satisfying thin shell theory. For the fluid property, the density ρ is set to $\rho_0/\rho = 7.7$ and the velocity c is $c_0/c = (13.8)^{0.5}$. Cavitation is not considered due to the underwater nature of this problem. The hydrostatic pressure is high enough to prevent the cavitation generation. Thus, the cavitation cut-off condition in Eq. 3.16 is disabled. For the incident wave field, a plane step wave is used instead of the spherical wave defined in Eq. 3.7:

$$p_{inc}(\boldsymbol{X}, t) = P_I H\left(t + \frac{\boldsymbol{X} - x_{so}}{c}\right) \tag{3.23}$$

where P_I is the peak pressure on the shock front, c is the wave speed. $\boldsymbol{X}$ is the location vector of the fluid nodes and x_{so} is the initial location of the shock front at $t = 0$.

The shell velocity response at two points is sampled. The first point is sampled at the front of the shell at $\theta = 0°$ and the second point at $\theta = 180°$. The initializing wavefront is positioned at the first sample point at $t = 0$ and propagates to the back of the shell. The result is non-dimensionalized with length scaled by a, time by a/c and pressure by ρc^2. The velocity is normalized to v/P_I. The numerical solution is obtained by coupling our in-house CASE code with hex linear SEM mesh and the Abaqus structural solver with spherical shell modeled by a linear shell element (S4R). As can been seen from the velocity response at the first sample point (Figure 3.4) and the second sample point (Figure 3.5), the numerical result agrees well with the analytical solution given in [25]. The spurious oscillation observed in the numerical result is caused by interpolating the sharp gradient of the step wave, which is also known as the Gibbs phenomenon.

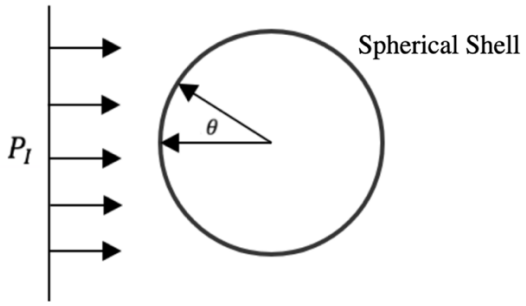

Figure 3.3 Empty 3D spherical shell response to plane shock wave

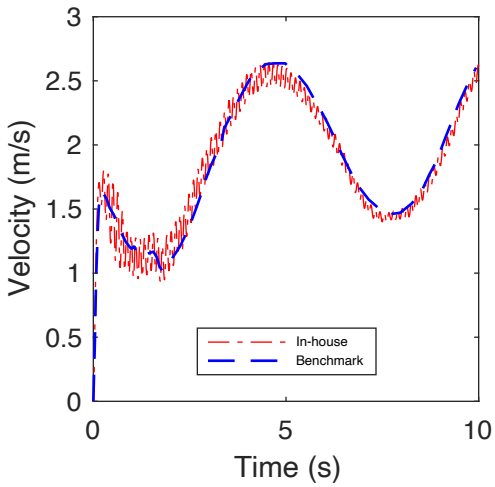

Figure 3.4 Spherical shell structural response at $\theta = 0°$

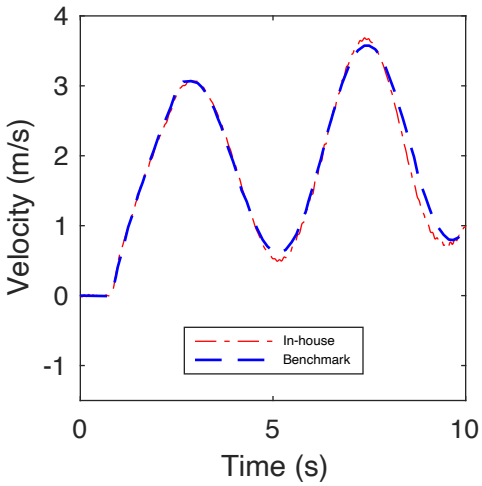

Figure 3.5 Spherical shell structural response at $\theta = 180°$

3.3.1.2 Surface ship

In the surface ship problem, cavitation must be considered including the bulk cavitation induced by free surface wave reflection and local cavitation caused by hull panel bending. In this

section, we simulate the UNDEX event of a surface ship shown in Figure 3.6 under a spherical shock wave impact. The incident shock wave in Eq. 3.7 is applied with the charge center directly below the keel at a depth of 18.288m (60ft).

Since precise experimental data or analytical solution are not available, we assess our result by comparing it to a numerical solution calculated using the Abaqus structural-acoustic solver which couples a linear FEM-based acoustic fluid solver with the Abaqus structural solver described in Section 3.2.1. Although the Abaqus structural-acoustic solver has been used by many researchers and shown to have good performance in UNDEX problems (e.g., [26]), it does not support high-order SEM elements so it is only used for solution comparison in this work. In the Abaqus acoustic solver, we use a CAFE-like approach with the same cut-off cavitation condition and non-reflective boundary condition used in our in-house fluid solver. The major difference from the CAFE method used in our model is that the linear acoustic fluid element (AC3D8R) in Abaqus is pressure-based instead of using displacement potential. The all-hexahedral fluid mesh is generated using the Sculpt algorithm with a mesh size of 0.1524m (0.5ft). The structural mesh is comprised of quad and triangular shell elements with a size around 0.5m. The same ship structure is modeled in our framework and coupled to our CAFE/CASE fluid solver with the mapping approach introduced in Section 3.2.3. The same base fluid mesh is used as in the Abaqus acoustic solver, but with linear CASE elements. Two points are sampled on top of the keel. The first point is close to the point where the wavefront first touches the structure at (70m, -4m, 0m) and the second point is closer to the bow at (85m, -4m, 0m).

The velocity response result of the in-house model and FSI framework agrees well with the Abaqus acoustic-structure solver solution as shown in Figure 3.7 and Figure 3.8 for the first and second sample point. The structural response features an initial kick-off followed by a rebound caused by the local cavitation and structural stiffness. The structure is then reloaded once the local cavitation collapses. The peak velocity at the second sample point is smaller than the first since the pressure magnitude decreases during the spherical wave propagation.

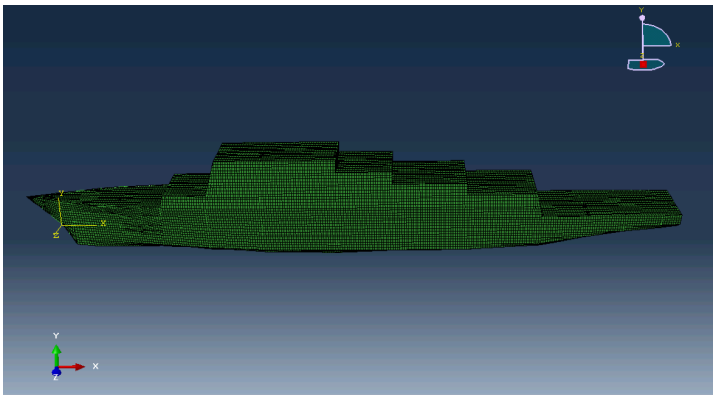

Figure 3.6 Ship structure mesh

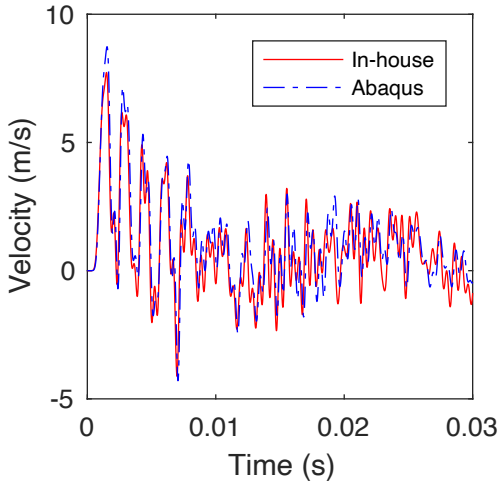

Figure 3.7 Velocity response comparison at the first sample point

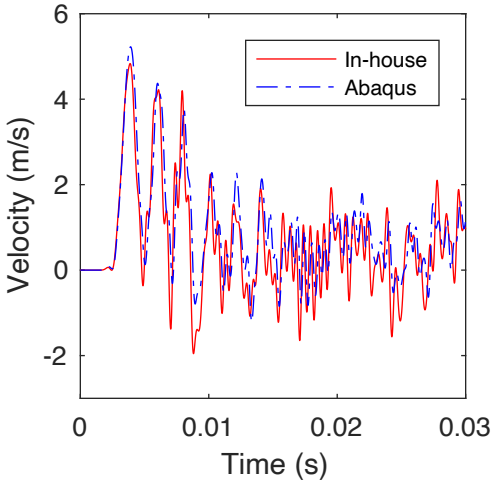

Figure 3.8 Velocity response comparison at the second sample point

3.3.2 Acoustic wave propagation model efficiency comparison

It is assumed that a shock wave decays to a linear acoustic wave traveling from the far-field regime and that the structural response is significantly influenced by its characteristics. Therefore, correctly simulating the acoustic wave propagation pressure is an important factor in modeling far-field UNDEX events. In this section, the computational efficiencies of the hex linear SEM element, high-order SEM element, and tet linear FEM element for propagating a spherical wave in a fluid column are compared. The result helps explain the different mesh and model behavior described later. A series of runs are made with increased mesh refinement and resulting increased DOF. The base fluid element size is 0.3048m (1ft). h refinement (refines the mesh without changing element type) is performed for linear SEM elements and linear tet elements from 2nd to 5th order. p refinement (refines the mesh by increasing element order) is performed for high-order SEM elements from 2nd to 5th order. The CAFE/CASE fluid solver with Total Field Model as described in Section 3.2.2 is used. Only a quarter of the spherical wave is modeled since the wave is axisymmetric. The spherical incident wave in Eq. 3.7 is

prescribed as the initial condition. The charge center is 21.336m (70ft) deep. The incident wavefront is initiated at 3.048m (10ft) deep when $t = 0$ ($R_0 = 60ft$).

The pressure profile is sampled along the spherical wave center line on the fluid column edge after the wave is propagated for 1ms. For clarity, only the 4th degree h or p-refined solution is plotted to show the wave profile (see Figure 3.10). Although the tet linear FEM element is able to capture the peak pressure more precisely, spurious oscillations are stronger than with the hex SEM elements especially near the tail of the wave. This may be caused by discretizing the high-gradient field using the constant-gradient linear basis function (Eq. 3.14) of the tet element. The L2 error norm of the wave pressure profile is plotted against degree of freedom (DOF) in Figure 3.11. The error norm of the hex high-order SEM element decreases faster than the other two element types. The tet linear FEM element has a similar level of accuracy as the hex high-order SEM element with the same DOF. The hex linear SEM element has a higher error norm relative to DOF compared to the other two element types. The good performance of tet linear FEM element may be explained by more element used for the same DOF. As an alternative to DOF to assess computational efficiency, we also use the floating-point operation count (FLOP) of the global reactance term ($H\psi$), which takes both DOF and element number into account. More details about FLOP quantification are found in [27]. The L2 error norm is plotted against the FLOP count in Figure 3.12. These results show higher computational efficiency for both the hex linear and high-order SEM elements than the tet-linear FEM elements. The hex high-order SEM element shows the fastest overall convergence rate with mesh refinement.

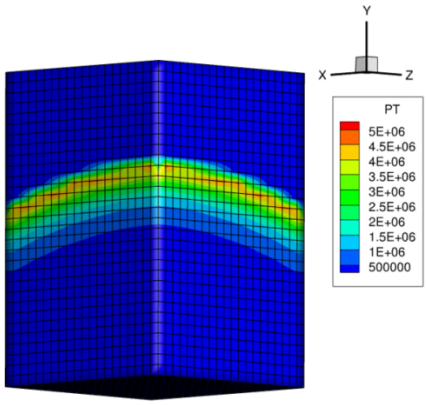

Figure 3.9 Fluid column used for wave propagation

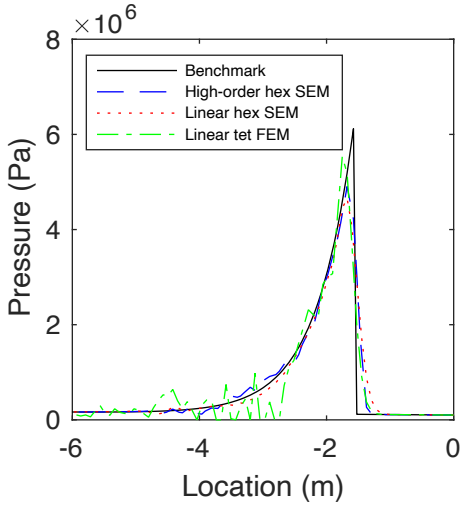

Figure 3.10 Wave pressure profile comparison at 1ms

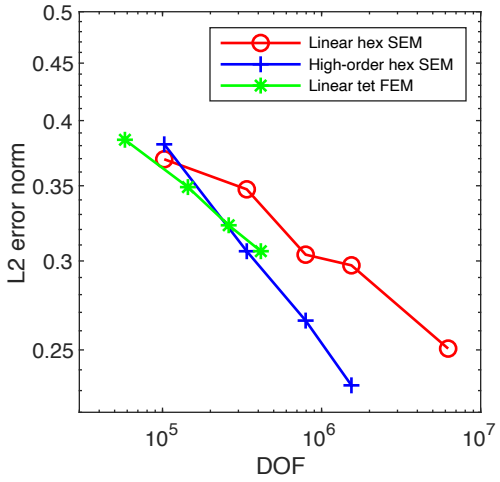

Figure 3.11 Wave pressure profile L2 error norm vs DOF

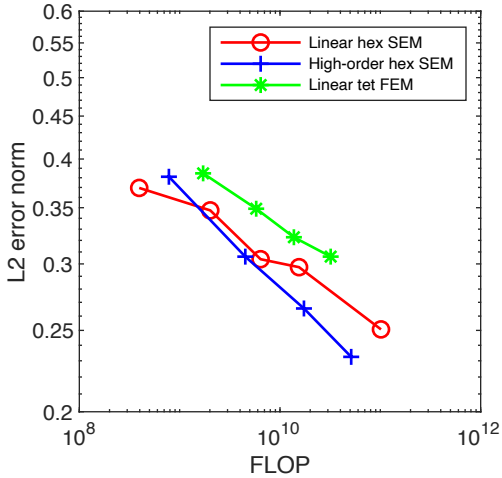

Figure 3.12 Wave pressure profile L2 error norm vs FLOP

3.3.3 Structural response fluid mesh type efficiency comparison

In this section, we compare the computational efficiency based on ship structural response of the all-hex mesh with linear and high-order SEM elements to the all-tet mesh with linear FEM elements. The comparison is conducted using both Total Field Model (TFM) and Scattered Field Model (SFM) variations of the fluid model. The surface ship case validated in Section 3.3.1.2 is used. The case configuration stays the same unless specified otherwise (e.g., sample points). The baseline element size is 0.762m (2.5ft) which is h-refined for hex linear SEM mesh and tet linear FEM mesh (up to 4th level) and p-refined for the hexahedral high-order SEM mesh (up to 3rd order).

Since no experimental data is available, a benchmark solution is generated by the in-house fluid model using a highly-refined structured hex-linear SEM fluid mesh with 0.1524m (0.5ft) element size. This highly-refined fluid mesh for this benchmark only is generated manually using the Abaqus structured mesh algorithm with the fluid domain partitioned into blocks that allow the mesh to be mapped from a regular shaped domain. This mesh is used in our in-house code. The accuracy of the structural velocity response is again compared to the floating-point operation count (FLOP), but instead of using the L2 norm as with the fluid pressure, the structural velocity error is calculated using the approach introduced by Russel (Russell, 1997) which is frequently used to evaluate the accuracy of vibration velocity response. A Russell error norm of 0.1 is typically used as an upper limit for sufficiency and this threshold is indicated on the Russell error norm plots.

In a shock and vibration problem, the shock response spectrum (SRS) is often assessed in addition to the velocity response. The SRS serves the purpose of assessing how the structural and other ship components with certain natural frequency (e.g., onboard equipment) would respond to the vibration. It provides an important input for ship equipment design and installation. For the SRS error quantification in the following two sections, the L2 error norm of the pseudo-velocity is calculated and plotted against FLOP.

3.3.3.1 TFM structural response fluid mesh efficiency comparison

Cases using the three meshes and the Total Field Model are discussed first. The structural velocity Russell error norm and SRS L2 error norm at two sample points as a function of the FLOP count are compared in Figure 3.13 to Figure 3.18. As shown in Figure 3.13 and Figure 3.16, the all-hex high-order SEM mesh has a lower velocity response Russell error norm than the all-hex linear SEM mesh at both sample points. The all-tet linear FEM mesh result shows the lowest accuracy although the error norm is acceptable (<0.1) at the highest refinement level. This result is also consistent with the wave propagation comparison in Section 3.3.2, which indicates that capturing the wave front correctly may be a significant factor in the structural response comparison.

The SRS of the three mesh types are plotted in Figure 3.14 (sample point 1) and Figure 3.17 (sample point 2). Only the results of the highest mesh refinement level are shown for clarity. Figure 3.15 and Figure 3.18, points 1 and 2, show a similar advantage for the all-hex high-order SEM mesh in the SRS L2 error norm. This is particularly evident at point 2 (further) point where the larger numerical dispersion in the wave profile for the all-hex linear SEM mesh and all-tet linear FEM mesh as the wave travels to the second sample point has a greater impact. Overall, the all-hex mesh with high-order SEM element appears to be the best choice when using the TFM.

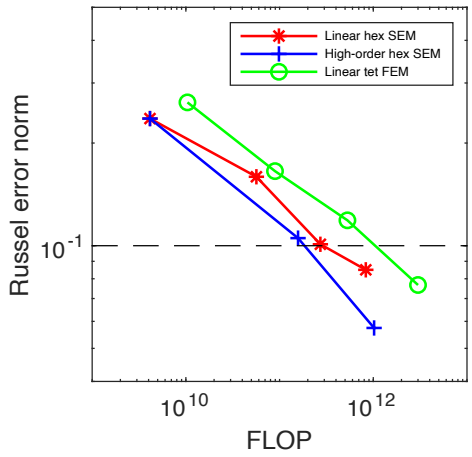

Figure 3.13 Structural velocity Russell error norm at sample point 1 (TFM)

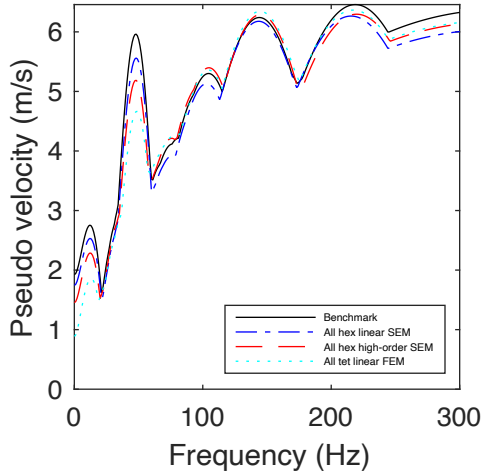

Figure 3.14 SRS at sample point 1 (TFM)

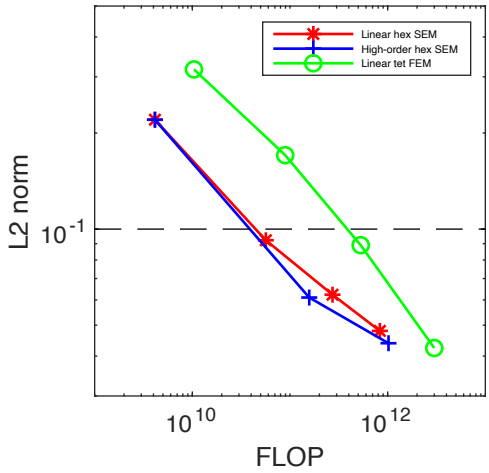

Figure 3.15 SRS L2 error norm at sample point 1 (TFM)

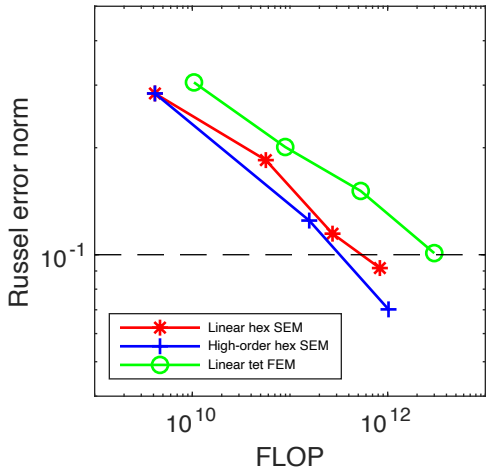

Figure 3.16 Structural velocity Russell error norm at sample point 2 (TFM)

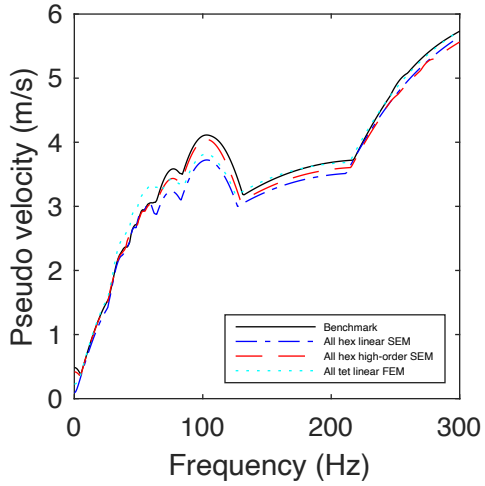

Figure 3.17 SRS at sample point 2 (TFM)

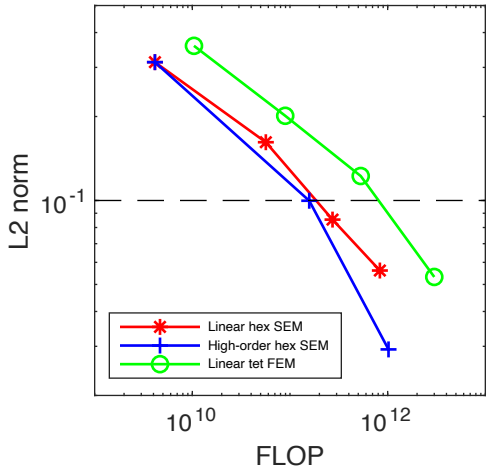

Figure 3.18 SRS L2 error norm at sample point 2 (TFM)

3.3.3.2 SFM structural response fluid mesh efficiency comparison

In this section, the same mesh type comparison performed with the TFM is repeated for SFM. As shown in Figure 3.19 and Figure 3.21, the all-hex linear SEM mesh outperforms the all-hex high-order SEM mesh while both are more accurate than the all-tet linear FEM mesh. This result is more evident at the second sample point where the advantage of the all-hex linear SEM mesh becomes even larger as the mesh is refined. The somewhat degraded behavior of the all-hex high-order SEM mesh may be explained by the less accurate representation of the boundary geometry. As stated in the introduction, the base element size of the high-order SEM mesh is larger than the linear SEM mesh with the same refinement level, thus the boundary geometry is less accurately captured. The high-order SEM accuracy observed using TFM may be due to the increased error from the boundary being compensated by better simulation of the incident wave propagation which is not solved in SFM.

The SRS error results on the first sample point shown in Figure 3.20 are similar in trend to the velocity response (Figure 3.19). On the second sample point (Figure 3.22), the advantage of the all-hex linear SEM mesh at the first sample point is less clear until the mesh is highly refined. Overall, the mesh type with the highest computational efficiency is not as obvious as in the TFM case. The all-hex mesh generated by the Sculpt algorithm using the linear SEM is better for SFM, but perhaps only in this limited sample and there may also be other issues with SFM as discussed in the next section.

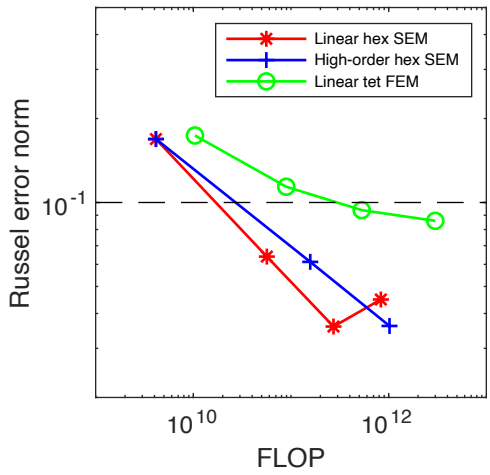

Figure 3.19 Structural velocity Russell error norm at sample point 1 (SFM)

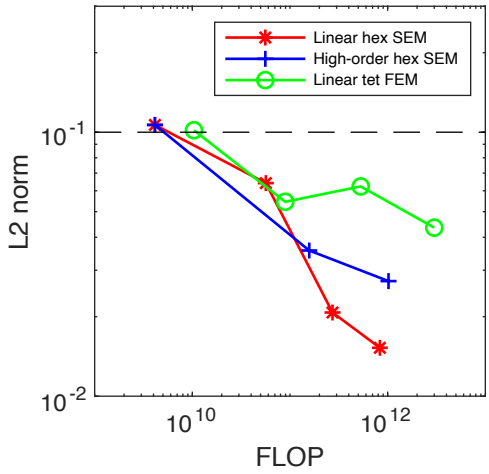

Figure 3.20 SRS L2 error norm at sample point 1 (SFM)

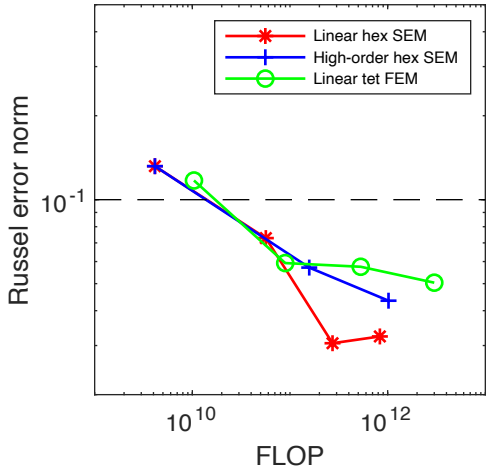

Figure 3.21 Structural velocity error norm on sample point 2 (SFM)

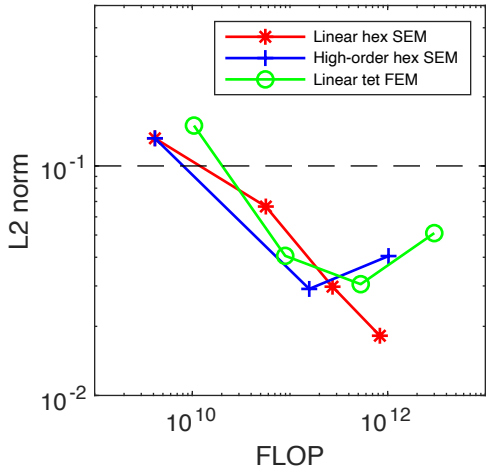

Figure 3.22 SRS error norm on sample point 2 (SFM)

3.3.4 Further comparison between Scattered Field Model and Total Field Model

Although the Scattered Field Model (SFM) has the potential to be more accurate than the Total Field Model (TFM) with the same amount of computation since the incident wave is propagated without dispersion, it may not replicate the correct physics as stated in Section 3.2.2.3. In this section, two surface ship numerical experiments with different charge locations are used to investigate this problem (see Figure 3.23). The first charge is placed directly below the keel at a depth of 18.288m (60ft) on the centerline and the second charge is placed at a depth of 6.096m (20ft) and 15.24m (50ft) to the port side. It seems clear that the shock wave from the second charge would be affected by the hull leaving a large region on the starboard side in shadow (see Figure 3.23), whereas the shock wave from the first charge would directly impact the entire wetted hull surface, which is more consistent with the SFM assumptions. Here, the structural velocity response is sampled at a point on the starboard hull surface located at (69.5m, -1.70m, -9.27m). The rest of the case configuration follows Section 3.3.1.2 if not otherwise specified. It can be seen from the result in Figure 3.24 that the TFM and SFM results show little difference for the first charge location which is expected. For the second charge location, Figure 3.25 shows that the TFM and SFM results agree well until around 12ms. After that (near 15ms), the SFM result reaches a larger peak velocity than the TFM result. The agreement in the early result is due to the actual incident wave passing through the hull structure ahead of the fluid which is modeled correctly by both methods, but once the assumed incident wave reaches the shadow side of the hull and effectively enters the fluid (15 ms), the velocity is over-predicted.

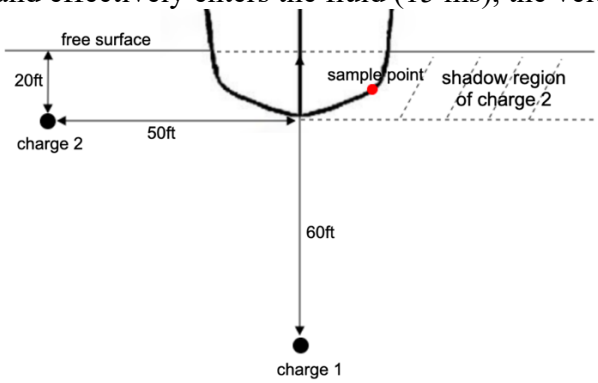

Figure 3.23 Charge location configuration

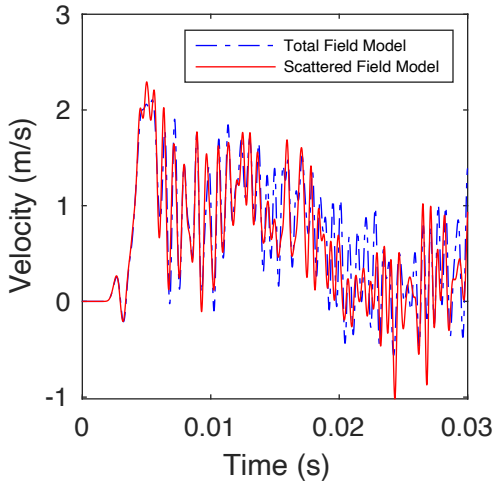

Figure 3.24 Structural velocity comparison for the first charge location

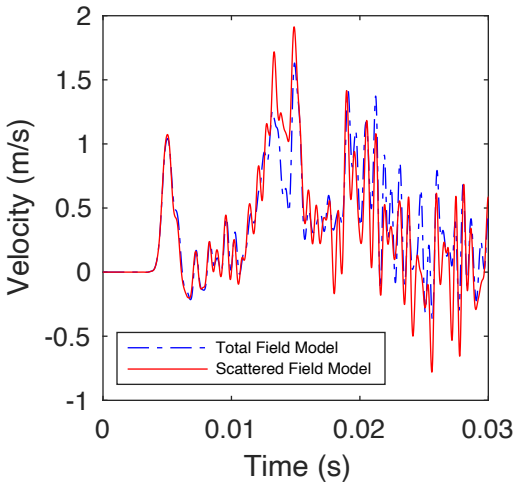

Figure 3.25 Structural velocity comparison for the second charge location

Given that the original SFM over-predicts the structural response for charge configurations with a shadow zone, a modified SFM was implemented. In this modification, the fluid nodes in the shadow (blocked by the structure) are identified by determining if the line connecting the node and the charge center intersects with the structural wetted surface elements. Incident pressure is then not prescribed on these shadow points throughout the simulation. As shown in Figure 3.26, the surface ship case with the second charge location and modified SFM shows better agreement with the TFM in terms of the peak velocity than the original SFM model although the modified SFM does not consider the diffraction effect of the incident wave which might be important in certain cases. Our overall, but preliminary assessment is that the combination of the modified SFM fluid model and all-hex mesh using linear SEM elements is the most computationally advantageous approach investigated in this work.

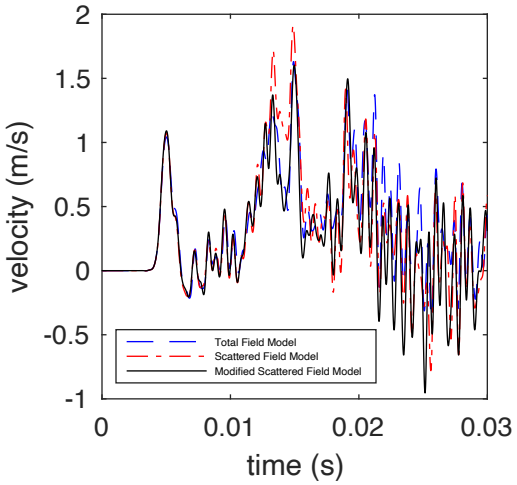

Figure 3.26 Structural velocity comparison for the second charge location

3.4 Conclusion

In this paper, several fluid mesh types and modeling techniques for modeling the far-field UNDEX problem are assessed. Specifically, an all-tet linear FEM mesh generated by the Delaunay refinement algorithm, an all-hex linear SEM mesh generated by the Sculpt algorithm and an all-hex high-order SEM mesh generated by the Sculpt algorithm are compared using both Total Field Model (TFM) and Scattered Field Model (SFM) methods. All of these meshes are created using automatic mesh generation which is very desirable in surface ship design applications. The tet linear FEM element and hex linear/high-order SEM element are first compared in an acoustic wave propagation study. The result shows that the hex high-order SEM element has the highest accuracy for the same computation and the hex linear SEM element is superior to the tet linear FEM element. Next, a far-field UNDEX FSI framework coupling an in-house fluid solver and Abaqus structural solver is assembled and assessed by two benchmark cases. Following the case configuration of the second benchmark study, the three mesh types are evaluated in a surface ship case. If the TFM is used in the fluid solver, the all-hex high-order SEM mesh shows the highest computational efficiency followed by the all-hex linear SEM mesh and all-tet linear FEM mesh. The coincidence of this result with the acoustic wave propagation result reveals the importance of capturing the acoustic wave accuracy in the TFM fluid model. If the SFM is used in the fluid solver, the all-hex linear SEM mesh outperforms the high-order SEM mesh and the all-tet linear FEM mesh. The reason that the computational advantage of the high-order SEM mesh is not achieved in the SFM may be because the boundary geometry is less accurately represented. Finally, the shadow effect of the SFM is demonstrated and a modified SFM method is tested and proven effective. Due to the more computationally efficient nature of the SFM, the best strategy to model the fluid domain indicated in this paper is to use a combination of the modified SFM and hex linear SEM mesh generated by the Sculpt algorithm.

Reference

[1] A. H. Keil, “The Response of Ships To Underwater Explosions,” in *Transactions of Society of Naval Architects and Marine Engineers*, 1961.

[2] W. D. Reid, *The Response of Surface Ships to Underwater Explosions*. Melbourne, Vic. :

DSTO Aeronautical and Maritime Research Laboratory, 1996.
[3] K. Makinen, "Cavitation Models for Structures Excited By a Plane Shock Wave," *J. Fluids Struct.*, vol. 12, pp. 85–101, 1998.
[4] S. L. Wood and Y. S. Shin, "Cavitation Effects on a Ship-Like Box Structure Subjected to an Underwater Explosion," Naval Postgraduate School, 1998.
[5] J. A. DeRuntz, T. L. Geers, and C. A. Felippa, "The Underwater Shock Analysis (USA) Code, a Reference Manual," 1978.
[6] Y. S. Shin and N. A. Schneider, "Ship Shock Trial Simulation of USS Winston S. Churchill (DDG 81): Modeling and Simulation Strategy and Surrounding Fluid Volume Effects," in *74 th Shock and Vibration Symposium*, 2003.
[7] Z. Zong, Y. Zhao, and H. Li, "A Numerical Study of Whole Ship Structural Damage Resulting from Close-In Underwater Explosion Shock," *Mar. Struct.*, vol. 31, pp. 24–43, 2013.
[8] H. Wang, X. Zhu, Y. S. Cheng, and J. Liu, "Experimental and numerical investigation of ship structure subjected to close-in underwater shock wave and following gas bubble pulse," *Mar. Struct.*, vol. 39, pp. 90–117, 2014.
[9] T. C. Baudouin, J. F. Remacle, E. Marchandise, F. Henrotte, and C. Geuzaine, "A frontal approach to hex-dominant mesh generation," *Adv. Model. Simul. Eng. Sci.*, vol. 1, no. 1, pp. 1–30, 2014.
[10] A. T. Patera, "A Spectral Element Method for Fluid Dynamics: Laminar Flow in a Channel Expansion," *J. Comput. Phys.*, vol. 54, no. 3, pp. 468–488, 1984.
[11] M. A. Sprague and T. L. Geers, "A Spectral-Element/Finite-Element Analysis of a Ship-Like Structure Subjected to an Underwater Explosion," *Comput. Methods Appl. Mech. Eng.*, vol. 195, no. 17–18, pp. 2149–2167, 2006.
[12] B. Klenow, "Finite and Spectral Element Methods for Modeling Far-Field Underwater Explosion Effects on Ships," Virginia Tech, 2009.
[13] A. Zhang, S. Ren, Q. Li, and J. Li, "3D Numerical Simulation on Fluid-Structure Interaction of Structure Subjected to Underwater Explosion with Cavitation," *Appl. Math. Mech. (English Ed.*, vol. 33, no. 9, pp. 1191–1206, 2012.
[14] M. A. Taylor and B. A. Wingate, "A generalized diagonal mass matrix spectral element method for non-quadrilateral elements," *Appl. Numer. Math.*, vol. 33, pp. 259–265, 2000.
[15] S. J. Owen, M. L. Staten, and M. C. Sorensen, "Parallel Hex Meshing from Volume Fractions," *Proc. 20th Int. Meshing Roundtable*, vol. 90, pp. 161–178, 2011.
[16] Csimsoft, "Bolt Automatic Hex Meshing User's Guide." 2016.
[17] S. J. Owen, "Parallel Smoothing for Grid-Based Methods," *21st Int. Meshing Roundtable*, p. 6, 2012.
[18] S. J. Owen and T. R. Shelton, "Validation of Grid-Based Hex Meshes with Computational Solid Mechanics," *Proc. 22nd Int. Meshing Roundtable*, 2013.
[19] M. A. Sprague and T. L. Geers, "A Spectral-Element Method for Modelling Cavitation in Transient Fluid-Structure Interaction," *Int. J. Numer. Methods Eng.*, vol. 60, no. 15, pp. 2467–2499, 2004.
[20] Dassault Systèmes Simulia, "Abaqus 6.14 Theory Guide," 2014.
[21] C. A. Felippa and J. A. DeRuntz, "Finite Element Analysis of Shock-induced Hull Cavitation," *Comput. Methods Appl. Mech. Eng.*, vol. 44, no. 3, pp. 297–337, 1984.
[22] R. H. Cole, *Underwater Explosions*. Princeton University Press, 1948.
[23] M. Swisdak, "Explosion Effects and Properties: Part II – Explosion Effects in Water,"

Washington, DC, 1978.
[24] C. Farhat, M. Lesoinne, and P. Le Tallec, “Load and Motion Transfer Algorithms for Fluid/structure Interaction Problems with Non-matching Discrete Interfaces: Momentum and Energy Conservation, Optimal Discretization and Application to Aeroelasticity,” *Comput. Methods Appl. Mech. Eng.*, vol. 157, no. 1–2, pp. 95–114, 1998.
[25] P. Zhang and T. L. Geers, “Excitation of a fluid-filled, submerged spherical shell by a transient acoustic wave,” vol. 696, no. 1993, pp. 2789–2796, 1993.
[26] A. Zhang, W. Zhou, S. Wang, and L. Feng, “Dynamic Response of the Non-Contact Underwater Explosions on Naval Equipment,” *Mar. Struct.*, vol. 24, no. 4, pp. 396–411, 2011.
[27] Z. Lu and A. J. Brown, “Application of the Spectral Element Method in a Surface Ship Far-Field UNDEX Problem,” *Shock Vib.*, vol. 2019, 2019.

Chapter 4 Surrogate Approaches to Predict Surface Ship Response to Far-field UNDEX in Early-stage Ship Design

(Prepared to be submitted to Journal of Marine Science and Technology)

Zhaokuan Lu, Alan Brown
Department of Aerospace and Ocean Engineering, Virginia Tech, Blacksburg, VA, 24061, USA

Abstract

Numerical simulation of a far-field underwater explosion (UNDEX) and its interaction with a large ship structure is a computationally intensive task requiring the discretization of a large fluid domain. This paper explores surrogate non-numerical approaches to approximate surface ship structural response to far-field UNDEX based on the now classic approach proposed by Keil in 1961 [1]. Instead of the entire time domain history, this work focuses on peak structural responses, which may provide valuable information to guide equipment arrangement in early-stage ship design to minimize shock effects. The shock factor response equation as proposed by Keil is refined to improve its performance in predicting peak structural responses at different locations in the ship. This refinement is accomplished by using structural response simulation data with a range of shock factor values in two different applications including a ship structure to determine and assess the linear relationship consistent with Keil's original formulation. The results show that Keil's linear relationship between shock factor and peak structural response is reasonable. As a result, the shock factor may be employed to approximate peak structural response. Peak structural responses predicted using the shock factor are compared to results using a numerical fluid model, and the feasibility of using a surrogate fluid model is assessed. Application examples using the shock factor are presented.

Keywords: UNDEX, Early-stage ship design, Surrogate model, Shock factor, Statistical analysis

4.1 Introduction

In far-field UNDEX where the explosive is located far enough from the ship, and/or the charge weight is small, the major UNDEX to ship interaction comes from the shock wave and its impact on personnel and equipment inside the ship. Although the structural deformation is mostly elastic, a significant amount of energy is passed into the ship as a stress wave, causing sudden motion of structural foundations where critical equipment may be installed [1]. Far-field UNDEX also creates local cavitation caused by the inward motion of plate panel under shock and bulk cavitation caused by the reflection of the shock wave from the free surface. In this work, we focus on this far-field UNDEX problem. In order to assess the vulnerability of surface ships to far-field UNDEX, shock trials are sometimes conducted to understand the structural response to various shocks at different locations onboard. Due to the expensive and environmentally unfriendly nature of shock trials and their very limited value in early-stage design, attention has been given to numerical simulations, but these simulations can be computationally expensive and require detail not available in early-stage design.

Ship concept exploration requires the consideration of potentially thousands of designs at a very limited level of detail. Using a numerical model to investigate UNDEX shock effects in each design variant is difficult or impossible. In related early studies, peak structural response has been used as a metric to quantify the level of shock response of the ship structure (e.g., [2]

[3]). In early stage ship design, peak structural response may provide useful information to guide equipment arrangement location. Although researchers are trying to make numerical simulation more efficient (e.g., [4]–[6]), non-numerical methods provide a reasonable approach until more effective and efficient methods are available. Keil [1] proposed a conceptual shock factor as a function of charge weight, orientation relative to the ship, distance from the ship, ship type, ship location, and installation type. His expression is based on the energy density in the shock wave arriving at the ship hull. Keil stated that the structural velocity response can be linearly scaled by this shock factor. This shock factor is later applied to a submarine-like structure by O'Hara [7]. Zhang [8] proposed a modified shock factor for small cylindrical objects to account for the shock wave scattering effect. The modified shock factor linearly scales the peak acceleration of the structure response successfully. Guo [9] adopted the Keil shock factor for a SWATH catamaran with adjustments to consider the shock wave shadowed by the double-hull structure. In the Guo study, similar structural response is found under equal shock factor conditions. Although the shock factor is frequently used to quantify the shock severity imposed on surface ships (e.g., [10]), a generalized shock factor for the surface ship that can be used to predict peak structural responses under different far-field UNDEX events and at different locations in the ship has never been fully explored.

In order to study the linear relationship between the structural response and the shock factor, regression analyses are performed. A Cavitating Acoustic Spectral Element (CASE) fluid solver and coupled Abaqus structural solver FSI framework built by Lu and Brown [11] is used to collect structural response data for regression. Although more efficient than its counterparts, the CASE fluid solver is still computationally expensive if used to run a large number of cases. G.I. Taylor [12] proposed one of the first analytical schemes to model the FSI effect for a structure interacting with an underwater shock wave. Specifically, an infinite air-backed rigid plate under plane shock wave impact is analyzed. The fluid domain is modeled by assuming it is perfectly acoustic, and thus the effect of the fluid can be prescribed as a structural boundary condition. This Taylor Plate model is much faster than numerical models which require spatial discretization of the fluid domain. The Taylor Plate model has been used to build simplified models to calculate the momentum transmission and FSI effect of a sandwich plate under shock impact (e.g., [13], [14]). The Taylor Plate model was also extended to a water-backed plate by Liu [15] to understand the shock response of a submerged structure. It is used to study UNDEX effects on a rigid Floating Shock Platform (FSP) by Sebert [16] with results compared to experimental data. Reasonable results for the velocity time history were obtained in the first few milliseconds, after which the Taylor Plate solution deteriorates because of the inception of cavitation, making the fluid no longer entirely acoustic. The Taylor Plate model is usually not used for underwater explosion simulations due to the existence of more sophisticated numerical models. However, the peak response often occurs in the early time of the response, possibly making the need to use more sophisticated models unnecessary. Mathew [17] compared the structural velocity response of an elastic FSP obtained using the Taylor Plate Model to results using the CASE fluid solver. Excellent agreement is found in the structural velocity response for the first few milliseconds. However, this performance cannot be generalized for surface ships which are much larger and more structurally complex. If the peak structural response when the Taylor Plate model is employed in surface ships is sufficient to generate data for regression, the numerical fluid model (e.g., CASE) which consumes more computational resources and time could be replaced. Once Keil's linear relationship for one ship design is established it may be applicable to "similar" ships so numerical (or Taylor plate) analyses may only be required for a

single baseline design. For significantly different designs, additional numerical or Taylor plate analyses would likely be required, making the possible use of the Taylor plate approach even more advantageous.

In the following sections, we first present the shock factor formulation for peak structural response. Then the assumed linear relationship is determined and assessed using two benchmark problems with the structural response data generated using a CASE-Abaqus coupled solver. Finally, the feasibility of replacing the CASE fluid model with the Taylor Plate model is evaluated.

4.2 Shock Factor and Modifications

In Section 4.2.1, the original shock factor defined by Keil [1] and an approach to improve correlation with peak velocity response is described. The idea of the shock factor is then extended in Section 4.2.2 to consider peak acceleration response which is another essential factor to quantify shock severity.

4.2.1 Peak velocity shock factor

In the original description, Keil defined shock factor as:

$$SF_0(\vec{X}_c, w) = \frac{w^{\frac{1}{2}}}{R_0} cos\ (\theta_0) \tag{4.1}$$

to describe the shock wave energy density applied on the ship hull surface. $\vec{X}_c$ and w represent the charge center and charge weight. R_0 is the distance from the charge to a reference point $\vec{X}_0$ on the ship usually defined at mid-keel by Keil and others, and θ_0 is the orientation of charge relative to the reference point (see Figure 4.1).

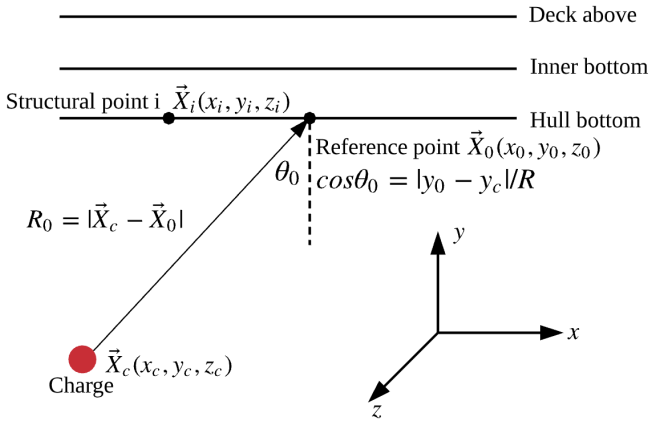

Figure 4.1 Original Keil shock factor definition

The velocity profile of the ship structure at a random point i is expressed as:

$$v_i(t) = C \cdot \bar{v}_i(t) \cdot SF_0\left(\vec{X}_c, w\right) \tag{4.2}$$

where C is a linear coefficient depending on ship type, onboard location, and installation type; $\bar{v}_i(t)$ is a normalized velocity profile. Assuming the ship type and installation type are fixed, C only varies with location. Thus, the peak velocity at a specified structural point i is only proportional to the shock factor SF_0 calculated at a specified reference point:

$$v_i^{peak} = \bar{v}_{peak} \cdot C_i \cdot SF_0\left(\vec{X}_c, w\right) \tag{4.3}$$

To better understand and apply this equation, we add a possible derivation of the shock factor which is missing from the original Keil's paper. Based on the empirical formulation by Cole [18], the energy density of the shock wave front normal to the hull surface is:

$$E_f = \int (p(t)cos\theta)^2 dt = \kappa w^{\frac{1}{3}} \left(\frac{w^{\frac{1}{3}}}{R}\right)^{\gamma} \cos^2\theta \tag{4.4}$$

where κ and γ are constant coefficients given in [18], θ is the angle between the shock wave propagation direction and the normal of the hull surface, and R is the distance from the charge center to the point on the hull. The energy that enters the ship is assumed to be a constant fraction of the total wave energy and expressed as μE_f. If the initial plate velocity is zero, the peak velocity may be expressed as $v^{peak} = \sqrt{\frac{2E}{m}}$ based on a simple kinetic energy definition $E = \frac{1}{2}mv^2$. Combining this expression with Eq. 4.3 and 4.4, the peak velocity at a specific structural node i on the external submerged hull surface may be approximated by:

$$v_i^{peak} \approx \sqrt{\frac{2\mu E_f}{m_i}} = \sqrt{\frac{2\mu k}{m_i}} \frac{\sqrt{w^{1.016}}}{R_i^{1.025}} cos\theta_i \approx \sqrt{\frac{2\mu k}{m_i}} \frac{\sqrt{w}}{R_i} cos\theta_i \tag{4.5}$$

where m_i is proposed as the effective mass or inertia for point i. If $\theta_i = 90°$, the peak velocity v_i^{peak} would become zero, however, this is not physically correct since the wave still excites the structure at a glancing angle. To account for the transient wave excitation when the shock wave is oblique (large θ_i), an angle function is added to Eq. 4.5 as in [1]:

$$v_i^{peak} \approx \sqrt{\frac{2\mu k}{m_i}} \frac{\sqrt{w}}{R_i} (\eta + (1-\eta)cos\theta_i) \tag{4.6}$$

where η is a constant coefficient to be determined from experiment. Defining a velocity shock factor as:

$$SF_i(\vec{X}_c, w) = \frac{\sqrt{w}}{R_i} (\eta + (1-\eta)cos\theta_i) \tag{4.7}$$

based on structural node i location $\vec{X}_i$ and $l_i = \sqrt{\frac{2\alpha k}{m_i}}$, Eq. 4.6 becomes:

$$v_i^{peak} = l_i SF_i \tag{4.8}$$

The reference point where R_i and θ_i are defined is based on the location of the structural point i instead of being a single point for all structural points. In the shock factor used hereafter, the reference point X_0^i is defined depending on the location of the individual structural point i (see Figure 4.2). For a structural point on the hull surface, the reference point coincides with the structural point itself. For the points on the inner bottom and decks above, the selection of hull reference points is proposed and discussed in Section 4.2.3. The peak velocity v_i^{peak} at structural node i may be estimated by the shock factor SF_i once the linear coefficient l_i is known.

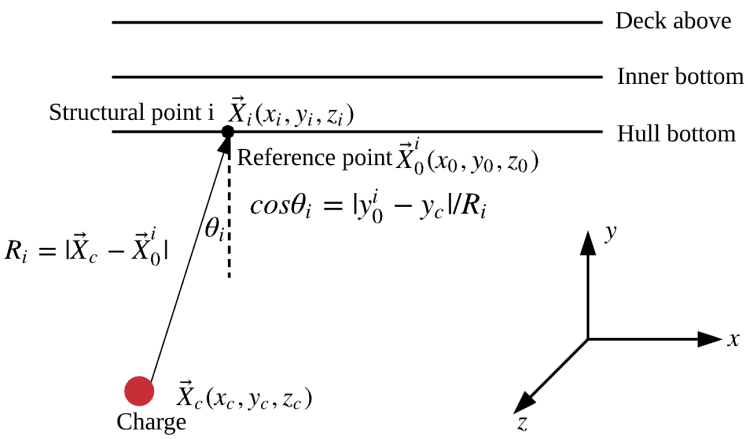

Figure 4.2 Modified Keil shock factor definition

4.2.2 Peak acceleration shock factor

Following the example of the velocity shock factor derivation described in Section 4.2.1, the acceleration shock factor is defined. If the peak acceleration is desired, the peak pressure (P^m) similitude expression found in [18] is used:

$$P^m = \epsilon \left(\frac{w^{\frac{1}{3}}}{R} \right)^{\tau} \tag{4.9}$$

where ϵ and τ are constant coefficients given in [18] and P^m is the peak pressure of the shock wave. The maximum nodal force acting on structural node i can be estimated by:

$$F_i^m \approx P_i^m A_i = A_i \epsilon \left(\frac{w^{\frac{1}{3}}}{R_i} \right)^{\tau} (\eta + (1-\eta) cos\theta_i) \tag{4.10}$$

where A_i is the equivalent area of node i to convert nodal pressure to nodal force. The definition of R_i, θ_i, and η follows that in Section 4.2.1. The peak acceleration (a_i^{peak}) at the structural point i becomes:

$$a_i^{peak} = \frac{F_i^m}{m_i} = \frac{A_i \epsilon}{m_i} \left(\frac{w^{\frac{1}{3}}}{R_i} \right)^{\tau} (\eta + (1-\eta) cos\theta_i) \tag{4.11}$$

Defining the acceleration shock factor as:

$$SFA_i(\vec{X}_c, w) = \left(\frac{w^{\frac{1}{3}}}{R_i} \right)^{\tau} (\eta + (1-\eta) cos\theta_i) \tag{4.12}$$

and with $q_i = \frac{A_i \epsilon}{m_i}$, the peak acceleration can be estimated as:

$$a_i^{peak} = q_i SFA_i \tag{4.13}$$

Linear coefficients l_i and q_i can then be determined experimentally or using a numerical model.

4.2.3 Categorizing the structural locations

For clarity, a point on the ship hull bottom has been used as an example to derive the shock factor in Sections 4.2.1 and 4.2.2. However, equipment sensitive to shock may be located throughout the ship. The shock response can vary significantly between decks [19]. Even on the same deck, the response is different. For instance, the inner bottom location on top of the longitudinal girder or floor (see Figure 4.3) is vertically connected directly to the hull surface which is directly exposed to the fluid shock excitation. As a result, the structural response in this location shows an almost immediate kick-off motion as soon as the fluid shock wave arrives, followed by a rebound and oscillation caused by the local cavitation. The oscillation is then gradually damped by the fluid. However, away from the primary structural members, the structure is not vertically connected to the hull surface, the stress wave path instead comes from the side hull and adjacent bulkhead horizontally within the same grillage. Due to the longer and more complicated stress wave path, the energy/load that reaches the structure is significantly smaller. Because of this and the smaller vertical stiffness, the kick-off motion is not as strong and instantaneous as at the location supported by primary structural members. On the decks above the inner bottom, the stress wave path is even more complicated due to the greater distance from the fluid. The fluid damping barely affects the damping on the decks above, which leads to prolonged oscillation. The points on the decks above the inner bottom can also be categorized into the locations supported by longitudinal girders or frames and locations only supported by regular stiffeners since the response pattern can be different due to the different stiffness. Hereafter, we call locations supported by primary structural members (i.e., girders, floors, frames) primary locations and those supported only by secondary structural members (plates and stiffeners) secondary locations. Due to the different response features and excitation paths at these different characteristic locations, they are treated separately in terms of evaluating the linear relationship between the shock factor and the peak structural response.

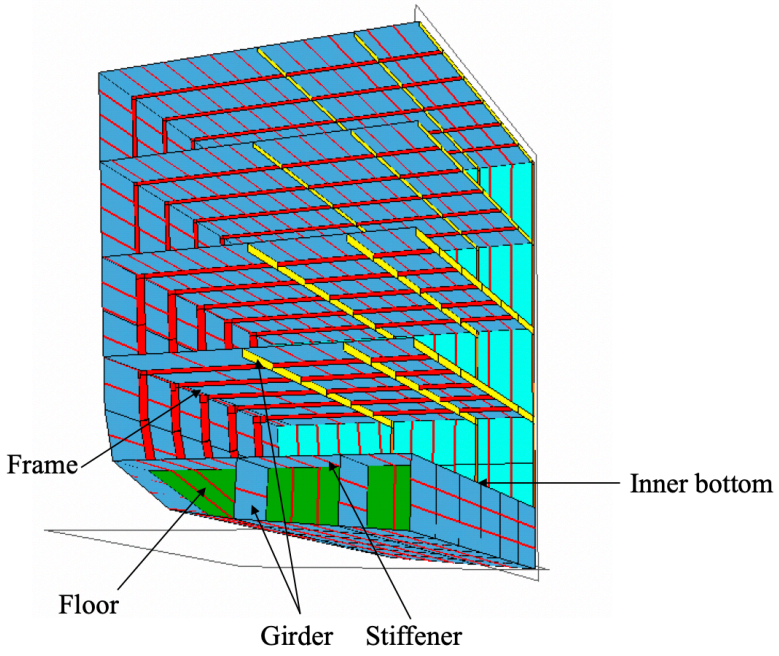

Figure 4.3 Ship structure visualization (half symmetric)

Referring to Eq. 4.5 and Figure 4.1, the reference point X_i^0 can be defined depending on where the structural point is. On the hull surface, the hull reference point shares the same location as the structural point because the structure is directly exposed to fluid. The internal structural points, however, are indirectly excited as stated before. A variation of the shock factor prediction model Eq. 4.8 and Eq. 4.13 may be defined as:

$$v_i^{peak} = \sum_{j=1}^{n} l'_{ij} \cdot SF_j \tag{4.14}$$

$$a_i^{peak} = \sum_{j=1}^{n} q'_{ij} \cdot SFA_j \tag{4.15}$$

These equations estimate the peak response of structural point i by a linear combination of the shock factor at multiple reference points. In Eq. 4.14 and Eq. 4.15, i denotes the structural point, n is the number of hull reference points represented by j, and l'_{ij} and q'_{ij} are linear coefficients. The reference points may be chosen at the intersection of deck, hull surface and bulkhead where the majority of the shock wave enters the ship (see Figure 4.4) or may be selected more generally using any matrix of hull points.

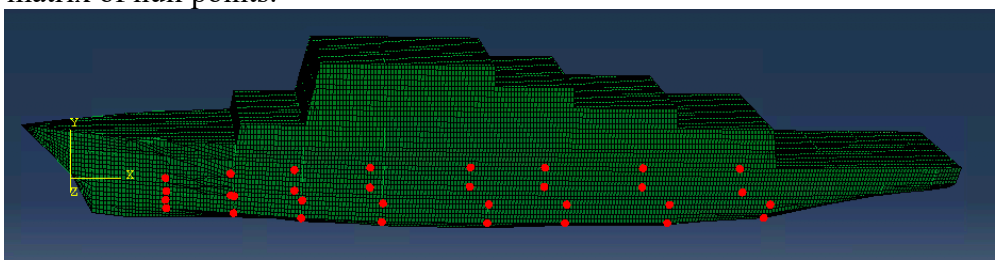

Figure 4.4 Reference points on hull surface

In this test case, we use only a few hull reference points in the vicinity of the internal structural point i. The shock factors at the reference points are interpolated to a single representative shock factor SF_i. The hull reference points are defined at the locations where the stress wave paths intersect with the hull surface. The intersection is assumed to be the direct-path point where the shock wave that reaches the internal structural point enters the ship. Since an internal point might be excited by more than one wave paths, there can be several reference points. To demonstrate the selection of reference points for shock factor calculation at different characteristic locations, a ship section bounded by two bulkheads is used for demonstration (Figure 4.6 to Figure 4.9 in Sections 4.2.3.1 to 4.2.3.4). The decks are numbered as shown in Figure 4.5. The selection of reference points for these different cases was largely guided and assessed by their ability to achieve the best correlation between the shock factor function prediction result and the actual numerical results. Detailed results are presented in Table 4.2~Table 4.5 and discussed in Section 4.4.

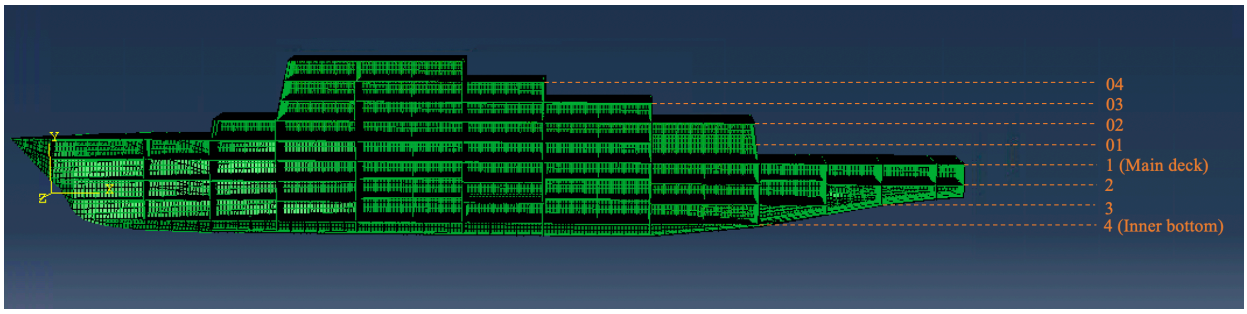

Figure 4.5 Ship decks naming convention

4.2.3.1 Deck 4 primary location

For the deck 4 (inner bottom) primary location (see Figure 4.6), the hull surface point vertically connected to the structural point by girder/floor is used as one of the reference points (point 3). To account for the shock wave entering horizontally into the deck, two points on the hull surface with the same longitudinal location as the structural point are used as the reference point as well (point 1&2). The stress wave path is shown in red dotted line. The resultant shock factor on structural node i is calculated by inverse distance interpolation of the shock factor SF_j on the reference points:

$$SF_i = \sum_{j=1}^{3} w_j SF_j \Big/ \sum_{j=1}^{3} w_j \tag{4.16}$$

$$w_j = 1/d_j \tag{4.17}$$

where d_j is the distance from the reference point j to the structural point i and w_j is the interpolation weight.

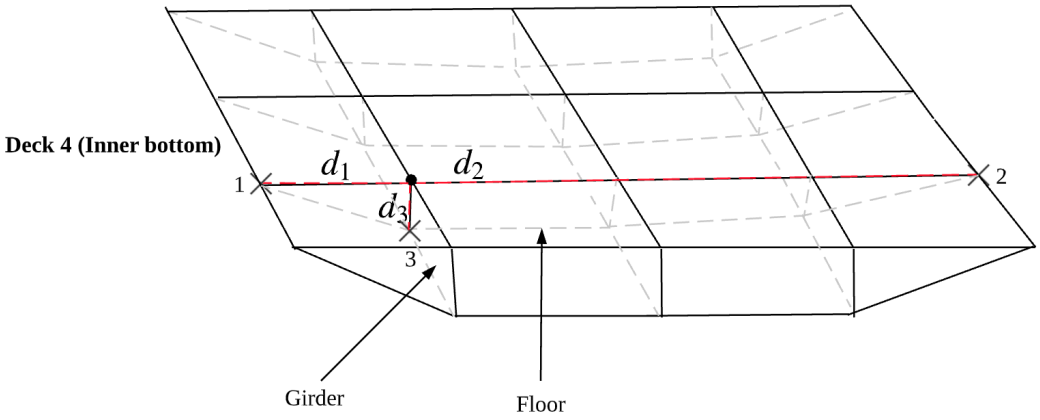

Figure 4.6 Deck 4 primary location

4.2.3.2 Deck 4 secondary location

For structure points not on the primary structural parts (see Figure 4.7), the load path is more complicated. The reference points in the transverse direction (point 1&2) are defined as the same as the primary location. Since the bulkhead tends to be stiffer than the floors and thus

carries more energy/load, the reference point in the longitudinal direction is chosen on the intersection of bulkhead and hull surface (point 3&4). Note that a_3 and a_4 consider the distance traveled on both the bulkhead and the deck.

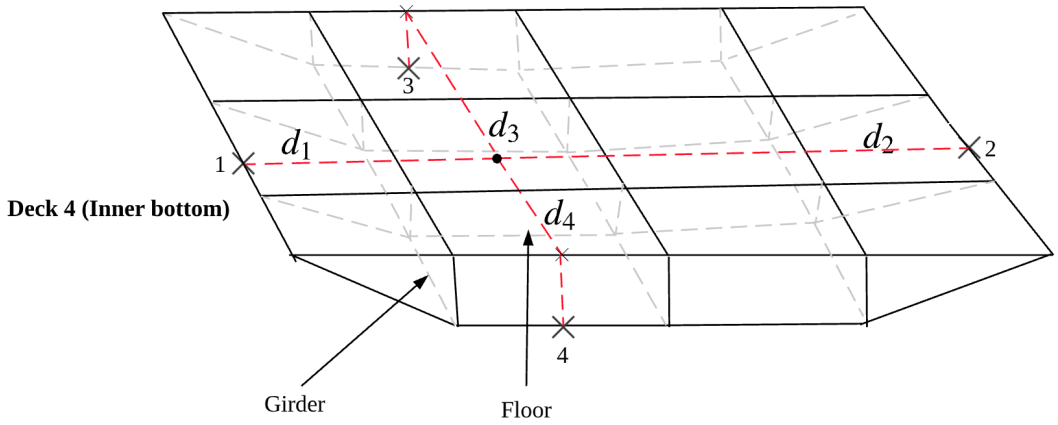

Figure 4.7 Deck 4 secondary location

4.2.3.3 Deck 3 primary and secondary location

For the deck 3 (first deck above the inner bottom) shown in Figure 4.8, both the primary and secondary locations share the same set of reference points which is defined similarly to the inner bottom secondary location because the structural point is not directly connected to the hull surface vertically.

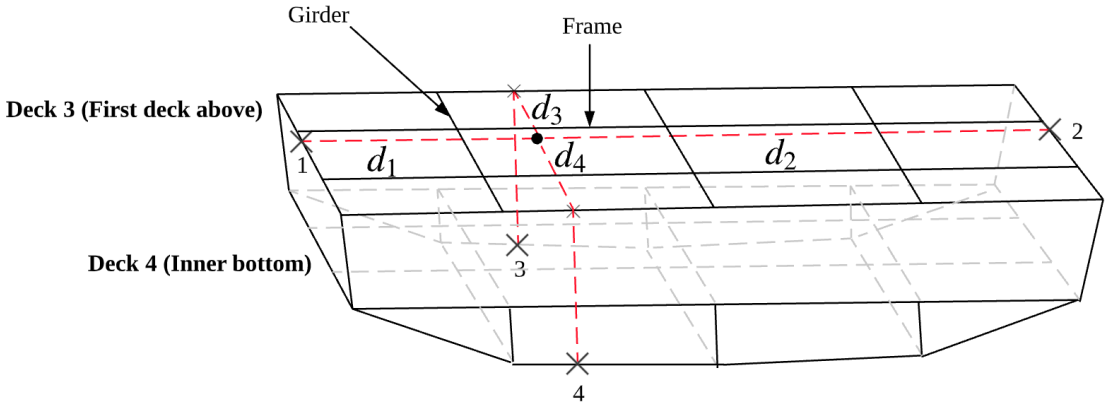

Figure 4.8 Deck 3 primary and secondary location

4.2.3.4 Deck 2 primary and secondary location

For the deck 3, we assume that the waterline is above the deck. As a result, the reference point 1 and 2 are directly exposed to the shock wave from the surrounding fluid. However, if the deck is above the waterline, the wave path is slightly different. The deck 2 (second deck above the inner bottom) shown in Figure 4.9 serves as an example when the deck is above the waterline. In this case, the transverse reference points (point 1&2) on the side-hull shell are located on the uppermost submerged lower deck. For the rest of the decks above the free surface, the rules of

reference point selection follow the deck 2. Therefore, we focus on validating the linear relationship between the shock factor and peak structural response on deck 2, deck 3 and deck 4 in this research.

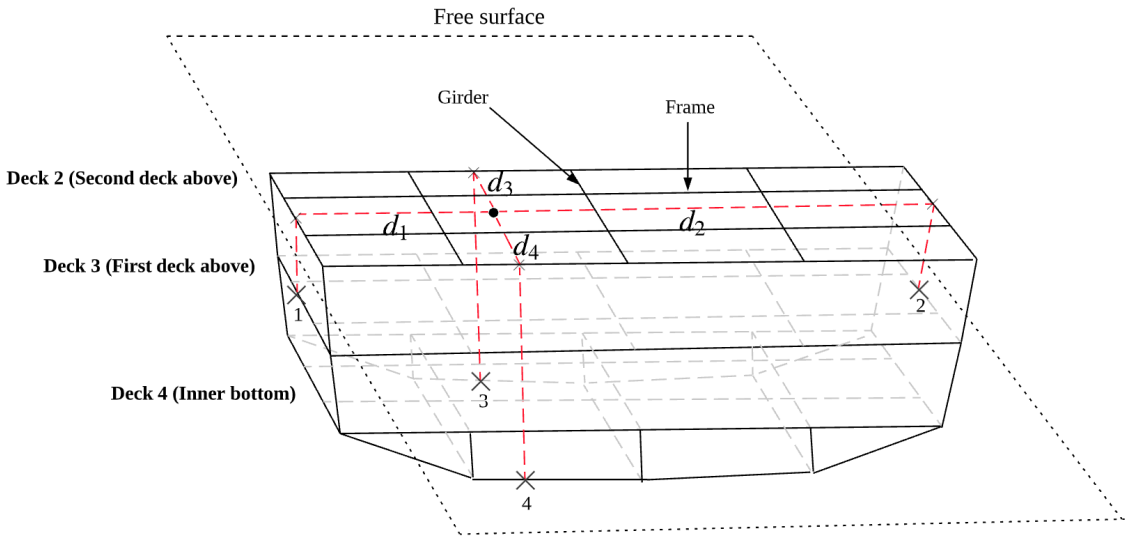

Figure 4.9 Deck 2 primary and secondary location

4.3 Assessment of shock factor

In this section, the linear relationship between the shock factor described in Section 4.2, and the structural peak response is determined and assessed by statistical regression in two UNDEX problems. Specifically, the shock factor prediction model in Eq. 4.8 (peak velocity) or Eq. 4.13 (peak acceleration) are fitted to the structural peak responses and the corresponding shock factor values. The Abaqus-CASE coupled solver is used to generate the structural response data for regression. The strength of the linear relationship is quantified by the coefficient of determination:

$$R^2 = \left(1 - \frac{\sum_i (y_i - f_i)^2}{\sum_i (y_i - \bar{y})^2}\right) * 100\% \tag{4.18}$$

where y_i is the actual response, $\bar{y}$ is the mean actual response, f_i is the predicted response. It shows how well the predicted response by the fitted shock factor prediction model correlates with the actual simulation data. Therefore, high R^2 reflects a strong linear relationship between the structural peak response and the shock factor. Once the l_i and q_i are obtained with satisfactory R^2, the Eq. 4.8 and Eq. 4.13 can be used to predict the peak response for any charge configuration (i.e., charge location and charge weight).

4.3.1 Bleich-Sandler problem

In this section, we test the validity of the shock factor using a Bleich-Sandler problem which involves an air-backed rigid plate under a plane shock wave attack (see Figure 4.10). The detailed case properties can be found in [11]. The Bleich-Sandler problem can be considered as a simplified UNDEX problem. Six charge cases are used to generate the data for regression. The charges are put at a depth ranging from 40 m to 15 m with a 5 m interval. The charge weight is

set as 27.2 kg (60 lb). The peak velocity and acceleration are obtained for each charge configuration. The plate velocity and acceleration response time history under the first charge is shown in Figure 4.11 as an example. The plate is first kicked off by the shock wave. The maximum velocity (zero acceleration) is reached as the shock wave is almost past, and the gradually decreasing fluid pressure due to the upward plate motion and plate gravity sum to a zero total force on the plate.

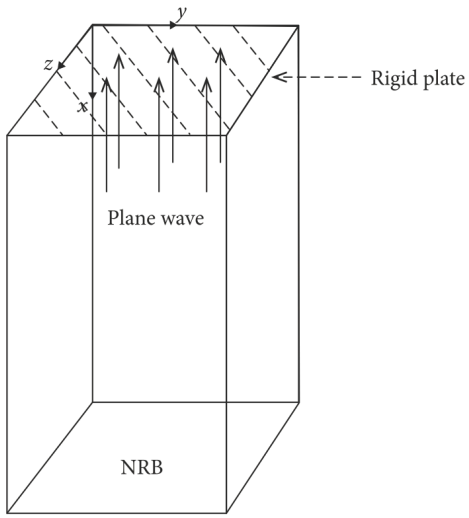

Figure 4.10 Bleich-Sandler case configuration

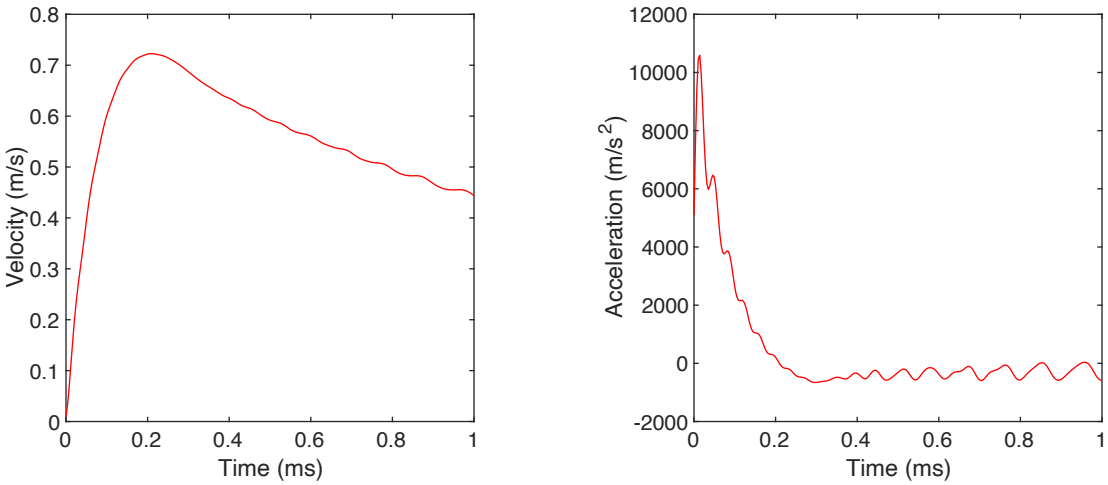

(a) Velocity (b) Acceleration

Figure 4.11 Bleich-Sandler plate velocity and acceleration response time history

The regression results are shown in Figure 4.12 where the x and y axes represent the actual response and the predicted response calculated by the fitted Eq. 4.8 and Eq. 4.13 with $l_i = 13.2\ m/s$ and $q_i = 507226.2\ m/s^2$. The data points represent the structure response to the five charges. If all the data points fall on the diagonal line (red) on the actual-by-prediction plot, the fitted model perfectly predicts the actual data, which implies $R^2 = 100\%$. Figure 4.12 shows the peak structural velocity, and the acceleration response are well predicted by the fitted shock factor prediction model. This reflects a strong linear relationship between the peak velocity and peak acceleration and their corresponding shock factor, which is further supported by the

calculated R^2 value shown in Table 4.1. The excellent behavior of the shock factor in the Bleich-Sandler case provides more confidence for the surface ship case assessed in the next section at least for hull surface panels.

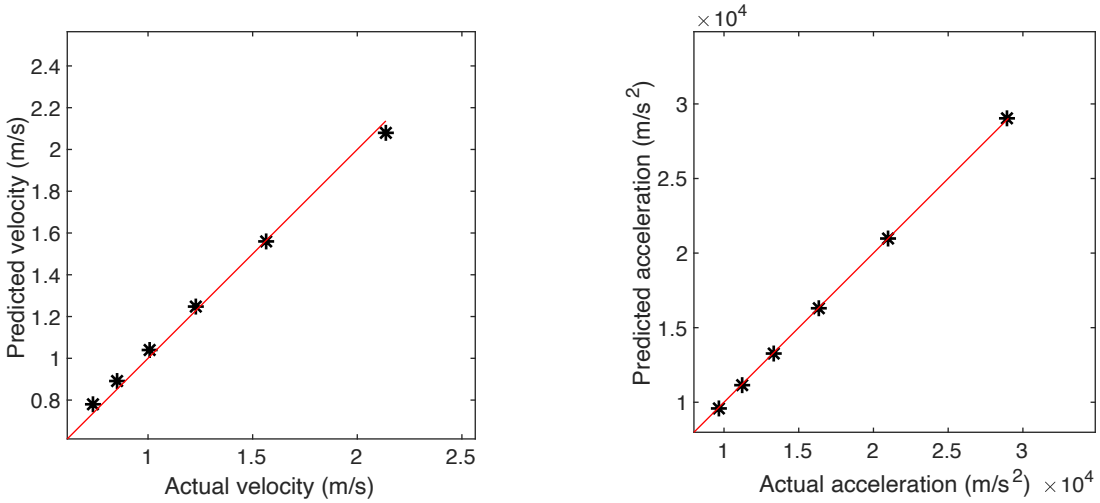

(a) Velocity (b) Acceleration

Figure 4.12 Actual-by-prediction plot for peak velocity and peak acceleration

Table 4.1 R^2 of peak structural response and shock factor

	Velocity	Acceleration
R^2	99.41%	99.99%

4.3.2 Ship problem

In this section, the linear relationship between the peak structural response and the shock factor is assessed in a surface ship UNDEX problem. 30 charges with different weights and locations, selected using a Latin Hypercube approach are placed around the hull (see Figure 4.13). $\eta = 0.2$ is chosen in the shock factor expression (Eq. 4.7 and Eq. 4.12) to deal with oblique shock attack angles. The structural response time history of 30 milliseconds from when the shock wave first touches the ship hull is sampled at a number of points at primary and secondary locations throughout the ship (see Figure 4.14). In addition to the time history, the frequency response is also sampled using a shock response spectrum (SRS). The SRS is a plot of the peak response of a system of single DOF spring-mass oscillators with various natural frequencies to the shock input. It reflects how equipment with different natural frequencies would respond to the shock. To assess the degree of linear relationship, an average R^2 comparing the actual and predicted values of all the sampled points at each characteristic location is calculated. The charge and sampled structural point parameters are provided in Appendix. A.

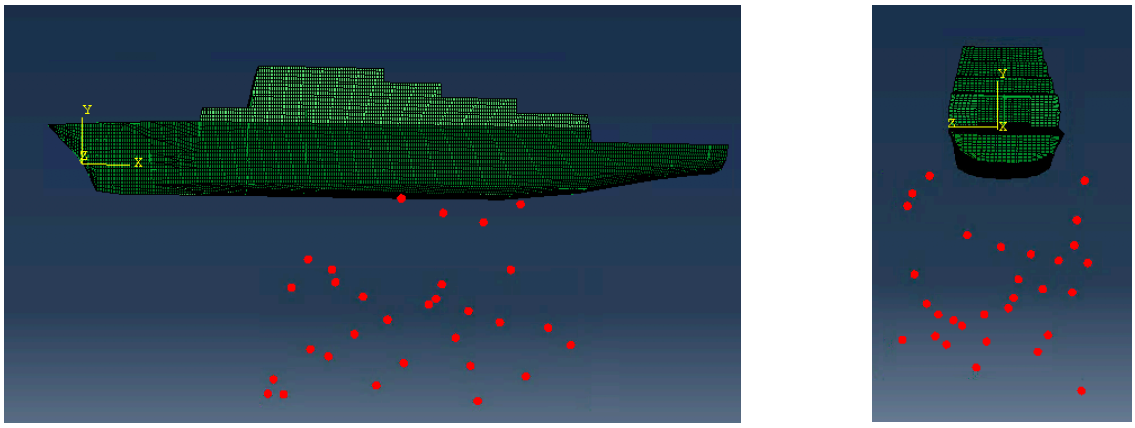

(a) Sideview (b) Rearview

Figure 4.13 Charge distribution visualization

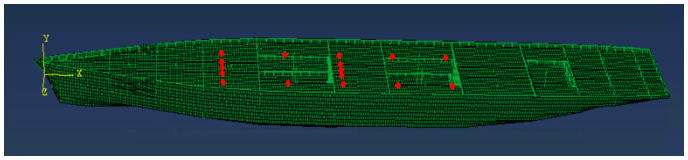

(a) Deck 2 primary location

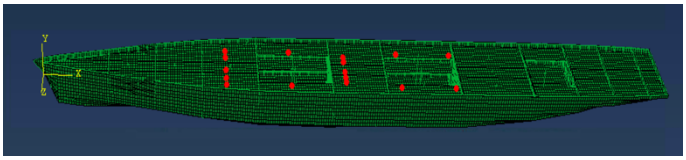

(b) Deck 2 secondary location

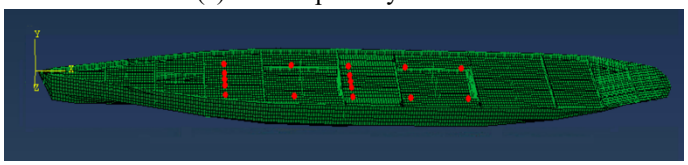

(c) Deck 3 primary location

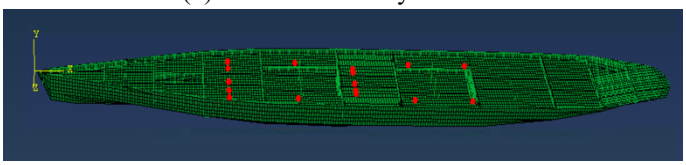

(d) Deck 3 secondary location

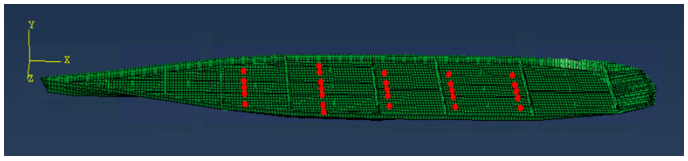

(e) Deck 4 primary location

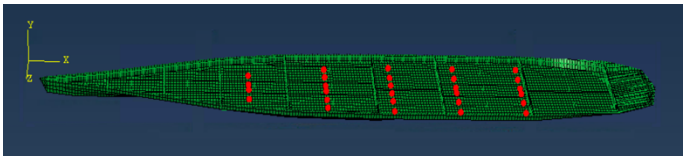

(f) Deck 4 bottom secondary location

Figure 4.14 Sampled structural points at different characteristic locations

4.3.2.1 Velocity shock factor

First, the predicted results of fitting the velocity shock factor prediction model (Eq. 4.8) to the time-history peak velocities and the velocity shock factor are presented. The actual-by-prediction plots for the sampled primary points on deck 4 (inner bottom) are shown as an example (Figure 4.15). Data points on each location plot represent the response of 30 charge cases. Based on the averaged R^2 result in Table 4.2, the structural responses at the deck 4 primary locations have the strongest linear relationship with the shock factor among all the characteristic locations. The relationship becomes significantly weaker at the deck 4 secondary locations. This is because the primary locations are directly excited by the fluid shock wave via the girders/floors vertically connected to the hull surface whereas the secondary locations are excited by a more complicated wave path from the edges of the grillage. The wave path plotted in Figure 4.7 is only one of the routes the wave may take in the structure. For instance, the wave can also keep propagating upward when it reaches the intersection between the bulkhead and deck 4. As a result, the shock factor does not estimate the shock wave energy at the secondary

location as accurately as at the primary location. On deck 2 and deck 3 (decks above the inner bottom), the R^2 of the primary and secondary locations is not as high as their counterparts on deck 4, which may again be explained by the less accurate shock factor energy estimation due to a longer and more complex wave path.

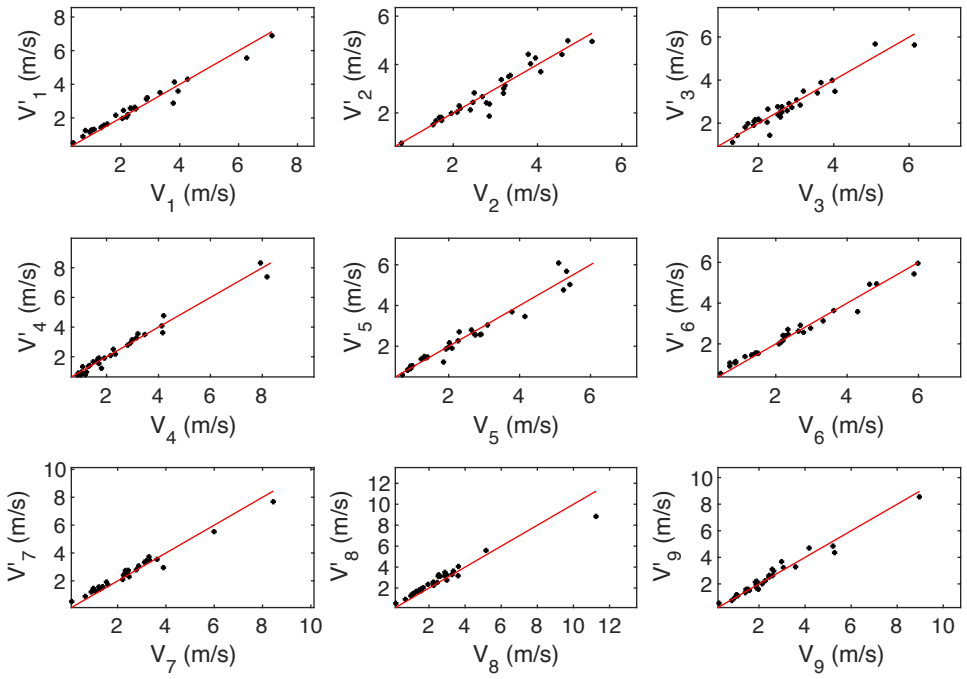

Figure 4.15 Actual-by-prediction plots of deck 4 primary location sampled points 1~9

Table 4.2 R^2 of the time-history peak velocity and shock factor

Location	R^2
Deck 4 primary	93.56%
Deck 4 secondary	81.89%
Deck 3 primary	83.83%
Deck 3 secondary	81.02%
Deck 2 primary	80.59%
Deck 2 secondary	77.46%

Next, the velocity shock response spectrum (SRS) is calculated using the data response time history as input. After plotting the SRS velocity responses to all the test charge cases, it is found that the peak response happens at approximately the same frequency (See Figure 4.16 for the SRS plot at an example structural point). To assess the strength of the linear relationship between the SRS peak velocity and the shock factor, linear regression is performed as before. The actual-by-prediction plot for the deck 4 primary location sampled points is shown in Figure 4.17. The regression result in Table 4.3 shows a similar trend to the time-history peak velocity result in Table 4.2 but with slightly lower R^2 (weaker linear relationship). The peak response in SRS is also subject to the influence of the local cavitation generated after the shock wave passes because the SRS is calculated using the entire 30 milliseconds response time history. Therefore, the velocity shock factor prediction model (Eq. 4.8) does not approximate the SRS peak velocity

as well as the time history peak velocity. Despite this, the correlation between the predicted result and the actual result is still significant.

In design applications, a linearly rise to the maximum response and then flat profile (solid red line in Figure 4.16) envelopes the entire SRS and could serve as an equipment design spectrum. With the natural frequency either from modal analysis or induction from the actual simulation data, a design spectrum can be generated. It should be noted, however, that the design spectrum by this approach does not consider the spectrum dip effect [20] which is caused by the interaction between the equipment and its structural foundation. However, in early-stage ship design, the details of the equipment installation are not yet available. The peak SRS response obtained can be used to compare the relative response strength throughout the ship which may be useful to guide equipment arrangement.

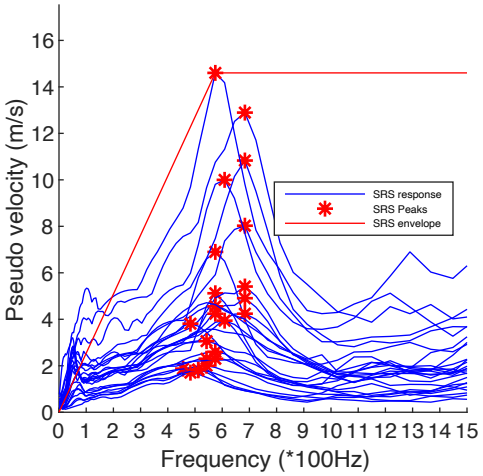

Figure 4.16 SRS plot of the response to all the test charges at an example structural point

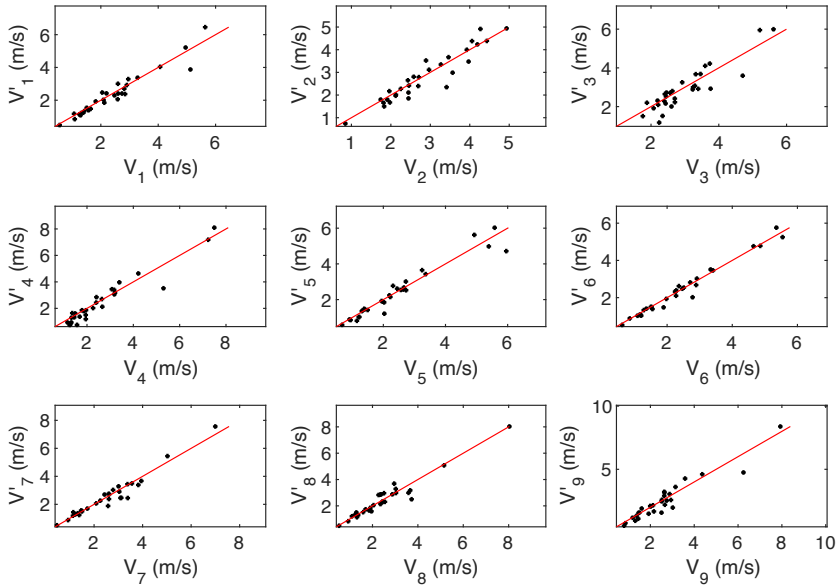

Figure 4.17 Actual-by-prediction plots of deck 4 primary location sampled points 1~9

Table 4.3 R^2 of SRS peak velocity and shock factor

Location	R^2
Deck 4 primary	89.94%
Deck 4 secondary	77.01%
Deck 3 primary	81.45%
Deck 3 secondary	80.13%
Deck 2 primary	75.21%
Deck 2 secondary	75.40%

4.3.2.2 Acceleration shock factor

In the acceleration time history, there is no clear single peak value as in the velocity time history due to the high-frequency nature of the acceleration response (see Figure 4.18 for a velocity and acceleration time history example). To mitigate the uncertainty, the average of the one third highest peak accelerations is used to quantify the acceleration magnitude instead of the absolute peak value. We call this the significant acceleration. The significant acceleration also makes more sense in assessing the destructive effect of the shock wave since the absolute peak acceleration is just a transient event. Based on the regression results in Table 4.4, the significant accelerations at all characteristic locations exhibits a strong linear relationship with the shock factor ($R > 80\%$). With the acceleration SRS, the absolute peak is sampled instead of the significant value since the SRS peak is more distinguishable (see Figure 4.19 for an SRS example). The overall R^2 (see Table 4.5) shares similar values with the peak SRS velocity regression results presented in Table 4.3.

In general, both the peak structural velocity and acceleration are considered to have a reasonably strong linear relationship with their corresponding shock factor ($R^2 > 70\%$), given the assumptions made in the shock factor derivation and the complex structural response behavior. Therefore, using the fitted shock factor prediction model (Eq. 4.8 and Eq. 4.13) to approximate the peak structural response is a reasonable approach for early stage design.

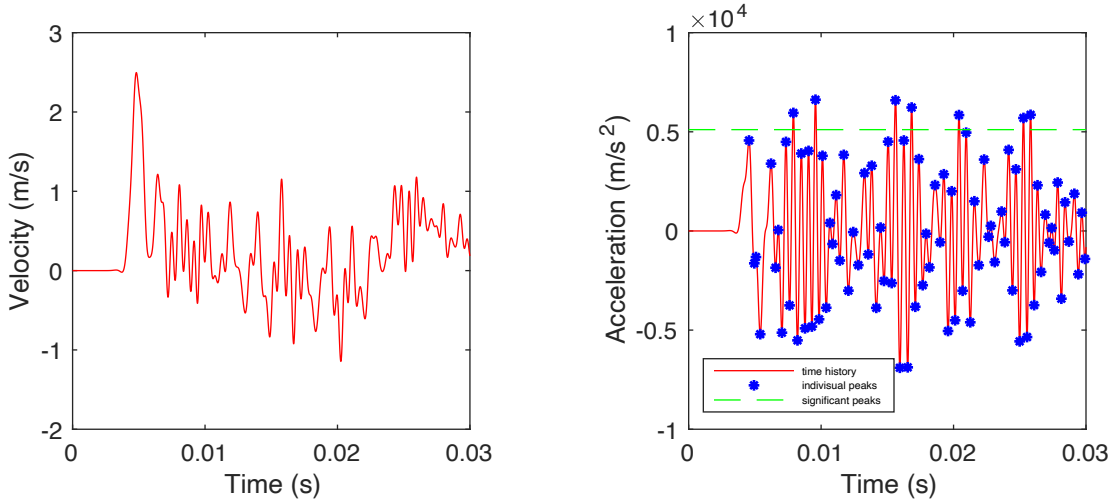

(a) Velocity time history (b) Acceleration time history

Figure 4.18 Comparison between the velocity and acceleration time history at an example structural point

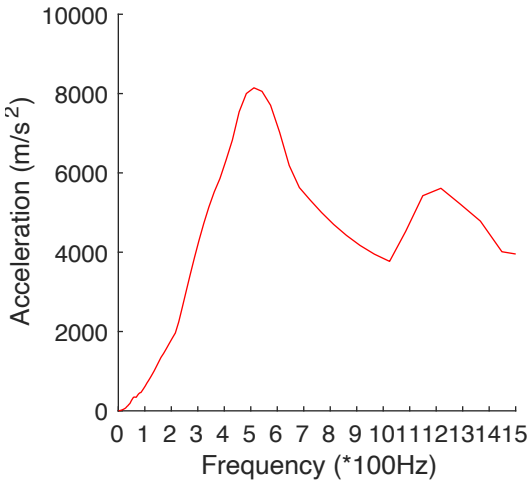

Figure 4.19 Acceleration SRS at an example structural point

Table 4.4 R^2 of the time-history peak acceleration and shock factor

Location	R^2
Deck 4 primary	81.11%
Deck 4 secondary	85.69%
Deck 3 primary	82.82%
Deck 3 secondary	86.21%
Deck 2 primary	81.29%
Deck 2 secondary	81.03%

Table 4.5 R^2 of SRS peak acceleration and shock factor

Location	R^2
Deck 4 primary	89.15%
Deck 4 secondary	74.11%
Deck 3 primary	79.56%
Deck 3 secondary	79.54%
Deck 2 primary	74.31%
Deck 2 secondary	73.30%

4.4 Taylor Plate Model

In Section 4.3, the peak structural response data for regression is generated by using the CASE model as the fluid solver. In this section, we evaluate the feasibility of substituting the Taylor Plate model for the CASE model. The structural response and the shock factor regression results when the fluid is modeled by the Taylor Plate model are presented and compared to the results for the CASE model. If the Taylor Plate result does not differ significantly from the CASE result, the computational time to collect the data for regression can be significantly shortened by using the Taylor Plate model.

4.4.1 Description of the Taylor Plate Model

The Taylor Plate model [12] does not explicitly model the whole fluid domain as in the CASE model. Instead, it assumes that the fluid is a perfect acoustic medium that allows the fluid particle displacement to be determined from the pressure of the shock wave when it reaches the structural wetted surface. In this model, an infinite air-backed rigid plate is excited by a plane shock wave (see Figure 4.20), resulting in an upward motion with velocity V_s. The incident wave with pressure p_i is then reflected from the plate with pressure p_r. The continuity relation of the fluid particle on the plate wetted surface requires that:

$$V_i cos\alpha = V_r cos\alpha + V_s \tag{4.19}$$

where the V_i and V_r are the fluid particle velocity caused by the incident and reflected wave, respectively; α is the incident angle of the wave. The particle velocity can be related to the fluid pressure by the planar wave acoustic equation of state $p = \rho cv$. Thus, Eq. 4.19 becomes:

$$\frac{p_i cos\alpha}{\rho c} = \frac{p_r cos\alpha}{\rho c} + V_s \tag{4.20}$$

which can be rearranged as:

$$p_r = p_i - \frac{\rho c V_s}{cos\alpha} \tag{4.21}$$

The total pressure at the plate wetted surface is thus related to the plate velocity as:

$$p_t = p_i + p_r = 2p_i - \frac{\rho c V_s}{cos\alpha} \tag{4.22}$$

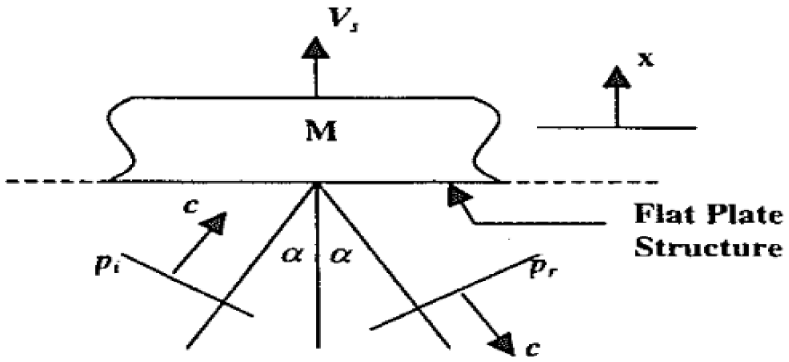

Figure 4.20 Taylor Plate case configuration

Eq. 4.22 solves for the fluid-structure interaction between the shock wave and the plate. In the original Taylor Plate model, cavitation is not considered. The total pressure on the plate can become infinitely low, which is not physical. Here, we add a cut-off condition to stop the total pressure on the wetted surface from dropping below vapor pressure when the water is cavitated:

$$p_t = \begin{cases} 2p_i - \dfrac{\rho c V_s}{cos\alpha}, & p_t > p_{cav} \\ p_{cav}, & p_t \le p_{cav} \end{cases} \tag{4.23}$$

where p_{cav} is the vapor pressure which is small enough to be considered zero.

The Taylor Plate model can be applied locally on the surface ship hull surface as a fluid pressure generator for the FEM structural solvers. Since the cavitation effect is only considered using a cut-off condition and no actual fluid is modeled, the later cavitation growth and closure,

which significantly affect the structural response, are not captured. Therefore, the result is only valid for the first few milliseconds during the shock wave impact. However, in terms of capturing the peak structural response, this may be sufficient.

4.4.2 Taylor Plate structural response results

In this section, the velocity time history of the structure response generated using the Taylor Plate fluid model is compared to that using the CASE fluid model which is considered as the benchmark. The structural response to charge 1 is used as an example. The closest structural sample points to the charge at primary and secondary locations are chosen for demonstration in Figure 4.21 since the response is typically the strongest. For the deck 4 (inner bottom) primary location (see Figure 4.21 (a)), the peak velocity happens instantly as the wave arrives since the structural point is connected directly to the hull surface by a primary structural member. The Taylor Plate model produces almost the same peak velocity and a similar velocity trend to the CASE model in the first few milliseconds after the wave arrives. After the shock wave is passed, and the local cavitation effect starts to kick in, the velocity history by the Taylor Plate model begins to deviate from the CASE model result. This is because the Taylor Plate model is only able to predict the cavitation inception time by the cut-off condition (Eq. 4.22), but unable to model the growth, shrinking, and eventual collapse of the cavitation as the CASE model does. In the Taylor Plate model, the local cavitation persists after it is generated, which causes the Taylor Plate solution to deteriorate. For the response at the other characteristic locations (see Figure 4.21 (b)~(f)), the peak velocity may not happen within the first few milliseconds after the wave arrives due to longer and more complex stress wave path. Therefore, the Taylor Plate result may not be able to capture the peak velocity correctly since it may not occur before the response starts to degrade (e.g., Figure 4.21 (b)).

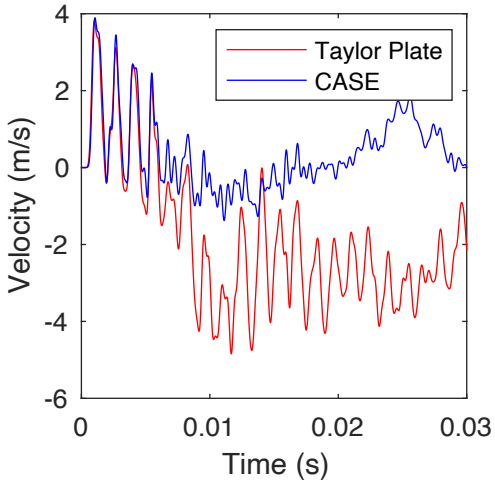

(a) Deck 4 primary location

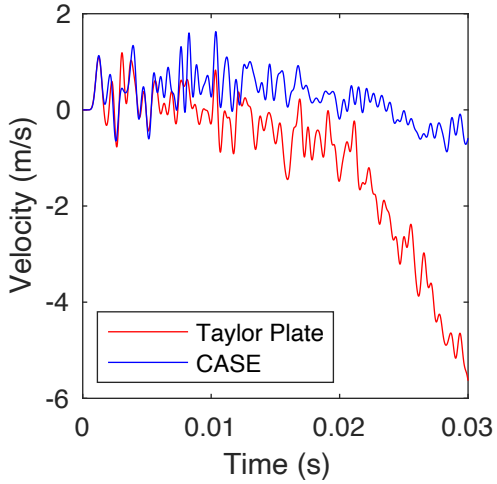

(b) Deck 4 secondary location

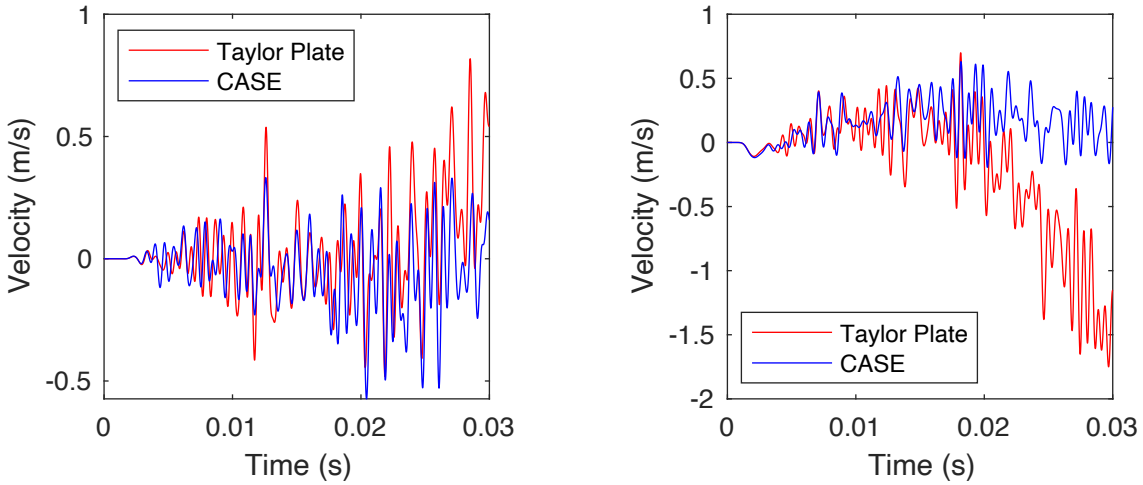

(c) Deck 3 primary location

(d) Deck 3 secondary location

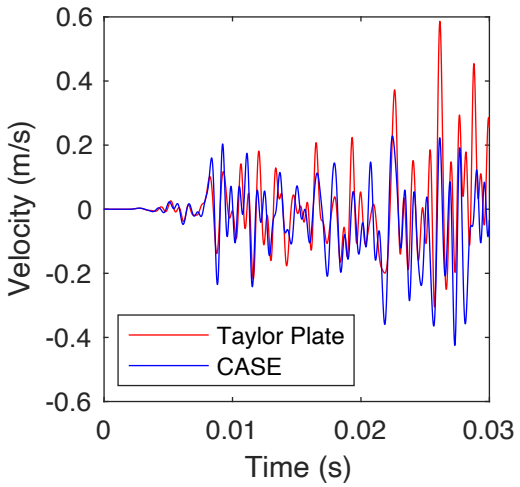

(e) Deck 2 primary location

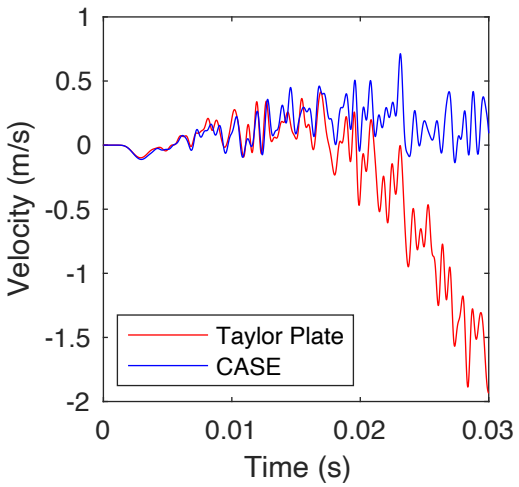

(f) Deck 2 secondary location

Figure 4.21 Comparison between Taylor Plate and CASE time-history velocity response

4.4.3 Taylor Plate shock factor prediction model regression result

In this section, the shock factor prediction models (Eq. 4.8 and Eq. 4.13) are fitted to the peak structural velocity and acceleration generated using the Taylor Plate model and their corresponding shock factor. The charge configuration and the sampled structural points used in this section are the same as in Section 4.3.2. Since the Taylor Plate results are only valid for a limited amount of time, the time history used to sample the peak response is shortened. Specifically, the deck 4 (inner bottom) primary location uses a 5ms time history after the wave arrives, and the secondary locations use a 10ms time history. For the locations on deck 3 and deck 2, a 15ms history is used. Because the peak response captured by the Taylor Plate model is not necessarily correct, the CASE result is used as the actual data y to calculate the R^2 (Eq. 4.18). The averaged R^2 value of the peak velocity and acceleration at different characteristic locations are presented in Table 4.6~Table 4.9 along with the CASE regression result (Table 4.2~Table 4.5) for comparison.

For the time-history peak velocity (Table 4.6), the Taylor Plate result at the deck 4 primary location has comparable R^2 to the CASE result. However, for the rest of the locations, the R^2 of the Taylor Plate result is significantly smaller. The less satisfactory performance of the shock factor prediction model fitted by Taylor Plate data may be explained by the observation made in Section 4.4.2. For the deck 4 primary location, the peak response happens as soon as the wave arrives, thus it is not as affected by the cavitation which the Taylor plate model cannot accurately model. For the other characteristic locations, especially those on the upper decks, the peak response occurs much later when the Taylor plate result becomes inaccurate. As for the time-history peak acceleration (Table 4.7), the degradation of R^2 is not as remarkable as in the peak velocity case because the peak acceleration response takes place earlier than the peak velocity response, thus it is more possible to happen before the Taylor Plate solution degrades.

As for the peak response in the velocity (Table 4.8) and acceleration SRS (Table 4.9), the R^2 of the Taylor Plate model result is significantly lower than the CASE result except for the deck 4 primary location. The poor performance of the Taylor Plate data fitted shock factor prediction model is because the SRS is generated by only partial time history in which the peak response is not guaranteed to be included instead of the entire time history used in CASE regression results. Overall, the Taylor Plate model is not recommended to collect the SRS peak response data for regression. Given the more acceptable correlation between the response predicted by the Taylor Plate fitted shock factor prediction model and the actual response, the Taylor Plate model may be used to obtain the time history peak response for regression in place of the CASE model with a little sacrifice of accuracy.

Table 4.6 R^2 of the time-history peak velocity and shock factor

Location	Taylor Plate	CASE
Deck 4 primary	93.33%	93.56%
Deck 4 secondary	74.95%	81.89%
Deck 3 primary	67.87%	83.83%
Deck 3 secondary	58.94%	81.02%
Deck 2 primary	67.94%	80.59%
Deck 2 secondary	54.30%	77.46%

Table 4.7 R^2 of the time-history peak acceleration and shock factor

Location	Taylor Plate	CASE
Deck 4 primary	79.71%	81.11%
Deck 4 secondary	76.22%	85.69%
Deck 3 primary	66.45%	82.82%
Deck 3 secondary	71.20%	86.21%
Deck 2 primary	67.60%	81.29%
Deck 2 secondary	75.74%	81.03%

Table 4.8 R^2 of the SRS peak velocity and shock factor

Location	Taylor Plate	CASE
Deck 4 primary	71.06%	75.67%
Deck 4 secondary	48.10%	77.01%
Deck 3 primary	50.46%	81.45%
Deck 3 secondary	52.85%	80.13%
Deck 2 primary	46.91%	75.21%
Deck 2 secondary	54.88%	75.40%

Table 4.9 R^2 of the SRS peak acceleration and shock factor

Location	Taylor Plate	CASE
Deck 4 primary	74.87%	89.15%
Deck 4 secondary	28.41%	74.11%
Deck 3 primary	41.38%	79.56%
Deck 3 secondary	45.89%	79.54%
Deck 2 primary	37.49%	74.31%
Deck 2 secondary	44.88%	73.30%

4.5 Application of the shock factor

In this section, we present a simplified notional application of shock factor in the ship design problem. In order to arrange onboard equipment with different shock-resistance capability, the strength of the structural shock response throughout the ship should be known. Based on the discussion so far, the fitted shock factor prediction model (Eq. 4.8 and Eq. 4.13) for a specified structural point could be used to predict the structural response to specified UNDEX scenarios. Ships are typically divided into subdivision blocks (SDBs) bounded by two adjacent bulkheads, decks and side-hull surfaces (see the red box in Figure 4.22 for an example SDB). In early-stage ship design, components (e.g., equipment) may be assigned to SDBs instead of particular structural locations. To make preliminary system arrangement decisions, it is sufficient to know the relative structural response of the SDBs. If the structural response of representative points (e.g., bottom center) (primary or secondary) in each SDB may be used to represent shock response intensity for the entire SDB, then the shock factor prediction model may be used to calculate this intensity. To assess this idea, the significant acceleration of the bottom center (or the closest point to the bottom center) primary and secondary location points in each SDB are sampled and compared to the mean significant acceleration of all primary and secondary bottom location points in each subdivision block. The correlation between the center response a_c and the mean response $\bar{a}$ is evaluated by a ratio $\lambda = a_c/\bar{a}$. If the λ is close to 1, the structural response at the bottom center may be considered to represent the entire subdivision block deck. The structural responses for three different charges are collected. The first charge is right below the midship keel, the second charge is also below the keel but close to the ship stern, and the third charge is close to the midship but with a large transverse standoff. The λ of all subdivision blocks from deck 4 (inner bottom) to deck 04 (deckhouse) are calculated (see Figure 4.22 for deck and section numbering convention).

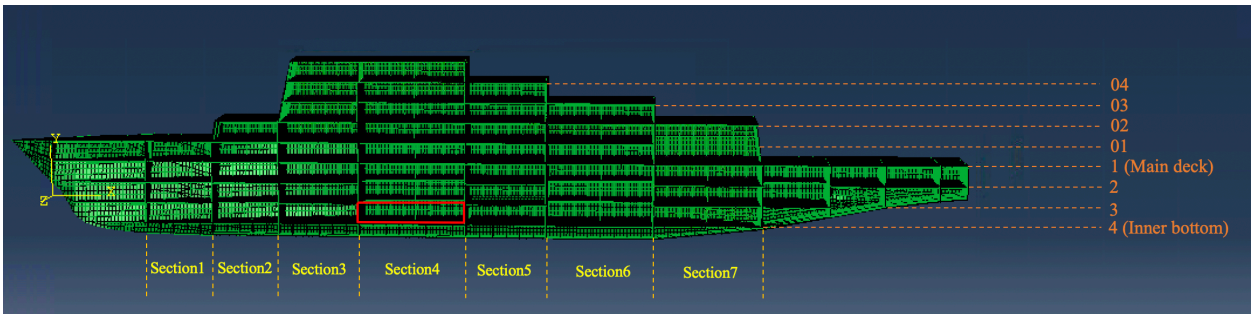

Figure 4.22 Deck and block naming convention

In Table 4.10, the standard deviation (SD) of the significant acceleration response to charge 1 at primary bottom points of each SDB is listed along with the SD of the SDB mean significant acceleration on each deck (last column). The SD value indicates that the variation of the significant acceleration between SDBs is larger than the variation in individual SDBs on each deck except for block 5 on deck 4, which supports the plan of assigning components to SDB instead of specific structural points.

Table 4.10 Standard deviation of the significant acceleration

Deck	Section 1	Section 2	Section 3	Section 4	Section 5	Section 6	Section 7	Deck SD
04			94.28	253.95	196.84			369.01
03			36.12	198.56	150.69	115.55		287.45
02		25.77	59.51	206.38	208.77	94.55	33.51	329.92
01	12.10	28.50	67.34	231.22	193.10	101.24		409.17
1	32.78	25.70	55.87	327.43	391.35	174.93	35.22	616.54
2	10.48	34.78	106.95	409.43	417.39	228.81	44.49	774.31
3	29.75	80.09	167.17	658.66	421.48	364.60	88.35	975.36
4	198.41	316.89	540.73	2216.37	6311.91	1720.04	849.36	3448.64

Contours of the structural response to charge 1 for primary location points in deck 4 SDBs are plotted in Figure 4.23. Center points are indicated with a green dot and average responses are represented by a plane surface. The corresponding λ of the SDBs on all decks is listed in Table 4.11. The largest λ is for deck 4 block 5, which is caused by the high acceleration gradient due to the close proximity to the charge center. Further away from the charge center, the acceleration distribution becomes more even and λ becomes closer to 1. For the response at the secondary location to charge 1 and the response to charge 2 and charge 3, the λ distribution follows a similar trend. The average and standard deviation of λ of all the subdivision blocks are calculated and listed in Table 4.12. For all the charge cases assessed, the structural response at the block bottom center correlates fairly well with the mean response even when the shock wave is highly oblique to the ship (charge 3). Therefore, the shock factor prediction function at the primary and secondary location bottom center of each SDB may be sufficient to approximate the response of the entire ship.

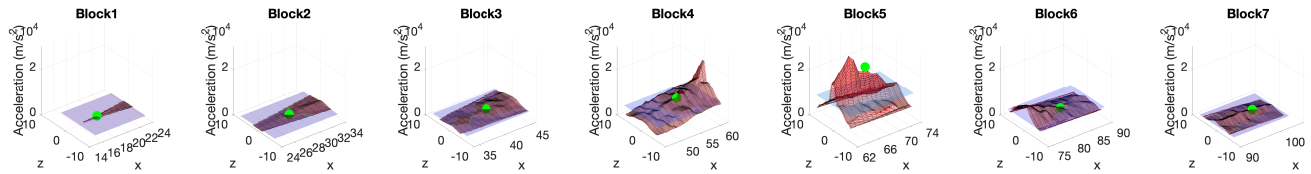

Figure 4.23 Deck 4 primary location response to charge 1 contour plot

Table 4.11 λ of each SDB primary location (charge 1)

Deck	Section 1	Section 2	Section 3	Section 4	Section 5	Section 6	Section 7
04			0.45	1.13	1.22		
03			1.09	1.04	0.91	0.99	
02		0.61	0.95	0.94	1.00	0.89	1.38
01	0.97	0.97	1.13	1.03	0.92	1.02	
1	0.68	1.30	1.33	1.15	1.02	0.87	0.97
2	1.14	1.21	1.33	1.17	1.06	0.71	0.81
3	1.01	1.33	0.98	1.15	1.19	0.78	0.85
4	1.43	1.19	1.24	1.36	2.13	0.88	1.58

Table 4.12 Average and standard deviation of λ

	Primary Location	Secondary Location
Charge 1	1.07 (0.27)	0.98 (0.34)
Charge 2	0.99 (0.23)	0.88 (0.31)
Charge 3	0.78 (0.21)	0.73 (0.19)

4.6 Conclusion

In this work, the shock factor concept proposed by Keil [1] is refined and extended to predict peak acceleration and evaluated in a surface ship UNDEX problem. The linear relationship between the structural peak response and the shock factor is assessed by regression analysis. The structural response data used for regression is generated by a CASE-Abaqus coupled FSI solver. For peak time-history velocity response, the strongest linear relationship is found on deck 4 (inner bottom) primary location. At the other types of characteristic locations not directly connected to the ship hull, the linear relationship becomes weaker since the shock factor cannot estimate the shock wave energy as well as at the deck 4 primary location. Similar linear relationship is found between the significant peak acceleration and the shock factor at all assessed characteristic locations. Both peak velocity and acceleration response in the shock response spectrum (SRS) shows a weaker linear relationship with their corresponding shock factor than the time-history peak response because the local cavitation influences the time history input used to generate SRS. Overall, reasonably strong linear relationships are found between the structural responses in both time-history and SRS and their corresponding shock factors. Therefore, the fitted shock factor prediction models (Eq. 4.8 and Eq. 4.13) can be used to approximate the peak structural response in place of the numerical solver, which significantly saves computational effort. The feasibility of substituting the Taylor Plate model for the CASE model is also evaluated. Based on the correlation between the fitted shock factor prediction function and the actual response, the Taylor plate model is only recommended to obtain the time-history peak structural response. The structural response at the subdivision block bottom center is shown to represent the response of the entire block fairly well. As a result, the shock factor prediction model obtained at the bottom center of each subdivision block can be used to approximate the structural response across the ship and potentially as a metric for locating equipment in early stage ship design.

Although the surrogate approach proposed in this work is not as definitive as the numerical approach, it provides valuable insight on how UNDEX shock structural response varies within the ship and an alternative to improve the simulation efficiency. In terms of the future investigation on this topic, a larger matrix of SF hull reference points should be assessed to better calculate response throughout the ship. Experiments should also be performed to determine if the shock factor prediction models obtained for a specified ship can be applied to ships with similar topologies. Furthermore, a coefficient C as a function of ship dimensions may be added to the shock factor prediction models (Eq. 4.8 and Eq. 4.13) to accommodate ships with different topologies:

$$v_i^{peak} = C(L, B, D) \cdot l_i \cdot SF_i \tag{4.24}$$

$$a_i^{peak} = C(L, B, D) \cdot q_i \cdot SFA_i \tag{4.25}$$

where L, B and D represent ship length, width and depth.

Reference

[1] A. H. Keil, "The Response of Ships To Underwater Explosions," in *Transactions of Society of Naval Architects and Marine Engineers*, 1961.

[2] E.W.Clements, "Shipboard Shock and Navy Devices for Its Simulation," *NRL Rep.*, 1972.

[3] N. Bradbeer and D. Andrews, "Shock Response Implication of Lower-cost Warship Structural Styles," in *Proceedings of IMDC 2012*, 2012.

[4] Y. S. Shin, "Ship Shock Modeling and Simulation for Far-Field Underwater Explosion," *Comput. Struct.*, vol. 82, no. 23–26, pp. 2211–2219, 2004.

[5] M. A. Sprague and T. L. Geers, "A Spectral-Element/Finite-Element Analysis of a Ship-Like Structure Subjected to an Underwater Explosion," *Comput. Methods Appl. Mech. Eng.*, vol. 195, no. 17–18, pp. 2149–2167, 2006.

[6] Z. Lu and A. J. Brown, "Assessment of a New Mesh Generation and Modeling Approach for the Surface Ship Far-field Underwater Explosion Problem," in *SNAME Maritime Convention (SMC) 2019*, 2019.

[7] G. J. O'Hara and P. F. Cunniff, "Scaling for Shock Response of Equipment in Different Submarines," *Shock Vib.*, vol. 1, no. 2, pp. 161–170, 1993.

[8] W. Zhang and W. Jiang, "An Improved Shock Factor to Evaluate the Shock Environment of Small-Sized Structures Subjected to Underwater Explosion," *Shock Vib.*, vol. 2015, pp. 1–11, 2015.

[9] J. Guo, X. bin Ji, Y. yan Wen, and X. wei Cui, "A new shock factor of SWATH catamaran subjected to underwater explosion," *Ocean Eng.*, vol. 130, no. December 2016, pp. 620–628, 2017.

[10] C.-C. Liang and Y.-S. Tai, "Shock responses of a surface ship subjected to noncontact underwater explosions," *Ocean Eng.*, vol. 33, no. 5–6, pp. 748–772, 2006.

[11] Z. Lu and A. J. Brown, "Application of the Spectral Element Method in a Surface Ship Far-Field UNDEX Problem," *Shock Vib.*, vol. 2019, 2019.

[12] G. I. Taylor, "The Pressure and Impulse of Submarine Explosion Waves on Plates," *Sci. Pap. Sir Geoffrey Ingram Taylor*, pp. 287–303, 1941.

[13] N. A. Fleck and V. S. Deshpande, "The Resistance of Clamped Sandwich Beams to Shock Loading ," *J. Appl. Mech.*, vol. 71, no. 3, pp. 386–401, Jun. 2004.

[14] G. J. McShane, V. S. Deshpande, and N. A. Fleck, "Underwater blast response of free-

standing sandwich plates with metallic lattice cores," *Int. J. Impact Eng.*, vol. 37, no. 11, pp. 1138–1149, 2010.
[15] Z. Liu and Y. L. Young, "Transient Response of Submerged Plates Subject to Underwater Shock Loading: An Analytical Perspective," *J. Appl. Mech.*, vol. 75, no. July 2008, pp. 1–5, 2008.
[16] K. A. Sebert, "A Mathematical Model of Transient Motion Response of the US Navy Floating Platform," The University of Akron, 1984.
[17] A. K. Mathew, "Modeling Underwater Explosion (UNDEX) Shock Effects for Vulnerability Assessment in Early Stage Ship Design," Virginia Tech, 2018.
[18] R. H. Cole, *Underwater Explosions*. Princeton University Press, 1948.
[19] A. B. Hwee and H. M. Jeremy, "Managing Shock Requirements of Shipboard Equipment," *DSTA Horizons*, pp. 30–37, 2013.
[20] J. E. Alexander, "Shock Response Spectrum – A Primer," *Sound Vib.*, no. June, pp. 6–14, 2009.

Appendix. A: Surface ship charge configuration and structural sampled point location

Table 4.13 Charge location and weight

Case	x_c (m)	y_c (m)	z_c (m)	w (lb)
1	46.29	-38.29	16.14	130.14
2	57.35	-35.03	-3.41	92.53
3	71.52	-28.09	18.04	110.81
4	62.78	-46.05	-8.79	98.84
5	51.53	-21.80	7.08	128.46
6	39.43	-44.43	8.07	71.70
7	73.55	-28.58	-4.01	125.89
8	51.20	-39.76	3.01	74.84
9	41.92	-47.64	2.33	63.68
10	84.16	-29.71	-14.82	59.36
11	69.03	-41.24	-10.68	105.97
12	88.59	-32.44	-1.69	88.40
13	61.12	-26.49	-19.44	56.58
14	99.04	-37.37	19.20	106.87
15	86.59	-49.71	-16.96	83.74
16	77.72	-23.92	-12.23	149.21
17	76.46	-35.90	12.76	138.87
18	79.86	-41.68	10.92	68.93
19	43.72	-25.29	-0.66	121.85
20	65.31	-31.80	-9.50	117.00
21	91.93	-20.92	-5.96	52.04
22	37.87	-47.22	14.30	134.75
23	54.66	-23.41	-16.78	143.41
24	96.64	-33.74	9.25	78.28
25	92.85	-43.94	4.65	97.36
26	64.86	-7.56	15.26	114.23
27	96.31	-5.63	-16.12	99.19
28	48.64	-18.35	-17.61	149.30
29	72.92	-10.70	18.60	81.20
30	81.11	-12.58	19.26	122.70

Table 4.14 Inner bottom primary location sampled points

Point	x (m)	y (m)	z (m)
1	52	-4	0
2	64	-4	0
3	76	-4	0
4	52	-4	-7.1
5	52	-4	-5.08
6	52	-4	-2
7	52	-4	2
8	52	-4	5.08
9	52	-4	7.1
10	64	-4	-5.08
11	64	-4	-2
12	64	-4	2
13	64	-4	5.08
14	76	-4	-5.08
15	76	-4	-2
16	76	-4	2
17	76	-4	5.08
18	38	-4	0
19	38	-4	2
20	38	-4	-2
21	38	-4	5.08
22	38	-4	-5.08
23	88	-4	0
24	88	-4	2
25	88	-4	-2
26	88	-4	5.08
27	88	-4	-5.08

Table 4.15 Inner bottom secondary location sampled points

Point	x (m)	y (m)	z (m)
1	39	-4	3.60
2	39	-4	0.80
3	39	-4	-0.80
4	39	-4	-3.60
5	53	-4	5.88
6	53	-4	3.48
7	53	-4	0.80
8	53	-4	-0.80
9	53	-4	-3.48
10	53	-4	-5.88
11	65	-4	6.68
12	65	-4	3.60
13	65	-4	1.20
14	65	-4	-1.20
15	65	-4	-3.60
16	65	-4	-6.68
17	77	-4	6.68
18	77	-4	3.60
19	77	-4	0.80
20	77	-4	-0.80
21	77	-4	-3.60
22	77	-4	-6.68
23	89	-4	3.60
24	89	-4	0.80
25	89	-4	-0.80
26	89	-4	-3.60
27	89	-4	6.68
28	89	-4	-6.68

Table 4.16 First upper deck primary location sampled points

Point	x (m)	y (m)	z (m)
1	64	-0.92	0
2	52	-0.92	-5.08
3	52	-0.92	5.08
4	64	-0.92	-5.08
5	64	-0.92	-2
6	64	-0.92	2
7	64	-0.92	5.08
8	76	-0.92	-5.08
9	76	-0.92	5.08
10	38	-0.92	0
11	38	-0.92	2
12	38	-0.92	-2
13	38	-0.92	5.08
14	38	-0.92	-5.08
15	88	-0.92	5.08
16	88	-0.92	-5.08

Table 4.17 First upper deck secondary location sampled points

Point	x (m)	y (m)	z (m)
1	65	-0.92	0.8
2	53	-0.92	-5.88
3	53	-0.92	5.88
4	65	-0.92	-4.05
5	65	-0.92	-3.03
6	65	-0.92	3.03
7	65	-0.92	4.05
8	77	-0.92	-5.88
9	77	-0.92	5.88
10	39	-0.92	0.8
11	39	-0.92	3.03
12	39	-0.92	-3.03
13	39	-0.92	5.88
14	39	-0.92	-5.88
15	89	-0.92	5.88
16	89	-0.92	-5.88

Table 4.18 Second upper deck primary location sampled points

Point	x (m)	y (m)	z (m)
1	64	2.16	0
2	52	2.16	-5.08
3	52	2.16	5.08
4	64	2.16	-5.08
5	64	2.16	-2
6	64	2.16	2
7	64	2.16	5.08
8	76	2.16	-5.08
9	76	2.16	5.08
10	38	2.16	0
11	38	2.16	2
12	38	2.16	-2
13	38	2.16	5.08
14	38	2.16	-5.08
15	88	2.16	5.08
16	88	2.16	-5.08

Table 4.19 Second upper deck secondary location sampled points

Point	x (m)	y (m)	z (m)
1	65	2.16	0.8
2	53	2.16	-5.88
3	53	2.16	5.88
4	65	2.16	-4.05
5	65	2.16	-3.03
6	65	2.16	3.03
7	65	2.16	4.05
8	77	2.16	-5.88
9	77	2.16	5.88
10	39	2.16	0.8
11	39	2.16	3.03
12	39	2.16	-3.03
13	39	2.16	5.88
14	39	2.16	-5.88
15	89	2.16	5.88
16	89	2.16	-5.88

Chapter 5 Conclusion and Future Work

In this dissertation, efforts are made to make the far-field UNDEX simulation more efficient and at the same time sufficient for early-stage ship design. A partitioned fluid-strucutre interaction framework coupling CAFE/CASE fluid solver and Abaqus structural solver is built. It is found that superior computational efficiency is achieved with high-order spectral elements in a Floating Shock Platform far-field UNDEX problem. The high-order CASE possesses the highest computational efficiency compared to the linear CAFE and CASE, which is furnished by better acoustic wave propagation and cavitation modeling. As the element order increases, the advantage of high-order CASE becomes larger. The numerical experiment of mapping schemes suggests that the consistent mapping approach is the most suitable one for UNDEX problems as it well guarantees the force and energy conservation with straightforward implementation.

To accelerate the meshing process and apply the spectral element in surface ship problems, an automatic all-hexahedral meshing solution called Sculpt algorithm is assessed and compared to the popular all-tetrahedral mesh. The all-hex mesh generated by the Sculpt algorithm using high-order CASE element shows the highest computational efficiency if the Total Field Model (TFM) is used. If the Scattered Field Model (SFM) is used, the all-hex mesh using linear CASE element is the most efficient. The shadow effect of the SFM is also demonstrated and a modified SFM method is tested and proven effective. Due to the more computationally efficient nature of the SFM, the best strategy to model the fluid domain for the surface ship problem indicated in this dissertation is to use a combination of the modified SFM and all-hex mesh generated by the Sculpt algorithm using linear CASE element.

In the last part of this dissertation, a surrogate statistical model developed from the shock factor proposed by Keil is assessed. Reasonably strong linear relationship is found between the peak structural response and shock factor after regression analysis. The shock factor prediction model generated using the data collected by CASE-Abaqus FSI solver can be used to obtain the peak structural response with little computational cost in the concept exploration. The investigation of non-numerical fluid model suggests that it is feasible to replace the CASE model with the analytical Taylor Plate model for collecting the time-history peak structural response data. The shock factor prediction model obtained at each subdivision block (SDB) bottom center can be used to estimate the structural response across the ship since it is shown that the structural response at the bottom center can well represent the response of the entire SDB. Although the surrogate methodology proposed in this dissertation is not very definitive, it may provide valuable insights on improving the simulation efficiency in design problems.

To facilitate the future applications of the shock factor in early-stage ship design, the following potential research directions are recommended:

- Several metrics to assess the structural peak response in both time and frequency domains are presented in this dissertation. However, the most effective metric for different design objectives must be determined.
- To further improve the current shock factor model, a larger matrix of hull reference points should be explored.
- To integrate the current shock factor knowledge into an optimization framework in early-stage design, a general response surface model (RSM) for peak structural response with the shock factor and parametrized SDB location as explanatory variables is required.

- Numerous different hull forms need to be evaluated in the concept exploration. It is difficult to generate an RSM for each design. Experiments should be performed to verify the extent to which the RSM generated for one ship may be applied to ships with similar topologies and how this may best be implemented. A more general RSM with ship dimensions as additional explanatory variables can be built to consider ships with different topologies.